Two-dimensional transition metal dichalcogenide : point defects and junctions studied from DFT and STM

van Dung Nguyen

Communauté
UNIVERSITÉ Grenoble Alpes

THÈSE

Pour obtenir le grade de

DOCTEUR DE LA COMMUNAUTE UNIVERSITE GRENOBLE ALPES

Spécialité : **Nanophysique**

Arrêté ministériel : 25 mai 2016

Présentée par

Van Dung NGUYEN

Thèse dirigée par **Laurence Magaud, Directrice de Recherche, Institut Néel**
codirigée par **Johann Coraux, Chargé de Recherche, Institut Néel**

préparée au sein de **l'Institut Néel**
dans **l'École Doctorale de Physique de Grenoble**

Dichalcogenures de métaux de transition: Défauts Ponctuels et Jonctions étudiés par DFT et STM

Thèse soutenue publiquement le **20 Novembre 2019**,
devant le jury composé de :

Dr. Florent CALVO
Directeur de recherche au Liphy, Président
Dr. Yannick DAPPE
Chargé de Recherche au Service de Physique de l'État Condensé, CEA Saclay, Rapporteur
Dr. Martine MAYNE
Directeur de recherche au NIMBE, CEA Saclay, Rapporteur
Dr. Xavier WALLART
Directeur de recherche à IEMN, Examinateur

Contents

Introduction **1**

1 Simulation and Experimental Methods **3**

1.1 Density Functional Theory - a brief summary 3

1.2 Ultra High Vacuum (UHV) system 6

1.2.1 Multi-purpose UHV system 6

1.2.2 Reflection High Energy Electron Diffraction (RHEED) 7

1.2.3 Scanning Tunneling Microscope (STM) 8

1.3 Conclusion 11

2 Transition Metal Dichalcogenides (TMDC) **13**

2.1 Two Dimensional Materials: Physics of Materials with Reduced Dimensionality 14

2.1.1 Graphene 14

2.1.2 TMDC: from Bulk to Monolayer 15

2.1.3 Electronic Properties 23

2.2 Preparation of TMD Monolayers 29

2.2.1 Top-down technique 30

2.2.2 Bottom-up technique 31

2.3 Conclusion 34

3 Point Defects in Single Layer TMDs **35**

3.1 Introduction 35

3.1.1 Intrinsic point defects in single layer TMDCs 36

3.2 DFT calculations of point defects in MoS_2 38

3.2.1 Calculation details 38

3.2.2 S vacancy . . . 38
3.2.3 S divacancy . . . 39
3.2.4 Se/S substitution . . . 42
3.2.5 B/S substitution . . . 43
3.2.6 C/S substitution . . . 44
3.2.7 N/S substitution . . . 45
3.2.8 Cl/S substitution . . . 46
3.2.9 Mo vacancy . . . 46
3.2.10 Fe/Mo substitution . . . 47
3.3 Weakly Trapped, Charged, and Free excitons in Single-Layer MoS_2 in the Presence of Defects, Strain, and Charged Impurities . . . 48

4 $MoSe_2$/WSe_2 in-plane junction - the zigzag case 51
4.1 Introduction . . . 51
4.1.1 Methods . . . 52
4.1.2 From infinite 2D materials to WSe_2 zigzag ribbon . . . 52
4.2 $MoSe_2$/WSe_2 heterojunction . . . 53
4.3 Se vacancy in a $MoSe_2$/WSe_2 junction (20x4) . . . 55
4.4 Conclusion . . . 58

5 Epitaxial of TMDs on Metal Surface 59
5.1 Introduction . . . 59
5.2 Reactive molecular beam epitaxy of MoS_2 on Au(111) . . . 61
5.3 Results and Discussion . . . 63
5.3.1 Structure of MoS_2 single-layer islands on Au(111) . . . 63
5.3.2 Effects of Cs intercalation on the structure of MoS_2 . . . 65

Conclusions 71

Perspectives 73

Appendix 75

Introduction

Two-dimensional (2D) transition metal dichalcogenides (TMDCs) are a large family of 2D materials covering a broad range of electronic, optical and magnetic properties. These compounds, made of a few or a single layer of the formula is MX_2 (M a transition metal, X a chalcogen atom S, Se or Te) have been known for decades in their bulk form, and it is only since 2010 that they started to attract strong interest. In particular, semiconducting 2D TMDCs have been intensively studied, probably in reason of their unique optoelectronic properties (e.g. strong absorption of light, exciton-dominated light emission at room temperature, direct or indirect bandgap, the spin-orbit-induced polarisation of the electronic bands) which strongly depend on the number of layers. The present manuscript is also focused on these semiconducting materials and addresses their growth, structural and electronic properties, in some cases in a situation that is relevant pn the long term in the prospect of optoelectronic applications where understanding the effect of defects/doping and the nature of junctions is crucial. While these questions have been thoroughly investigated in the case of 3D semiconductors, at the moment our work started this was not the case for 2D TMDCs.

The work presented here relies on both experimental and computational methods, which are presented within the first chapter. There, we explain basic concepts of density functional theory (DFT) calculations that were used to simulate the ground-state structures and their electronic properties. We also give more practical details related to the way they were performed. In this chapter, we also introduce the surface science tools that were used to study the growth and structure of the TMDCs. This comprises a description of the ultrahigh vacuum systems hosting the growth facilities and characterization techniques, a scanning tunneling microscope (STM) and a reflection high-energy electron diffraction (RHEED) apparatus.

The second chapter presents, in a partial way, the state of knowledge on some of the basic properties of 2D TMDCs put in perspective with those of graphene. A focus is given on the variation of the electronic properties as a function of the number of layers. The corresponding literature review is supplemented with new DFT calculations of the structure and electronic properties of MoS_2 in different crystallographic structures, that will serve as a reference for the rest of the manuscript. This second chapter also discusses the practical

issue of the preparation of 2D TMDCs, which helps to position the work that we present in *Chapter* 5.

In the third *Chapter*, we report our study of defects in free-standing 2D MoS_2. Using DFT simulations, we address a large number of defects, vacancies and substitutional atoms, and discuss their structure and their impact on the electronic properties of the material. This study allowed us to identify a new kind of defect found in experiments. These substitutional defects, presumably N substitutional atoms, have strong consequences on the optical properties of the material. We briefly summarize the corresponding experimental results at the end of the chapter.

In the fourth *Chapter* we turn to 2D junctions combining two different TMDCs, $MoSe_2$ and WSe_2. Such architecture is thought to yield p-n junctions. With DFT calculations, we analyze their structure, the modification of the electronic properties in the two materials due to the contact with the other, and whether interface electronic states form. This study is crucial to devise on the use of these junctions in future optoelectronic devices. We also study the influence of a defect, a chalcogen vacancy, in these junctions.

The fifth chapter is devoted to a practical realization of single-layer MoS_2 when it is prepared on an Au(111) substrate. We provide a detailed structural analysis based on STM, RHEED, and synchrotron X-ray diffraction. We first address the growth of MoS_2 using reactive molecular beam epitaxy method. In this system (MoS_2/Au(111)), MoS_2 is not free-standing but is rather strongly coupled to its substrate. Aiming at recovering quasi-free-standing properties, we then investigated the decoupling of MoS_2 from Au(111) using the process of intercalation, here with an ultra-thin layer of Cs. We find that the structure of MoS_2 is indeed substantially changed after intercalation. The process is promoted by a moderate increase in temperature and can be reversed when the temperature is further increased.

Chapter 1

Simulation and Experimental Methods

1.1 Density Functional Theory - a brief summary

The pursued goal of simulation at the atomic level is to be able to describe and even predict the structural and electronic properties while keeping the computational load acceptable. This means solving the following Schrödinger equation (in atomic units):

$$\left[\sum_{nuclei} \frac{p_n^2}{2m_n} + U_{n-n(r)} + \sum_{electrons} \frac{p_e^2}{2} + U_{e-n(r)} + \sum_{i,i,i\neq j} \frac{1}{|r_i - r_j]}\right| \Psi = E\Psi \qquad (1.1)$$

and then describe interactions within a system (electron-electron, electron-nuclei, nuclei-nuclei) with sufficiently high accuracy.

Different approaches are available based on different levels of approximation. During my Ph.D. works, I used Density Functional Theory (DFT), a so-called *ab-initio* approach because it does not require the use of parameters. The main idea of DFT is to focus on the electronic density $n(r)$ and not on the wavefunctions. However, parameter-free does not mean no approximation and the main approximations used in the DFT are described in the following.

The ion mass is much larger than the electron one so that one can consider that the electrons respond instantaneously to the motion of the ions, or said differently, for any ionic movement, the electrons can be considered as in their ground-state. Ions can then be treated as classical particles, and their motion calculated from classical equations of motion. With this adiabatic approximation, the Schrödinger equation reduces to its electronic part, describing the electron motion in an external potential created by the ions,

$$\left[\sum_{\text{electrons}} \frac{p_e^2}{2} + U_{e-n(r)} + \sum_{i,j,i\neq j} \frac{1}{|r_i - r_j|}\right] \Psi = E\Psi$$

Hohenberg and Kohn showed that the external potential is a functional of the electronic density *n(r)* so that E is a functional of *n(r)* and then that solving this equation is equivalent to minimizing the energy as a function of the electronic density *n(r)*. The ground state electronic density is the one that minimizes the energy and the ground state energy is the minimum energy.

Calculating *n(r)* is not straightforward and Kohn and Sham solved this difficulty by mapping the actual system of N particles interaction on N non-interacting systems. They used a basis of 1-electron functions to express the electronic density *n*. They obtained the Kohn-Sham equations:

$$\left|\frac{-1}{2} \bigtriangledown^2 + V_{KS}(r)\right| \varphi(r) = \varepsilon_i \varphi_i(r),$$

$$n(r) = \sum_i |\varphi_i(r)|^2 ,$$

$$V_{KS}(r) = V_{ext}(r) + V_H(r) + V_{XC}(r),$$

$$V_H = \int \frac{n(r')}{|r - r'|} dr',$$

$$V_{XC} = \frac{\delta E_{XC}}{\delta n}.$$

These are Schödinger-like equations with a Kohn-Sham potential V_{KS} that contains the electron-nuclei interaction $V_{ext}(r)$, the Hartree term $V_H(r)$ and an extra term that describes electronic interactions, the exchange, and correlation V_{XC} potential.

The main difficulty stays now in this exchange and correlation term V_{XC} that can not be obtained easily. Kohn and Sham proposed a rather raw approximation: they calculate the XC energy of the real system using the XC energy of the homogeneous gas for the electronic density n of the real system at each position r:

$$E_{XC}^{LDA}|n(r)| = \int \varepsilon_{XC}^{hom}(n = n(r))n(r)dr,$$

this Local Density Approximation (LDA) works surprisingly well in multiple systems and is

part of the success of the DFT approach.

However, LDA also has many drawbacks and especially, it tends to overestimate the binding energy. The overestimation comes from the fact that LDA is based on homogeneous system expressions while the real electronic system is non-homogeneous. Therefore, in order to describe the electron density variations, corrections have been proposed, such as generalized gradient approximation (GGA), in which the $E_{XC}(n)$ depends not only on the electron density *n(r)* at a given point (locally) but also on its gradient $\delta n(r)$ (non-local). All the calculations performed during my Ph.D. works have been obtained with the Perdew, Burke, and Ernzerhof (PBE) expression of GGA.[121]

Eventually, forces are obtained from the partial derivative of the total energy as a function of the position. From the force calculation the atomic positions in the ground-state geometry can be deduced:

$$F_i = -\frac{\delta E}{\delta R_i}.$$

Van der Waals interactions can play an important role in 2D materials. In VASP, they can be accounted for using different functionals. In most of the calculations presented in the following I used PBE only but some tests were made using PBE0 and HSE06[83] Hybrid Functionals. It is worth noticing that the one-electron function $\varphi(r)$ are mathematical tools to calculate $n(r)$, and not true wavefunction of the quasiparticles. ε_i are not the quasiparticles energies either. Anyway, they are very often used to get band structures with a quite good agreement with experiments in many systems.

VASP and technical details of the calculations

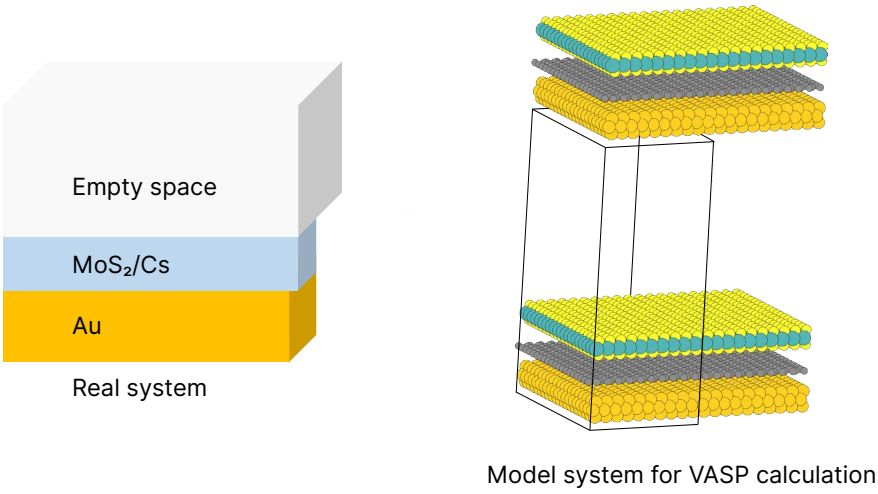

Figure 1.1: Supercell technique for an interface or a surface.

In this thesis, we used the Vienna Ab-initio Simulation Package (VASP).[149] It enables us to determine the atom positions at equilibrium, the density of state and the electronic band

structure of a given system. In some calculations, the partial charge maps integrated in an energy window $\int |\Psi|^2 \, dE$ are also plotted to compare to STM images. The VASP program uses a plane wave basis, and we used the projected-augmented-wave (PAW) formalism to describe the electron-ion interaction. VASP requires a periodic system. Deviations to 3D-periodic defect-free structures hence need to be considered with care.

In the case of a surface or an interface, the supercell must be large enough (empty space and substrate) to avoid spurious interaction between images created by periodic conditions (See Fig. 1.1). Defects are also modeled using a supercell approach where a large unit cell is created assembling $m \times n \times l$ unit cells, the defect is introduced in the center. Here again, the supercell has to be large enough to describe an isolated defect and not a periodic array of defects.

The main files used for VASP calculations are given in Appendix A.

1.2 Ultra High Vacuum (UHV) system

The UHV system installed at Institute Neel includes several chambers and instruments that allow us to perform sample preparation and *in situ* characterization. The following parts give a brief introduction to this system.

1.2.1 Multi-purpose UHV system

UHV conditions are essential for surface science since chemically clean sample surfaces without any unwanted adsorbates are required. The UHV system is shown in Fig. 1.2. It contains 4 chambers connected by a tunnel [which is also in UHV with a base pressure of 10^{-10} mbar]. Most of the time, all chambers are isolated from the tunnel by mechanical valves.

The tunnel is used to transfer the samples from one chamber to another one by magnetic transfer rods. It is also used to introduce/remove samples. To do so, a small part of the tunnel is filled with Nitrogen gas and exposed to the environment during the introduction of the samples. This part is carefully isolated from the whole system.

Samples are mounted onto molybdenum plates, that are themselves held onto 1-inch large molybdenum blocks designed to be compatible for the transfer and also the sample holder of each chamber (including the growth and the STM chambers). I mainly used the growth and STM chambers. The growth chamber is also equipped with an electron gun and a phosphor screen to perform reflection high energy electron diffraction (RHEED).

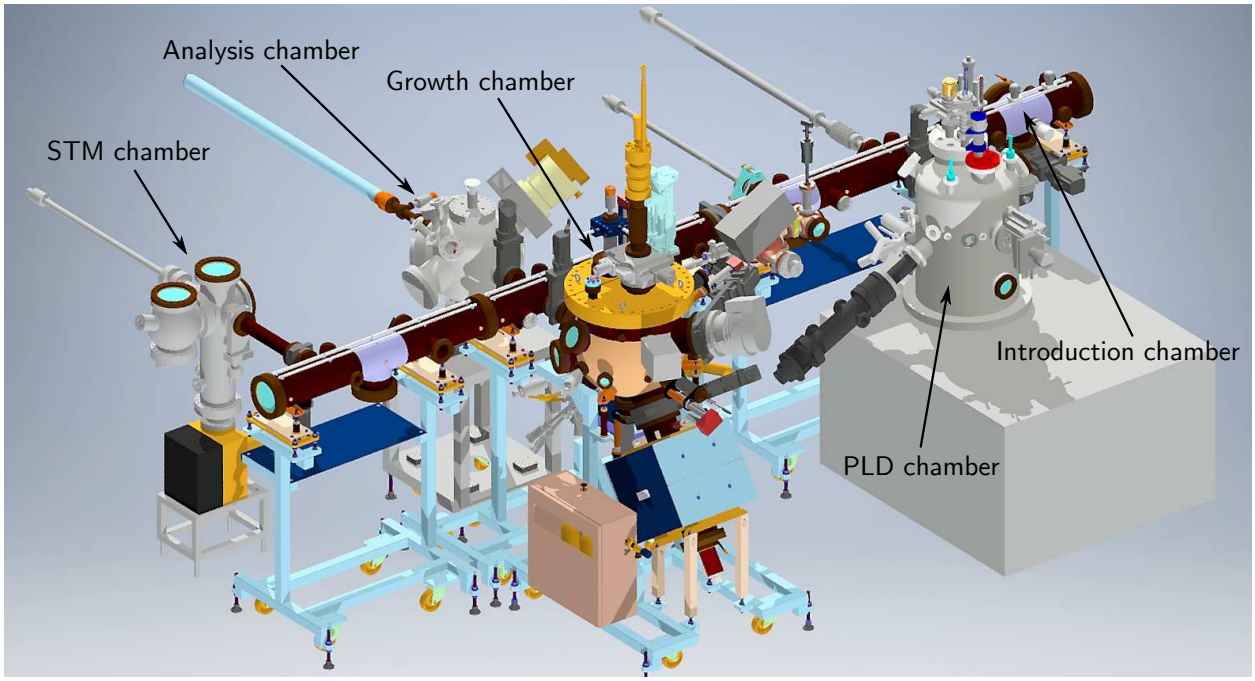

Figure 1.2: The UHV system is composed of 4 chambers connected by a transfer tunnel. From left to right, the STM chamber, the Analysis chamber, the Growth chamber and the PLD chamber.

1.2.2 Reflection High Energy Electron Diffraction (RHEED)

The RHEED measurements are used to get information on the surface structure of crystalline materials. Due to the grazing incident electron beam, the RHEED measurement is very sensitive to the sample surface or any adsorbate on top of it (including crystallography and morphology). In this thesis, we used RHEED measurements as references to check the quality of the surface and also to analyze the surface crystallography.

Working mechanism

In RHEED [104;117], a high-energy electron beam (generated by thermionic emission, typically of a few 10 keV - in our measurements in Chapter 5, we used E = 17 keV for all RHEED patterns) strikes the sample's surface at near-grazing incidence ($\approx 1^{o}$ via a focusing system based on electrostatic lenses) and reflect on a phosphorescent screen. Figure 1.3 (a) shows the Ewald construction allowing to predict the angular orientation of the diffracted beams.

Because of the short mean free path and glancing angle incident geometry of the electron beam, the diffraction patterns obtained are from the near-surface region. This means that the number of planes with a unit vector c in the direction perpendicular to the surface involved in diffraction is small, and the reciprocal lattice has a rod-like structure perpendicular to the surface.

The intersection between the Ewald sphere and the rods is in principle a set of points.

However, in practice, the electron beam is not strictly monochromatic and has a finite divergence, so the Ewald sphere is rather a shell, and imperfections in the crystal broaden the streaks. The result is that the RHEED pattern of an actually flat surface is usually a set of streaks perpendicular to the sample's surface (Fig. 1.3(b)).

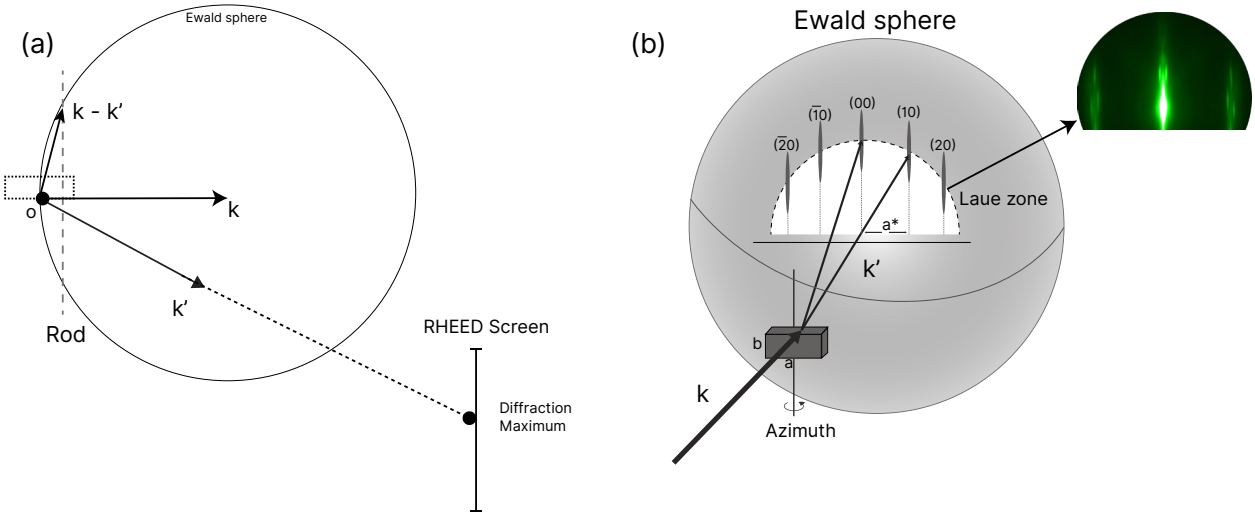

Figure 1.3: (a) Ewald construction of the diffraction condition, with the sphere defined by the X-ray wavevector's length as a radius, and the scattering vector an arc whose end coincides with the intercept between the sphere and a reciprocal space rod from the truncated crystal corresponding to the sample with its surface. (b) Three-dimensional view of the Ewald's sphere construction, with a set of first-order reciprocal space rods from the sample, yielding a series of diffraction streaks in the so-called first Laue zone, and a representative RHEED pattern obtained for a clean Au(111) surface with a herringbone surface reconstruction.

Experimental setup

In our setup measurement, the RHEED system is located in the growth chamber. The diffracted beams are visualized onto a fluorescent screen, and the pattern is acquired with a camera, which allows post-analysis of the RHEED patterns. The sample holder allows adjusting the angle of incidence of the electron beam and the relative orientation of the sample with respect to the direction of the beam (azimuth), so different sets of crystallographic planes can be selected to analyze the sample surface's reciprocal space.

1.2.3 Scanning Tunneling Microscope (STM)

In complement to RHEED experiments which give access to ensemble-averaged crystallographic data (the electron beam radius is about 1mm), we also have measurement by STM that provides images in real space at the atomic scale.

The STM was invented by Binning and Rohrer and later implemented by Binning, Rohrer, Gerber and Weibel. The first implementation rapidly allowed to resolve the famous (7×7)

reconstructed surface of Si(111)[15]. After the success of the STM, many other microscopes were invented such as the atomic force microscopes (AFM), the magnetic force microscopy (MFM) to name a few. For all of these measurements, the data are collected from a very sharp probe scanned over the sample's surface.

Working mechanism

Figure 1.5 shows the essential element of a STM setup. A very sharp metal tip is brought very close to the surface of the sample. Since the distance between the tip and the sample is of the order of 1 Å, the electron wavefunction in the tip and the sample overlaps. It creates a tunneling channel and by applying a voltage bias between the tip and the sample, a tunneling current is generated.

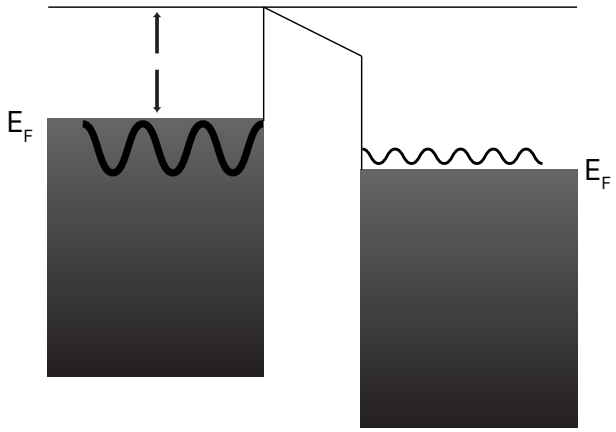

Figure 1.4: Schematics of the electronic wave-function in the tip and in the sample, and vacuum tunneling barrier under the application of a tunneling bias.

The tip is usually made of tungsten or Pt/Ir alloy and is conventionally chosen to be grounded, as a result, the voltage > 0 means the electrons are tunneling from the occupied states of the tip to the empty states of the sample. The tunneling current is then converted to a voltage by a current/voltage amplifier, which then can be used in a negative feedback loop to adjust the bias applied to the piezoelectric element that controls the tip-sample distance (z piezo), hence the tunneling current. The negative feedback is working as follows: if the tunneling current is larger than the chosen set-point, then the z piezo is contracted, thereby lowering the tunneling current, and vice versa. As the tip scans over the xy plane, the bias applied to the z piezo is measured. This constant current map can be converted into an apparent height map since the height is directly related to the tip-sample distance (see next paragraph) and z piezo extension. Note that the tunneling current is dependent on the local electronic density of states, which a priori varies for instance when the chemical nature of the surface changes.

The transmission coefficient T, which is the ratio of the tunneling current at the distance z and the current when the tip and surface is at contact is given by:

$$I = \frac{I(Z)}{I(0)} = e^{-2kz} \tag{1.2}$$

where $k = \frac{\sqrt{2m\Phi}}{\hbar} = 5.1\sqrt{\Phi}nm^{-1}$ is the decay constant, and m is electron free mass, Φ is the workfunction of the tip and the sample. I(0) is constant and the typical value of Φ is 5eV leading to a value of k about 11.4 nm^{-1}, which means that the decay is one order of magnitude per 1Å.

The STM images can also be compared to simulation. In brief, this method consists in calculating the partial charge density in an energy window corresponding to the measurement.

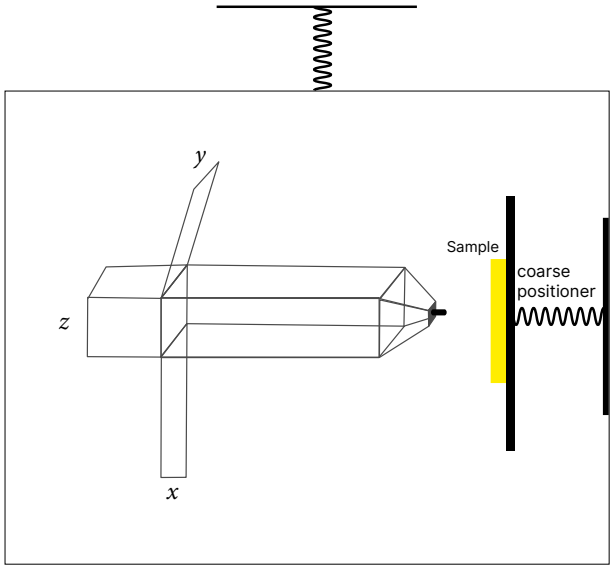

Figure 1.5: Basic principle of STM, when the tip scan over the sample.

STM setup

In the experimental result presented in this thesis, the STM measurements were performed under UHV condition with the base pressure of 10^{-11} mbar at room temperature. We used a commercial Omicron UHV-STM 1 with a W chemically-etched tip.

At first, the sample is mounted to the sample holder, the tip is placed close to the sample by the coarse positioning (as seen in Fig. 1.5), this process is automatized and stops when a tunneling current becomes measurable. As the tip travel along x and y directions with preconfiguration parameters, the constant height maps are printed to the display.

1.3 Conclusion

During my Ph.D., I coupled DFT calculations, growth samples and perform STM experiments. Coupling DFT and STM enable us to take advantage of the possibilities of the two approaches: high accuracy (including information on the chemical nature of the atoms) but model system for DFT and direct imaging of the real system for STM. Comparing the data to the simulations enabled us to discriminate between different kinds of defects (*Chapter* 3) or to get a better understanding of TMDC junctions (*Chapter* 4) and TMDC/Metal interfaces (*Chapter* 5).

Chapter 2

Transition Metal Dichalcogenides (TMDC)

Strictly two-dimensional (2D) materials were long thought to be unstable. This had been theoretically predicted and strongly supported by experimental observations[107]. Nevertheless, reports on TMDCs monolayer appeared back in the 80s, and even earlier for few layers MoS_2, but they did not raise strong interest at that time.[68] At the beginning of this millennium, the field reignited after the elaboration of graphene by Berger,[13] Zhang,[171] and Novoselov[115] and the exploration of its unique properties, such as an abnormal room-temperature quantum Hall effect. Since 2004 and graphene, the two-dimensional material family kept on growing with hBN, silicene, phosphorene, germanene, stanene, transition metal dichalcogenides... We focus here on TMDCs and more specifically on semiconducting TMDCs. The nature of their gap (direct/indirect) can be modified by varying the number of layers, or by strain. Nowadays, these materials are at the heart of intense research activities devoted not only to their intrinsic properties but also for practical applications one: optoelectronic properties[6], catalytic effects[152] superconductivity[123] or extremely large magneto-resistance,[5] etc. In this chapter, we compare some elementary properties, such as lattice constant, polymorphism, electronic structure, reported in the literature, with our own calculations performed by Density Functional Theory (DFT). We present some additional calculations on the lattice deformation and doping of the most studied TMDCs systems.

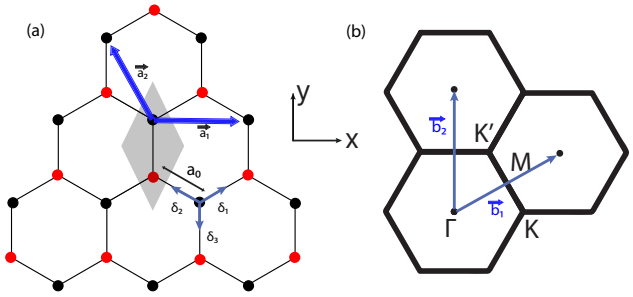

Figure 2.1: Graphene lattice structure (a) and its Brillouin zone (b). The triangular lattice with two lattice vectors a_1 and a_2, three nearest-neighbor vectors: δ_i, $i = 1, 2, 3$ are also indicated.

2.1 Two Dimensional Materials: Physics of Materials with Reduced Dimensionality

2.1.1 Graphene

The study of graphene created a premise for a new direction of research addressing more generally 2D materials. Among them, TMDCs have gained huge attention due to rich physics and great promise for applications.

Graphene is made of carbon atoms arranged on a honeycomb lattice. The honeycomb lattice is not a Bravais lattice: it is a triangular lattice with two atoms in the unit cell. The two translational vector can be chosen as (Fig.2.1):

$$\begin{aligned} a_1 &= (\sqrt{3}, 0)a_0 \\ a_2 &= (\frac{-\sqrt{3}}{2}, \frac{3}{2})a_0, \end{aligned} \tag{2.1}$$

where the parameter $a_0 = 1.42\text{Å}$ is the distance between two nearest-neighbors carbon atoms. The first Brillouin zone (FBZ) is hexagonal with a rotation of $\pi/6$ with respect to the original honeycomb lattice. The reciprocal space is constructed from two fundamental vectors:

$$\begin{aligned} b_1 &= \frac{2\pi}{a_0\sqrt{3}}(1, \frac{1}{\sqrt{3}}) \\ b_2 &= \frac{4\pi}{3a_0}(0, 1). \end{aligned} \tag{2.2}$$

Some special points are also noted in Fig. 2.1(b), these are the $\Gamma = (0, 0)$, the $M =$

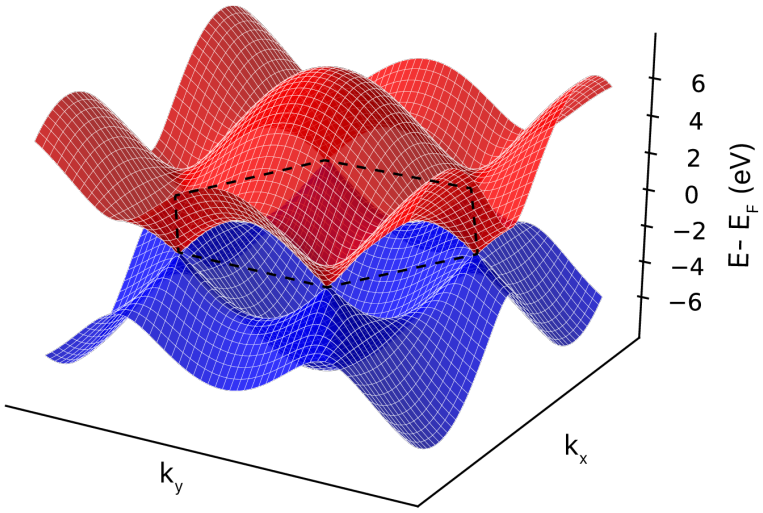

Figure 2.2: Graphene's band structure with respect to the Fermi level. The dashed hexagon indicates the first Brillouin zone.

$\frac{\pi}{a_0\sqrt{3}}(1, \frac{1}{\sqrt{3}})$ and the two inequivalent Dirac points:

$$\begin{aligned} K &= (\frac{4\pi}{3\sqrt{3}a_0}, 0), \\ K' &= (\frac{2\pi}{3\sqrt{3}a_0}, \frac{2\pi}{3a_0}), \end{aligned} \tag{2.3}$$

these two K and K′ are inequivalent because they cannot transform one to another by any linear combination of vectors of the reciprocal lattice.

P.R Wallace was the first one to describe graphene's band structure using the tight-binding approach and first neighbor interactions. The highest occupied and lowest unoccupied bands are shown in Fig. 2.2. They cross at the K points and have a linear and isotropic dispersion (Dirac cones) in an energy range of about 1 eV around these points. Graphene's very exciting electronics properties, for instance, the massless chiral Dirac fermion character of its charge carriers, are related to this band structure and to the honeycomb lattice.[150]

2.1.2 TMDC: from Bulk to Monolayer

TMD has an MX_2 formula with M a transition metal atom (Mo, W, etc.) and X a chalcogen atom (S, Se, and Te). These systems are made of triple layers where one plane of M is sandwiched between 2 planes of chalcogen. Within the plane, the TM-Chalcogen bonds

have a strong covalent character. The triple layers are stacked on top of each other thanks to (weak) van der Waals interactions. The thickness of this triple layers is in the range of 6-7 Å. Even if the primitive unit-cell consists of a triple-layer, these systems are still called monolayers (or single layers - SL). Metal atoms within a triple layer are six-fold coordinated and their bonding geometry can be either trigonal prismatic or octahedral.[26]

Because of the difference between intra- and inter-layer bonds, few layers down to SL TMDC can be isolated, like in graphite/graphene. Within the triple plane, the 2H TMDC, the most common polymorph, draw a honeycomb lattice (Fig. 2.3) like in graphene.

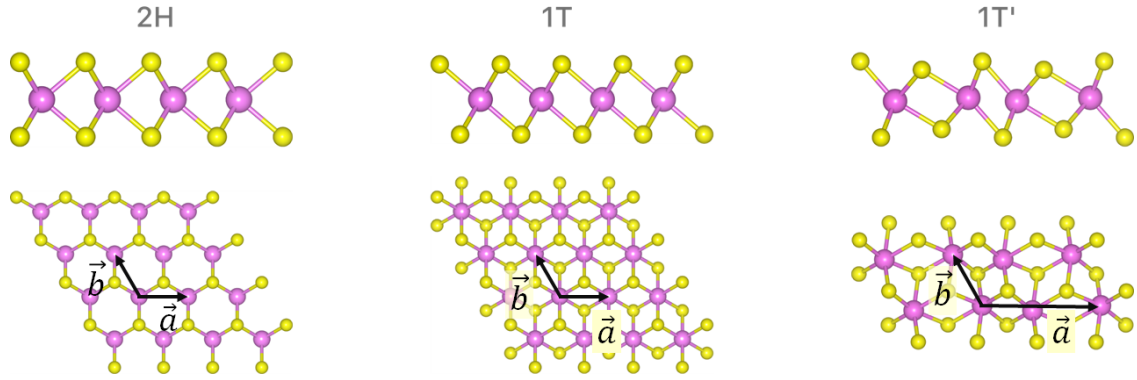

Figure 2.3: Three most common polymorphs of: TMDC 2H, 1T and 1T' phases. The in-plane lattice vectors for the primitive unit cell **a, b** are shown in the top views. Purple (Yellow) represent Metal (Chalcogen) atoms.

Different polymorphs exist that correspond to different local symmetry: trigonal prismatic (2H) where chalcogen atoms lay on top of each other and octahedral geometry where the 3 chalcogen atoms of the top layer are rotated by 180° with respect to the 3 chalcogen atoms of the bottom (Figs. 2.3 and 2.4). The terms H and T stand for hexagonal and trigonal symmetry of the crystal structure, respectively. Due to the differences in crystal symmetry, the H and T phases of TMDCs have substantially different electronic structures as we will show in the next paragraph. The 1T' phase is the modulation of the 1T phase in one direction that corresponds to a 2×1 superstructure (Fig. 2.3).

In general, group VI TMDCs take the 2H structure but there is some exception e.g. WTe_2 which adopts the 1T' phase like group VII TMDCs and some group VI TMDCs in special conditions of stress or electron doping. Group IV (ReS_2) and most of the group V TMDCs have a 1T structure[74].

Figure 2.4 shows top and perspective views of 2H and 1T phases. For both structures the two Bravais primitive lattice can be chosen as in graphene as:

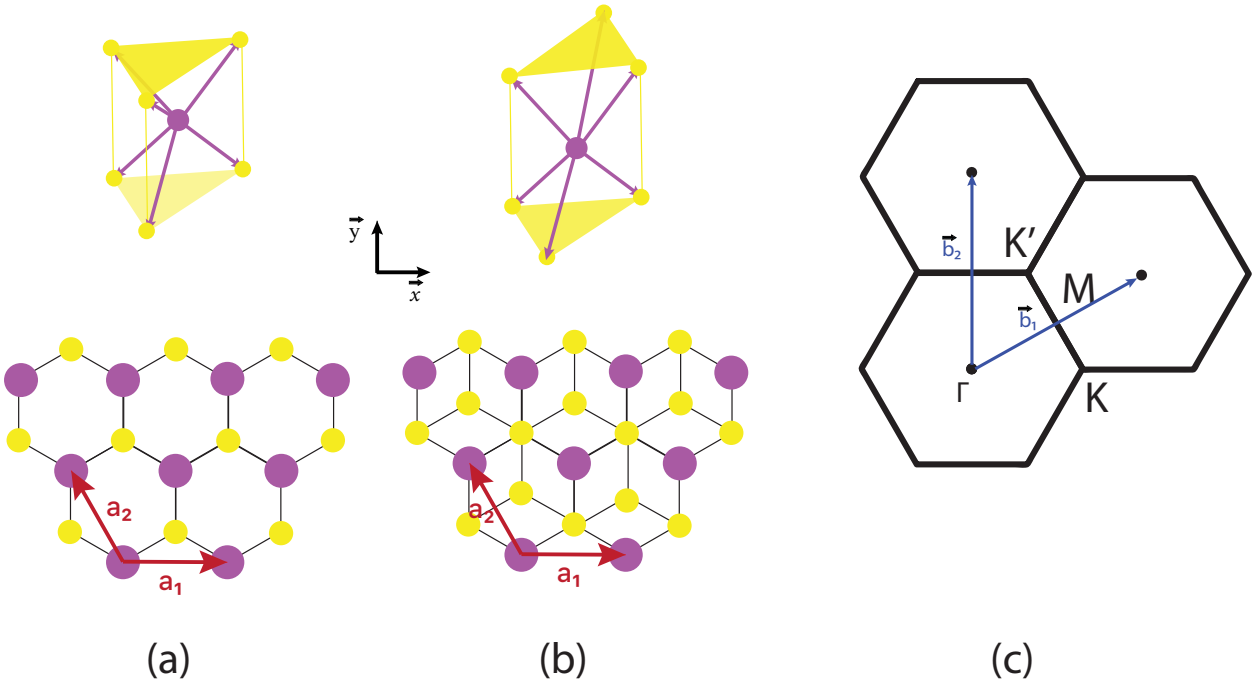

Figure 2.4: Top and three-dimensional views of the (a) 2H and (b) 1T MoS_2 lattice structures, Purple (Yellow) disks represent Mo (S) atoms. The two Bravais lattice vectors are indicated in red. Notice that in (a) two chalcogen atoms sit on top of each other. The Brillouin zone is shown in (c) with reciprocal lattice vectors in blue.

$$\begin{aligned} a_1 &= (a_0\sqrt{3}, 0, 0), \\ a_2 &= (\frac{-a_0\sqrt{3}}{2}, \frac{3}{2}a_0, 0), \end{aligned} \tag{2.4}$$

where the parameter a_0 is the distance between two nearest-neighbors M-M (or X-X) atoms. A single unit cell contains 1 M atom at $(0, 0, 0)$ and 2 X atoms. In the case of 2H stacking, the two X atoms are mirror reflection with respect to the plane of M atoms, they are separated by several Å and their coordinates as a function of (a_1, a_2) are $(\frac{1}{3}, \frac{2}{3})$. For a 1T stacking, the two X atoms stay on each side of the M atom plane, and their coordinate are $(\frac{1}{3}, \frac{2}{3})$ and $(\frac{2}{3}, \frac{1}{3})$. Structural data for different TMDCs are shown in Table 2.1, our results were obtained by DFT using VASP [82] and the generalized gradient approximation (PBE) for the exchange and the correlation energy for neutral but also doped systems. The energy cutoff and the Brillouin zone sampling were chosen to converge the total energy with values of 600 eV and 6×6×1 (6×6×6) in case of bilayer (bulk). Similar results were also found in references [84;96;131]. From Table 2.1, one can see that changing the chalcogen atoms leads to a substantial increase in the lattice constant in MX_2 system. TMDCs with the same chalcogen atom have very similar lattice vectors. This is of high importance for the formation of heterojunctions as

described in *Chapter* 4.

Table 2.1: Lattice parameters of TMDC compounds from our VASP calculations, in which $d_{\angle S-\angle S}$ (Å) is the distance between two chalcogene layers and d_{M-S} is the distance between metal and chalcogene atoms. Total energy per chemical formula is given for direct comparison ($\frac{E}{2}$ for 1T' phase).

	a_0(Å)	$d_{\angle S-\angle S}$ (Å)	d_{M-S} (Å)	Total ENERGY (eV)
MoS_2 (2H)	3.18	3.12	2.41	- 21.81
MoS_2 (1T)	3.19	3.17	2.43	-21.02
MoS_2 (1T')	6.45 × 3.19	2.71 / 3.48	2.38 / 2.48	-21.27
$MoSe_2$ (2H)	3.32	3.34	2.54	-20.76
$MoSe_2$ (1T)	3.27	3.46	2.56	-20.07
$MoSe_2$ (1T')	6.58 × 3.27	2.96 / 3.77	2.5 /2.6	-20.37
$MoTe_2$ (2H)	3.55	3.62	2.74	-18.79
$MoTe_2$ (1T)	3.49	3.74	2.75	-18.27
$MoTe_2$ (1T')	6.98 × 3.49	3.62 / 4.09	2.71 / 2.78	-18.70
WS_2 (2H)	3.19	3.14	2.42	-25.69
WS_2 (1T)	3.21	3.15	2.43	-24.89
WS_2 (1T')	6.44 × 3.22	2.97 / 3.29	2.30 / 2.46	-24.99
WSe_2 (2H)	3.35	3.34	2.56	-23.68
WSe_2 (1T)	3.29	3.45	2.57	-22.95
WSe_2 (1T')	6.58 × 3.29	2.94 / 3.82	2.54 / 2.60	-23.35
WTe_2 (2H)	3.56	3.63	2.74	-21.50
WTe_2 (1T)	3.52	3.69	2.75	-20.94
WTe_2 (1T')	7.04 × 3.52	3.01 / 4.22	2.73 / 2.82	-21.55

In addition to these two fundamental phases, distorted phases have also been found. Back

in 1973, to study superconductivity in TMDCs, Somoano intercalated MoS_2 with alkali atoms and showed it results in strong layer displacement[137]. The layered displacement, in reality, could be explained by a combination of disordered compounds. A new phase with octahedral coordination and a 2×1 supercell was observed later on[124;134]. The existence of a 2×1 superlattice was again confirmed by Heising by electron diffraction in 1999[56]. Since it shared similar symmetry with the 1T phase, this phase was called 1T'. It is shown in Fig. 2.3. To get more detail about the crystal structure and test calculation parameters, we performed DFT calculations to retrieve the lattice configuration of the 1T' polymorph. The relaxed primitive cell of 1T' phase has 6 atoms and shows distortion in the 3 directions. One can specify the two Bravais primitive lattice for the 1T' phase:

$$\begin{aligned} a_1 &= (2 \times a_0\sqrt{3}, 0, 0), \\ a_2 &= (\frac{-a_0\sqrt{3}}{2}, \frac{3a_0}{2}, 0). \end{aligned} \tag{2.5}$$

In case of the MoS_2 1T' phase, the three Mo-Mo nearest distances are 2.75, 3.19 and 3.73 Å, compared to 3.19 Å in case of 1T MoS_2. The Mo-S distances vary between 2.38 and 2.48 Å, compared to a uniform 2.43 Å of 1T-MoS_2. The results are in very good agreement with a previous report.[124] It must also be noted that, aside from the 2×1 super lattice structure, a 2×2 super lattice-1T" was found, with also a significant distortion.[27;28]

Other groups also studied intercalation of TMDCs with alkali atoms and showed that lithium intercalation in 2H MoS_2 transforms the structure into 1T[124] or 1T′[142] depending on the fabrication environments. The intercalation process can have difference effects, namely, charge transfer and strain. To model and also to evaluate the relative stability of different phases, we calculated the total energy of different TMDCs with different doping levels (neutral, +1 and -1 electron) and different lattice constants (to mimic the biaxial strain). The results for MoS_2 are shown in Fig. 2.5. Positively charged systems show strong energy variations, and we will not discuss them in the following but focus on neutral and electron doped TMDCs. Since the lattice constant of MoS_2 is 3.18 Å, the area of a primitive cell corresponds to 8.78×10^{-16} cm^2, one electron removed and added to the system will make a hole or electron doping density of $n^{\pm} = 1.14 \times 10^{15}$ cm^{-2} a very large value, typically 10 times larger than accessible with e.g. liquid ion gates. As shown in Fig. 2.5, for a specific charge state, the energy E exhibits a quadratic dependence on lattice constant, and by definition, the equilibrium lattice constant corresponds to the minimum of E. The 2H phase has the lowest energy minimum for neutral and electron doped case. In MoS_2, adding electrons could help the transition from 2H to 1T' phase since it reduces the energy difference.

The same results for different MX_2 (M: Mo and W and X: S, Se, Te) are shown in

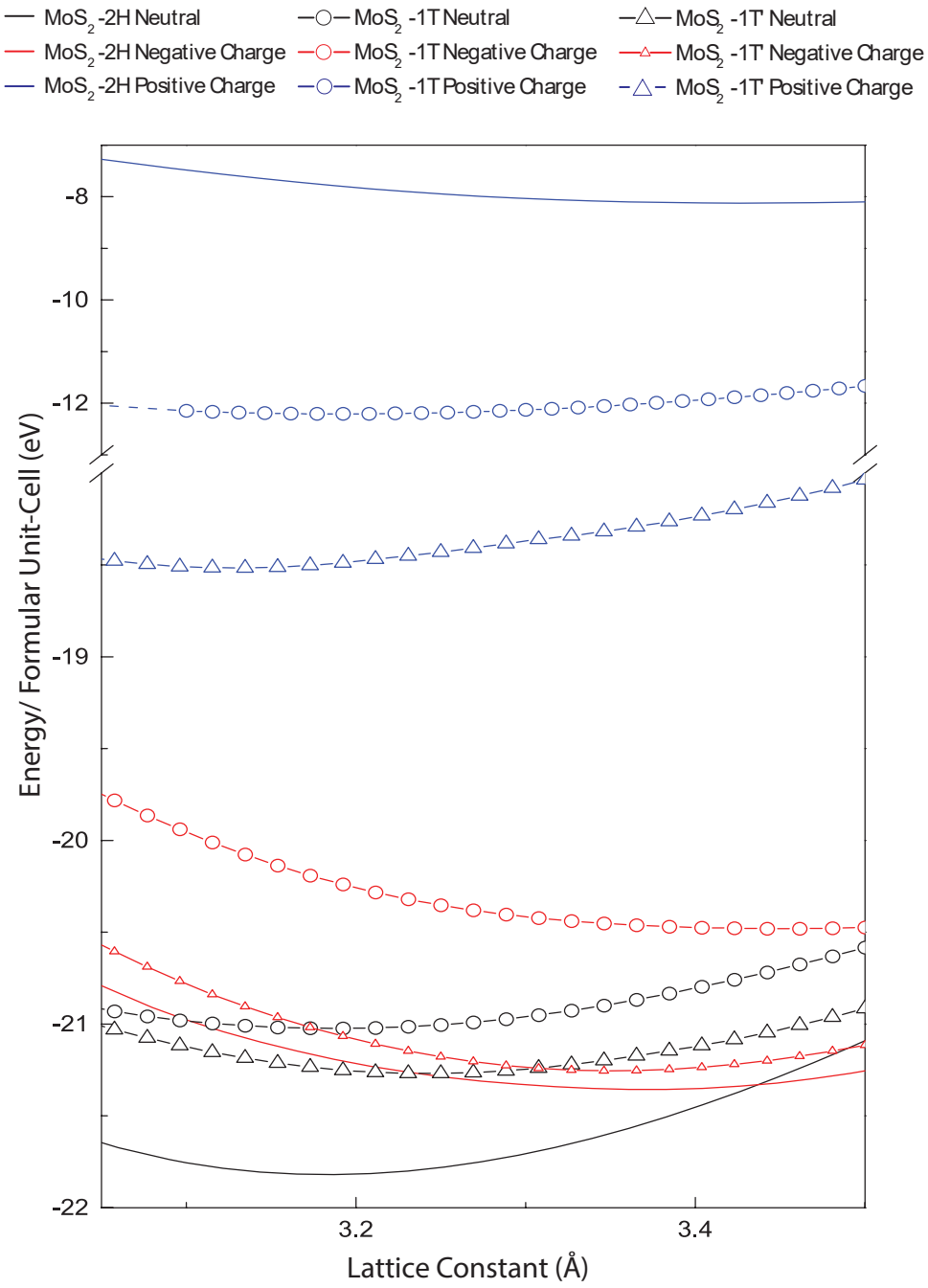

Figure 2.5: Free energy as a function of lattice constant in MoS_2 with different phases 2H, 1T and 1T', for different phases and 3 electron doping levels: negative (-1 e), neutral and positive (+1 e). The charged system is calculated with a compensating homogeneous background to keep the system neutral. As energy is lower, the system is more stable. For 1T′, the structure is achieved by relaxing the superstructure 2×1 from the 1T phase with a small displacement of one Mo atom with respect to the other. It's also worth to note that, the energy and the lattice constant of 1T' phase is averaged by number of unit formula.

Fig. 2.6. A similar trend is observed for all MX_2. In most neutral cases, the 2H phase is the equilibrium state, except for WTe_2, where the 1T' phase is more favorable than the 2H phase. This is in a very good agreement with the literature[20]. The optimized lattice

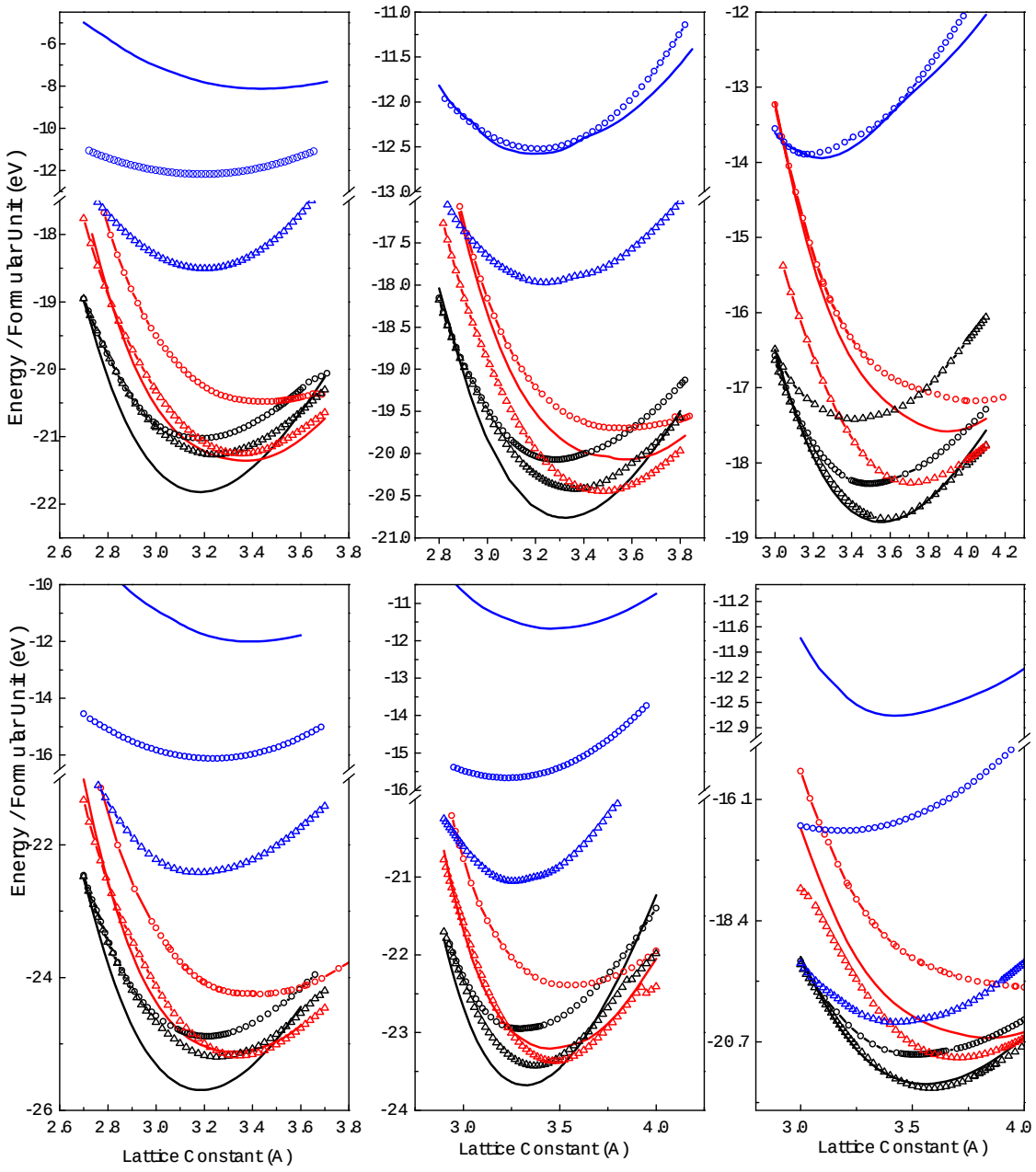

Figure 2.6: Our calculations show the evolution of energy E vs. lattice constant at three difference electron doping levels, negative (-1 e), neutral and positive(+1 e) for MoS_2, $MoSe_2$, $MoTe_2$, WS_2, WSe_2 and WTe_2.

parameter changes with doping. In agreement with Ouyand *et al.*[119] the 1T phase always has the highest energy. In our calculation the 1T' phase has the lowest energy when doped with electrons except for the MoS_2 system where the 2H phase remains the most favorable one. It should be noted that energies for different states of charge cannot be compared for technical reason (VASP).

As previously said, a single layer of TMDCs is made of 3 atomic layers, and within these three layers M-X bonds are covalent. Single layer TMDC can be stacked-up to become

bilayer, trilayer, etc. Figure 2.7 shows the stacking of 1T and 2H phases in bulk, the prefix digit in 1T and 2H defines the number of layers in the bulk unit cell. In the bulk, these layer are stacked on top of each other, thanks to weak van der Waals (vdW) forces. [1] The weak vdW forces allow the formation of ultra-thin layers of TMDC by micro-mechanical cleavage technique, as demonstrated in MoS_2 by Novoselov *et al.*[115].

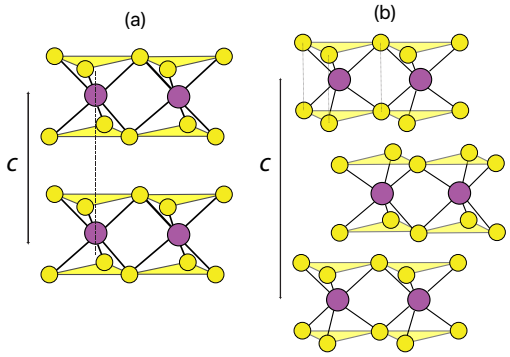

Figure 2.7: Bulk polytypes of TMDCs, (a) 1T phase and (b) 2H phase.

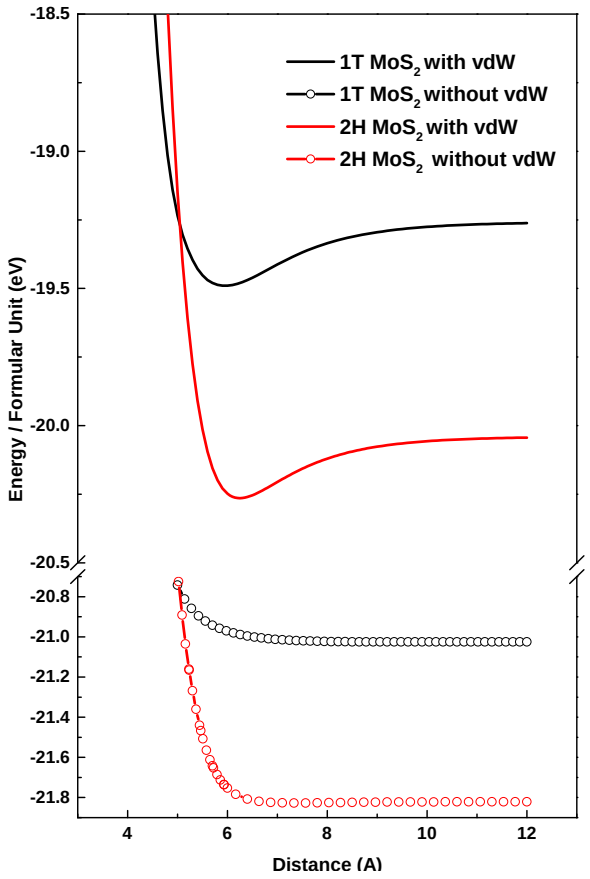

Figure 2.8: Our DFT calculations show the free energy as a function of c in difference cases.

Standard DFT calculations do not properly take into account van der Waals interactions.

[1] The vdW forces help geckos to walk on a wall.

Figure 2.8 compares the variations of the energy as a function of the interlayer distance in bulk 1T and 2H MoS_2, from calculations based on standard DFT with PBE functional[121] or DFT+PBE and van der Waals correction[50]. A real minima is found only when van der Waals interactions are included. In fact, not taking into account the vdW interaction could give nonphysical results.[132] In the next chapters since we are dealing with monolayers only, vdW interactions are not included.[73]

Beside these most common bulk polymorphs, others may exists[70] such as the 3R phase — as it name suggests, it is a crystal with 3 layers per unit-cell, rhombohedral symmetry and with trigonal prismatic coordination, the 1T″ phase - another distortion phase from 1T phase, where modulation of M atoms are in both $\mathfrak{x}$ and $\mathfrak{y}$ directions. Some TMDCs can be found in mixture of multiple polymorphs.

2.1.3 Electronic Properties

TMDCs show very exciting electronic properties, especially for SL. They also show a large spin-orbit splitting at the valence band. For those reasons, in the past few years, many studies on the electronic properties of TMDCs have been published both from simulation and experiment. In the case of simulations, first principle calculations have been widely used from the GW approximations[127], to DFT and tight-binding simulations[95;96]. In the case of experiment, multiple methods have been used to tackle different facets of the electronic properties, among them direct band gap in monolayers was first demonstrated by PL[106] and ARPES measurements[133]. In this part, the electronic structure of TMDC is presented for bulk, bilayer and SL, based on our calculations that are compared to results from the literature. Some experimental results from literature are also described.

Simulation approach

TMDCs in the 2H phase are semiconducting while they are metallic in the 1T phase.[37;106;140] Figure 2.9 shows the density of states (DOS) of MoS_2 SL with different polymorphs, 2H, 1T and 1T'. A gap of 1.68 eV in SL 2H phase demonstrates its semiconducting character, there is no gap in the 1T phase (it is metallic), and for 1T' phase we obtained a tiny gap of ≈0.05 eV. Our results are in good agreement with the literature[23;88].

Bulk 2H TMDCs are indirect band gap semiconductors. When the thickness decreases to a SL a direct band gap is found[88;91;106;131] with the valence band maximum (VB) and the conduction band (CB) minimum at the K-points of the Brillouin zone.

To get a better idea of how the electronic structure behaves in different configurations, we performed DFT calculations of the band structure of 2H MoS_2 . Figure 2.10 shows

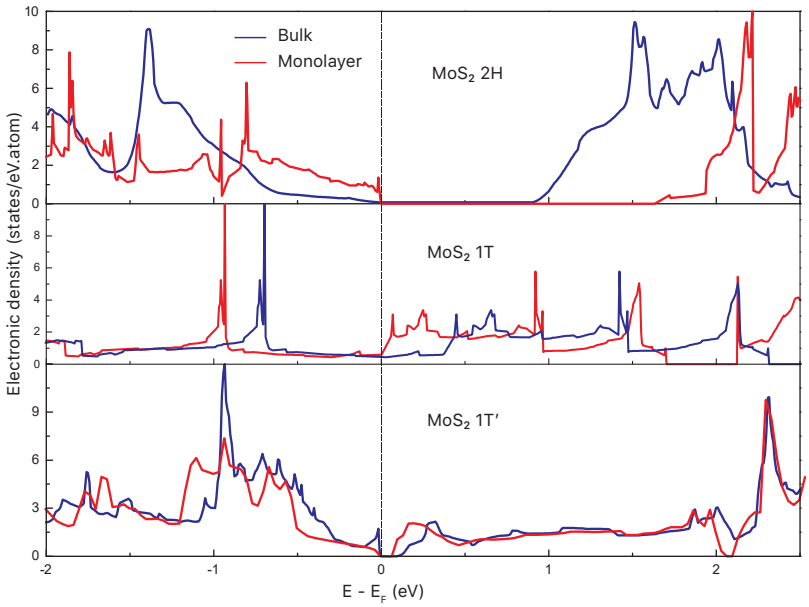

Figure 2.9: Our calculations on electronic density of states of the SL 2H, 1T and 1T' phases of MoS_2 from our calculations.

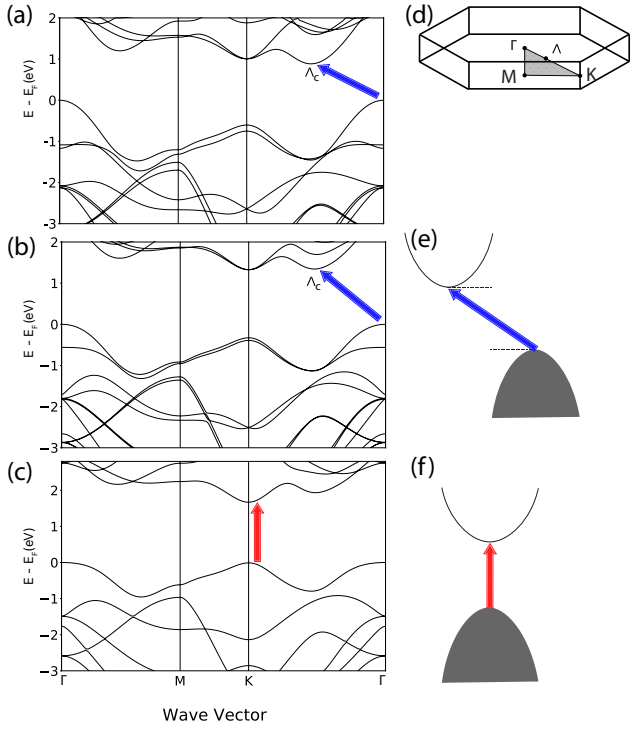

Figure 2.10: Our DFT calculations show the electronic band structure of (a) bulk, (b) bilayer and (c) SL of MoS_2. (d) First Brillouin zone and some high symmetry k—points, in which Λ is between of Γ and K. Red (Blue) arrows visualize the direct (indirect) band gap in SL (bi-layer and bulk) band structure.

the evolution of the band structure of 2H MoS_2 with different number of layers, from bulk phase to bilayer and SL. The positions of valence band and conduction band edges show a

progressive change upon decreasing thickness, as the indirect band gap semiconductor turns into a direct band gap semiconductor.

According to our DFT calculations, the bandgap of MoS_2 2H bulk and SL are 0.89 eV and 1.68 eV. GGA is known to underestimate the band gap, by using Hybrid functional to the calculations, other groups obtained a gap of about 2.1 eV[131], in good agreement with some experimental values[106].

All calculations agree with a maximum of the VB located at the K points for SL and Γ for more than one layer and a minimum of the CB at K for SL whereas the position of the minimum of the conduction band is not so clear for more than one layer. In our calculations, we find it at the Λ_C point [2]. Strain was proposed to play a major role for the location of the minimum[120].

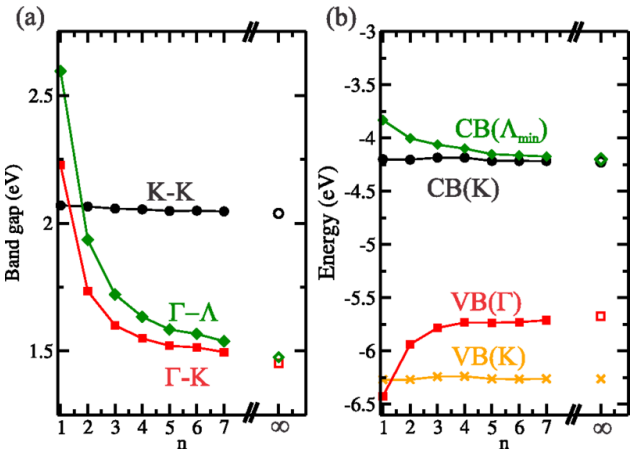

Figure 2.11: (a) The calculated values of band gaps by GW calculations with respect to the number of layers (n), and (b) band edge positions as a function of number of layers. Reproduced from[120].

In a SL, the difference in energy between the top of the VB Γ_V and the second highest state at K_V is very small while it is much larger and with a changed ordering for 2 and more layers. The difference in energy between the bottom of the conduction band at Λ_c and K_C is very small in the bulk and much larger in a SL.

To summarize, when decreasing the number of layers, the electronic structure experiences two processes: (1) the band gap widens from 0.89 eV to 1.68 eV (in our calculation with simple PBE) and (2) there is a transition between indirect to direct band gap. To understand the origin of the indirect-direct transformation and also of the gap widening, following Padhila *et al.*[120], we analyze the character of the states in the vicinity of the Fermi level Fig. (2.12). Close to E_F, bands have a $Mo_d - S_p$ character. States at K (CB and VB edges) have a nearly constant energy from bulk to SL while the energy of the conduction band edge at Λ_C decreases and of the valence band at Γ_V increases when layers are added (Fig. 2.11[120]).

[2] In our multilayer calculations, if the vdW is taken into account, the CBM switched from K_C to Λ_c

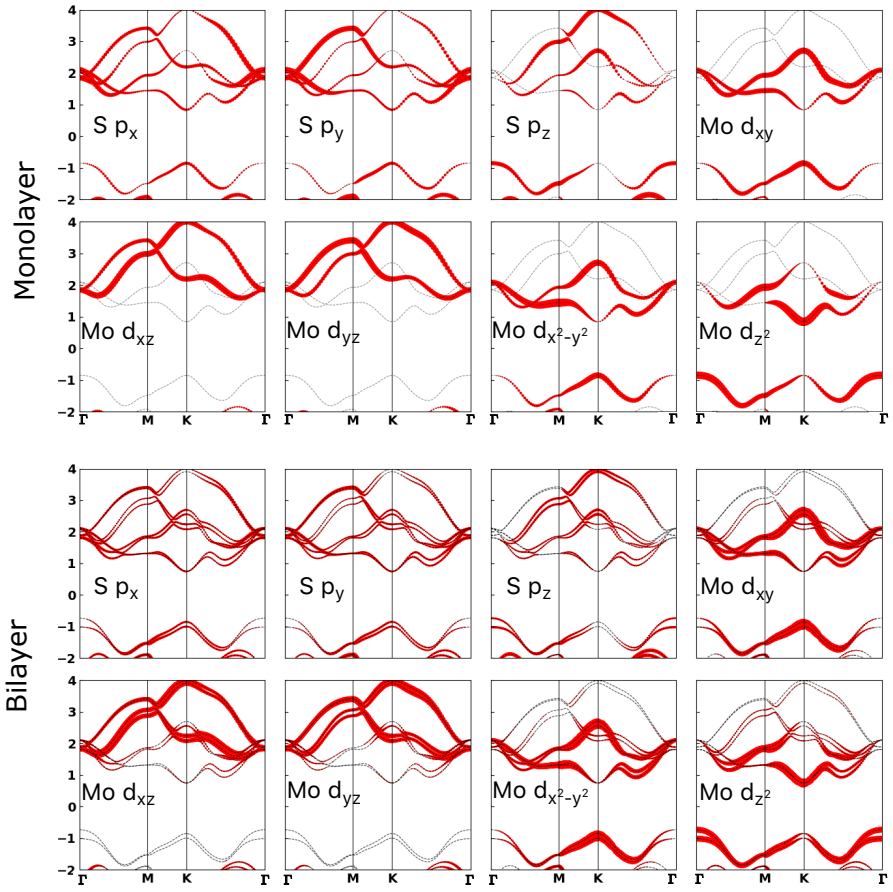

Figure 2.12: Our calculations show the orbital projected of SL and bilayer MoS_2. Size of the red dots indicate the strength of orbitals contribution. The s orbitals are not presented due to small contribution.

The analysis of the band structure shows that one layer gives one band on each side of the gap. They are split at K_V, Γ_V and Λ_C for more than one layer due to interlayer interaction while the CB edge at K-points shows no visible splitting, due to the fact that interaction is not possible by symmetry[120]. States at the top of the valence band at K have a $Sp_{x,y}$ and $Mod_{xy}, Mod_{x^2-y^2}$ in plane character that are not much affected when TMDC layers are added (due to weak interlayer interaction). These last two points explain the small variation of the energy positions of the lowest states at K_V and K_C and of the gap at K when going from bulk to SL.

On the contrary, states at Γ_V have a Sp_z and Mod_{z^2} out of plane character. For more than one TMDC layer, the corresponding states interact strongly and the bands are split in bonding and anti-bonding bands. The highest occupied band has an anti-bonding character and is pushed towards higher energies when layers are added which means that the maximum of the valence band goes from K to Γ when going from SL to two or more layers.

The same kind of arguments holds for states at Λ where one layer gives one band that becomes split in presence of an interlayer interaction.

Spin orbit coupling

All our calculations presented up to now do not take spin orbit coupling (SOC) into account. Spin-orbit interaction or spin-orbit coupling is the interaction between the spin of the electron and its angular motion.

In TMDC systems, the Kramer's degeneracy $[E^{\uparrow}(\vec{k}) = E^{\downarrow}(\vec{k})]$ in the MX_2 bulk comes from the combination of time-reversal symmetry $[E^{\uparrow}(\vec{k}) = E^{\downarrow}(-\vec{k})]$ and inversion symmetry $[E^{\uparrow}(\vec{k}) = E^{\uparrow}(-\vec{k})]$, thus SOC induces no splitting.[176] However, due to the absence of inversion symmetry in an MX_2 SL, spin splitting is observed except for some special symmetry $\vec{k}$ points in the Brillouin zone.

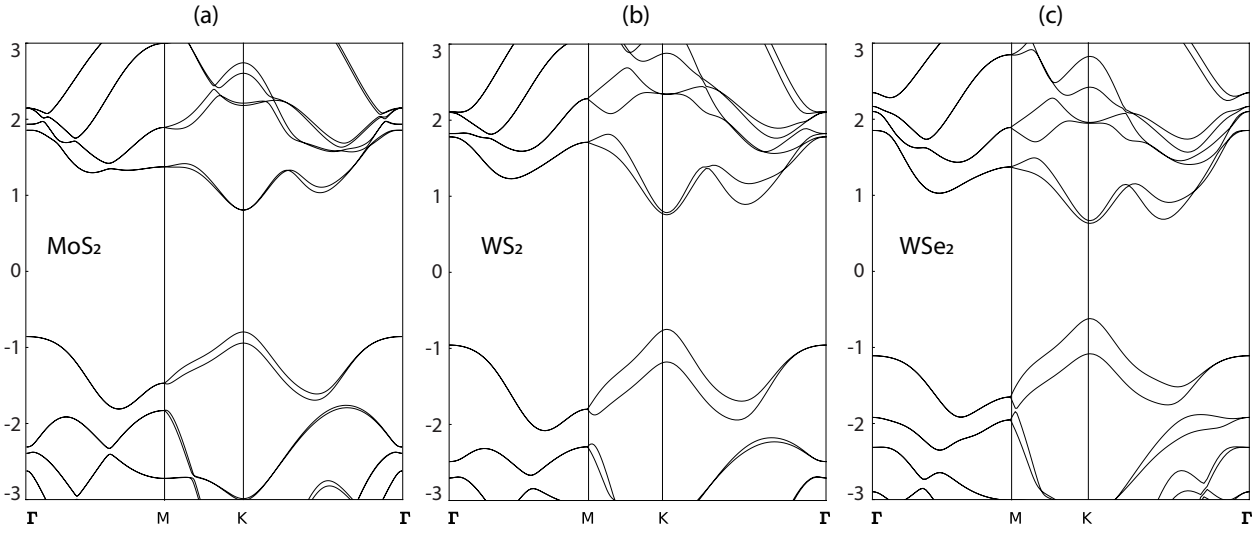

Figure 2.13: Our calculations on band structures with spin orbit coupling of (a) MoS_2, (b) WS_2 and (c) WSe_2 calculated by enabling the spin orbit interaction in VASP.

For instance, the bands are spin-degenerated at the Γ point due to time-reversal symmetry alone.[176] A combination of time-reversal and translational symmetry results in no splitting at the M point, whereas the spin splitting of a general $(\vec{k})$ point is determined by time-reversal and the point-group symmetry of the trigonal prismatic crystal. As shown in Fig. 2.13, the SO interaction breaks the spin degeneracy of the valence and the conduction bands along the line $\Gamma \rightarrow M \rightarrow K \rightarrow \Gamma$ of MoS_2, WS_2 and WSe_2. These materials exhibit a similar behavior but different magnitude of the spin splitting. The maximal spin splitting of the VBM in our calculation at the K_V-point is 148, 420 and 456 meV for the MoS_2, WS_2 and WSe_2, respectively.

The spin splitting at K_C are tiny (less than 4 meV) in comparison with the splitting at K_V. At the Λ_C, the large spin splitting is also found with the values of 70, 270 and 230 meV for MoS_2, WS_2 and WSe_2, respectively.

This SO splitting and the inversion symmetry breaking lead to coupled spin and valley

physics in group IV dichalcogenides,[160] for instance the valley K (-K) is associated with the spin up (down) only. The spin valley-dependent leads to very interesting properties such as the valley Hall effect.[160] It is worth noticing that including the SOC in DFT calculations demands a lot of computational effort, since we are working with very large unit-cell, the SOC is not taken into account in the next chapters.

Experimental approach

Up to now, several experimental methods have been used to characterize different TMDC electronic properties, such as photoluminescence (PL), STM (STS), Raman spectroscopy.

Despite its extreme thinness, TMDC SLs absorb light strongly. That is shown in multiple measurement of the optical band gap (which differs from the electronic band gap we discussed so far, due to the binding energy of the electron-hole pairs that recombine to emit a photon). One of the first studies on strong light absorption of TMDCs is the one published by Mak *et al.*[106]. In their report, the authors measured photon emission under the excitation of a light-source with an energy larger than the band gap energy of the material. The authors showed a substantial absorption enhancement in MoS_2 SL (Fig 2.14(a)). An intense bright PL peak at 1.9 eV in ML MoS_2 was detected at variance to the case of BL MoS_2, which is attributed to the fact that BL MoS_2 is an indirect band-gap semiconductor.

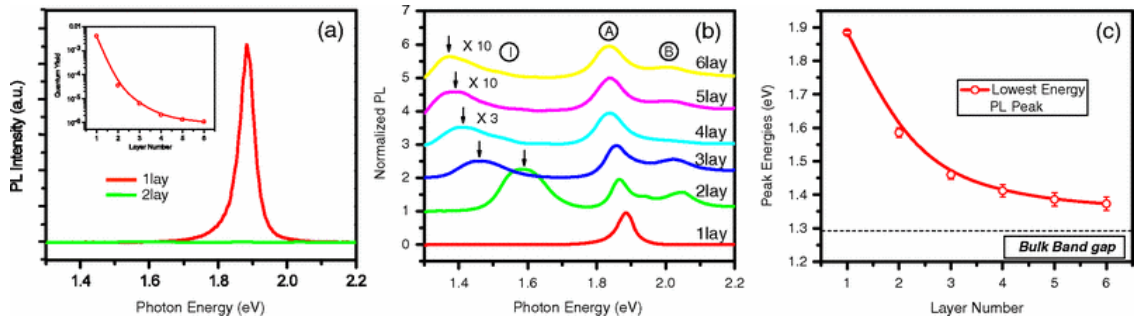

Figure 2.14: Photoluminescence spectra for (a) mono and bilayer MoS_2 measured in the photon energy range from 1.3 to 2.2 eV. (b) Normalized PL spectra by the intensity of peak A as a function of number of MoS_2 layers. And (c) band-gap energy of thin layers of MoS_2. Reproduced from Ref[106]

The electronic band gap of TMDCs was also studied by several groups. Two very popular methods to characterize the morphology and electronic structure are scanning tunneling microscope (STM) and scanning tunneling spectroscopy (STS). For instance, MoS_2 SL on highly ordered pyrolytic graphite (HOPG) has an electronic band gap of 2.15 or 2.35 eV at 77 K depending on criteria chosen to define the edges of the valence and conduction band (below/above which a certain tunneling current is measured).[167] Figure 2.15(a) shows a typical STM image of MoS_2 SL. The MoS_2 flake has the triangular shape and the height of

the flake is 0.67 nm corresponding to a SL MoS_2. Fig. 2.15(b) shows the band gap of MoS_2 SL that appears when measuring the differential tunneling conductance as a function of the tip-sample bias (STS measurement). The VBM is located at -1.81 V and the CBM is located at 0.3 V. A statistical analysis on different locations of the samples yields an average band gap value of 2.15 ± 0.06 eV. Other groups studied TMDCs grown on metallic substrates. For instance, Sørensen *et al.* measured MoS_2 on Au substrate and the STS measurements showed a quasi-particle band gap in this case of 1.8 eV[139].

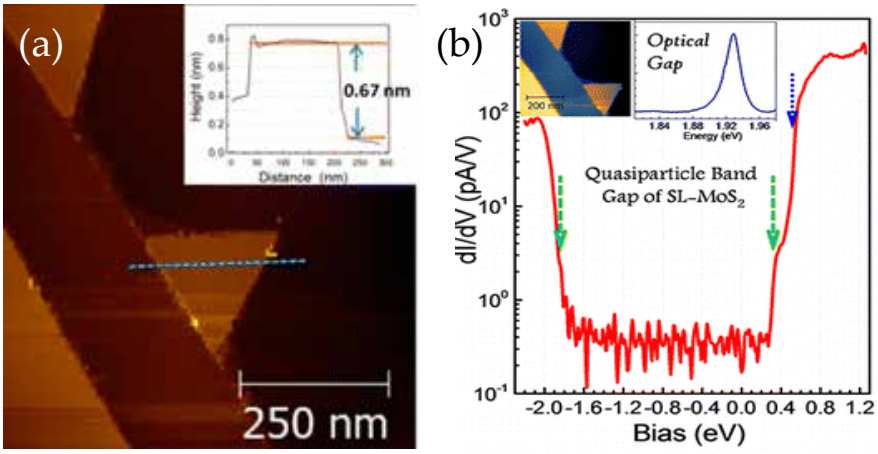

Figure 2.15: (a) STM image of a triangular ML flake with the height of 0.67 nm. (b) Typical scanning tunneling spectra on a SL MoS_2 flake. Reproduced from[167]

The origin of the different values of the band gap found with different substrates is unclear at this stage. Certain substrates may have a significant interaction, not simply van der Waals, with the SL MoS_2, with in some cases an hybridization of some the electronic bands of the two materials. This may result in a modification of the energy of some electronic bands of MoS_2, hence of the electronic band gap if for instance the valence or conduction band is more affected than the other. Similar studies for different TMDCs were also performed, for instance, $MoSe_2$ SL on bilayer graphene showed a band gap value of 2.18 eV at 5K, and $MoTe_2$ a gap of 0.96 eV at 77 K.[145] Beside gap-less and metallic substrates, insulators such as hBN, SiO_2 were used as a buffer layer for practical devices.

2.2 Preparation of TMD Monolayers

Two-dimenional TMDCs are usually fabricated following two classes of approaches: the top-down route, whereby bulk crystals are exfoliated into thin or even single-layer flakes, and the bottom-up method where crystals are grown from molecules/atoms by chemical vapor deposition or molecular beam epitaxy.

2.2.1 Top-down technique

Mechanical Exfoliation

To date, the mechanical exfoliation method is the most widely used approach to prepare thin, high quality samples. The first mechanical exfoliation was developed to exfoliate single and few layers of graphene and TMDCs (MoS_2, $NbSe_2$). The idea behind mechanical exfoliation is rather simple: due to the vdW force, the neighboring TMDC layers are weakly bond to each other, and these forces can be overcome with a mechanical force. In brief, adhesives (Scotch tapes) were used to peel TMDC layers from their bulk material. The process repeated multiple time to isolate few or even single layers. Finally, the cleaved 2D material stuck on the Scotch tape is brought into contact with a target substrate where part of the exfoliated flakes will adhere.

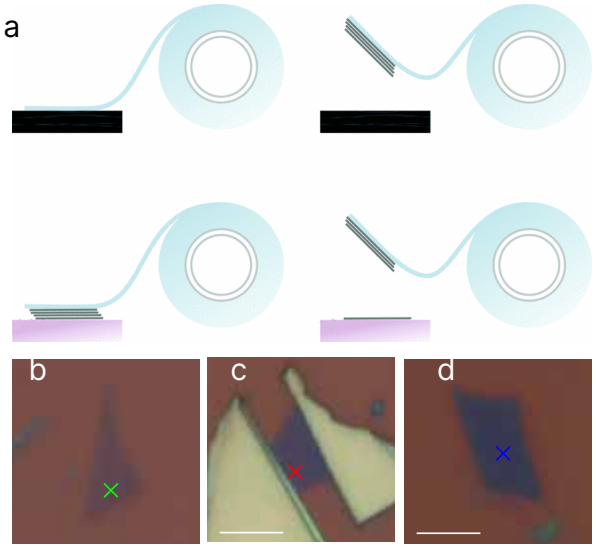

Figure 2.16: (a) Schematic of a mechanical exfoliation process. (b-d) Optical micrographs of single, bi-, and tri- layer of MoS_2 flakes exfoliated on SiO_2 with Scotch tape. Reproduced from Dubey *et al.*[35]

Multiple substrates have been used to exfoliate the TMDC single and few layers, including SiO_2/Si,[90] and Polydimethylsiloxane (PDMS)[35]. The mechanical exfoliation is cheap compared to other approaches, however, it also contains some drawback. The size/shape/thickness is difficult to control, the size is usually below the millimeter scale, contamination cannot always be avoided, overall making the technique so far unsuited to large-scale applications.

In addition to the exfoliation in ambient temperature/pressure, the nanomechanical cleavage was also performed under protective environments (glove boxes), and under the objective lens of an optical microscope in order to have better control on the number of layers and positioning of the flakes.[102;143]

Liquid Exfoliation

Exfoliation can be done in a solution via agitation (such as shear, ultrasonication, or thermal). This was first used to disperse graphene and later also applied to fabricate single or few layers of several TMDCs, such as MoS_2, WS_2 etc,[29;58]. In these fabrication processes, ultrasonic waves generate bubbles that collapse into high energy jets, breaking up the layered crystallizes and producing exfoliated nanosheets.[112] The solvents play an important role in the quality of the exfoliation: for instance, for the solvents that have surface energy similar to that of layered materials, the energy difference between the exfoliated and re-aggregated states will be very small, and so will be the driving force for reaggregation.[29]

Liquid exfoliation can also be done with the help of guest atoms/molecule, usually small ions (eg. Li^+[37], iodine bromide (IBr)[136]) are intercalated into the interlayer spacing of the bulk TMDC thereby weakening the interlayer adhesion and reducing the energy barrier to exfoliation. The intercalants also transfer charges to the layers and this way further reduces interlayer binding. The TMDC flakes are further peeled off by using ultrasonication[37] or thermal shock[136] and remain stable in the solution itself. These approaches by liquid exfoliation also have some drawbacks such as the appearance of defects, and the intercalation process may itself alter the lattice structure of the TMDCs layers.

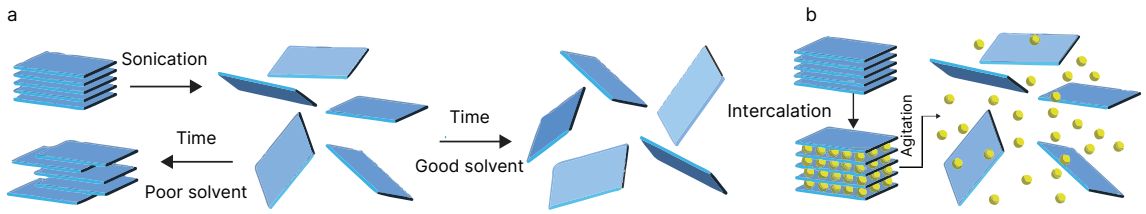

Figure 2.17: Schematic description of the liquid exfoliation mechanism. (a) Sonication assisted exfoliation (b) Ion intercalation. Reproduced from Nicolsi *et al.*[112]

2.2.2 Bottom-up technique

Bottom-up techniques include chemical vapour deposition (CVD), thermolysis, physical vapor transport or van der Waals epitaxy. These methods have recently showed promise to generate high quality TMDCs layers with scalable size, controllable thickness and excellent electronic properties. Multiple TMDC compounds have been grown using this method such as MoS_2[25;92;166], $MoSe_2$[78], $MoTe_2$[174], WS_2[30], WSe_2[63] .

One can classify bottom-up techniques into two types: a single-step and two-steps processes. In single-step process, gases comprising the metal and chalcogen atom are simultaneously introduced and react on a particular substrate, while in the 2-step process, the metal atoms are usually deposited on the substrate and TMDC growth is triggered by the chalcogenization process.

Synthesis via transition metal (or transition metal oxide) chalcogenisation

The TMDC layers can be synthesized by chalcogenisation of the transition metal oxide (or MO_x) at relatively high temperatures. This is the 2-step process and the method can be understood as follows: the transition metal (or MO_x oxide) is evaporated on top of a substrate (e.g. using an e-beam evaporator), the chalcogen atoms are then introduced and the sample is then annealed at high temperature. The reaction mechanism can be understood as a chemical reaction. Zhan *et al.*[166] pioneered the 2-step synthesis of MoS_2. This method when using Mo as a precursor is limited by the domain size and the thickness uniformity of the TMDC layers. Because Mo in bulk is a high migration temperature metal, a large density of Mo and MoS_2 domains might form at "reasonable" growth temperatures. As it turns out, the nature of the precursors plays an important role in the morphology of the TMDC layers. The metallic oxides happen to migrate more easily than metal atoms, so the nucleation density is lower and larger domains are obtained. Li *et al.*[92] synthesized large MoS_2 thin layers even at wafer-scale by using MoO_3 as a starting material. Other oxides were also used[25;153].

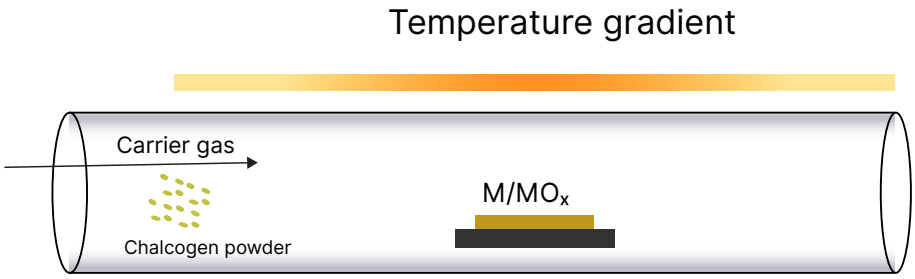

Figure 2.18: Schematic of a common method used to deposit TMDC from vapour phase. Metal/Metal oxide are deposited on a substrate and chalcogen supplied as gaseous precursors.

To synthesize tellurides, another challenge is faced when using high growth temperatures: MoTe2, for instance, decomposes by losing Te as a vapor. A second feature that makes $MoTe_2$ different from other TMDCs is that the energy difference between the 2H and the 1T' phases is rather small, making it very difficult to control the synthesis of the desired phase. However, in a paper in 2015, Zhou[174] report on a relation between the $MoTe_2$ phase and the choice of Mo precursor used in the growth. As it turns out when the authors used MoO_3 the process tended to form $MoTe_2$ in the 2H phase while with MoO_2 the 1T' phase preferentially formed.

Synthesis via thermal decomposition of thiosalts

In search of large-area, high quality TMDC layers with good electrical performance, the decomposition of precursors containing Mo and S atoms was explored. It is now well understood that the thermolysis of ammonium thiomolybdates $[(NH_4)MoS_4]$ in an N_2 environment results in the conversion to MoS_3 at 120-360°C and further conversion to MoS_2 by

annealing at higher temperature (800°C). The relevant chemical reactions are shown in Eq. 2.6, 2.7.[19] One can also suggest that the conversion can be done from $(NH_4)MoS_4$ directly to MoS_2 in the presence of H_2 gas. This reaction, shown in Eq. 2.8, occurs at a moderate temperature of around 425°C.[19]

$$(NH_4)_2MoS_4 \rightarrow 2NH_3 + H_2S + MoS_3 \tag{2.6}$$

$$MoS_3 \rightarrow MoS_2 + S \tag{2.7}$$

$$(NH_4)_2MoS_4 + H_2 \rightarrow 2NH_3 + 2H_2S + MoS_2 \tag{2.8}$$

Liu *et al.* used a two-step process to produce large-crystalline MoS_2 thin sheets on a variety of insulating substrates.[98] The field-effect transistors (FETs) devices made of the MoS_2 sheets exhibit high on/off current ratio and carrier mobility values.

Synthesis via vapor pressure reaction of transition metal (oxide) and chalcogen precursors

In this type of bottom-up technique also called direct reaction, or one-step process, gaseous species of transition metal (or transition metal oxide) and chalcogenides are introduced simultaneously. One such study by Lee *et al.* allowed growing large-area of MoS_2 using S and MoO_3 powders on SiO_2/Si substrate.[89] This method allows growing single-crystalline MoS_2 flakes directly on arbitrary substrates, however, the substrate treatment prior to the growth must be considered with care. The substrate treatment using aromatic molecules such as graphene oxide (r-GO), perylene-3,4,9,10-tetracarboxylic acid tetrapotassium salt (PTAS) and perylene-3,4,9,10-tetracarboxylic dianhydride (PTCDA), promotes the layer growth of MoS_2.[93] These graphene-like molecules act as nucleation for this one-step CVD.

Others may argue that the nucleation of the growth can occur at the edges or defects of the substrate. This allowed producing triangular-shaped MoS_2 layers with the typical domain size much larger than 1μm. Larger domains, of 120 μm (MoS_2) and 180 μm (WS_2) were also obtained.[30]

Another condition that affects the morphology of TMDC growth is the nature of the precursors. Ganorkar[46] studied CVD growth of MoS_2 with two precursors, MoO_3 and $MoCl_5$ and found that while the MoO_3 precursor results in a triangular-shaped MoS_2, the $MoCl_5$ results in a uniform MoS_2 but without the triangles. Besides the favorite SiO_2 substrate, TMDC SL can also be synthesized not only on other insulating substrates (Si wafer or sapphire) but also on graphite.[167]

Besides growth on a weakly interacting substrate, growth on a more strongly coupling substrate (Such as Au(111)[139], Ni(111)[10], Ag(111),[105] etc) has been studied recently using vdW epitaxy. In an example, the Mo atoms are evaporated under an ultra-high vacuum to

a substrate in H_2S environment. This method can produce very high-quality MoS_2 SL with a low density of defects.[10] The outcome is further discussed in *Chapter* 5.

2.3 Conclusion

Single layer TMDCs are remarkable systems, for instance in the form of a semiconductor with a great potential for applications. Using DFT calculations we can not only understand the structural properties, but also the electronic properties. But some key questions remain open. First, one may wonder how the materials' properties are affected by different type of defects. Second, will it be possible to create a heterojunction of two different TMDCs with a similar lattice constant? And third, can we decouple the TMDC single-layer from a growth substrate with which they strongly interact? With all the techniques (simulation and experiment) introduced in the last two chapters, finding the answer to those questions is the main purpose in the three next chapters.

Chapter 3

Point Defects in Single Layer TMDs

3.1 Introduction

Defects in a crystal are unavoidable according to the second law of thermodynamics, and in practice due to the simple fact that the materials never are elementary 100% pure. Furthermore, defects can also be formed during growth, post-processing, patterning, etc. Since they change the properties of a system and especially can alter devices' efficiency, it is of the highest importance to determine their nature and their origin so that one could be able to cure them or at least minimize their effect. This is especially true for 2D materials where low dimensionality reinforces the effect of defects. For instance, vacancies introduce states in the bandgap of semiconducting 2D materials, shift the Fermi level and then change the electronic properties. Substitution of atoms may appear in the fabrication method and it also modifies the electronic structure (significantly or not, in case of Se/S substitution), and so on. Defect at the atomic scale can also have a considerable effect on magnetic, and optical properties.

But defects can also be made on purpose to tune desired electronic, optical or magnetic properties. It is the case in electronics devices such as junctions or transistors where dopants are nothing else than defects that are well characterized and incorporated in the system in a controlled way. In this chapter, we deal with point defects — that is geometrical defects that affect isolated atomic sites of the crystal. One usually classifies these defects in two different kinds, intrinsic ones such as vacancies, antisites, interstitial and extrinsic defects such as substitutional defects and dopants.

The chapter builds on a paper published in ACS Nano.[35] I have optimized the geometry and calculated the electronic structure of many defects in MoS_2 and calculated partial charge map that are compared to STM experiments to determine the nature of a defect that was observed with a high precision in a new source of MoS_2 (prepared at high temperature and

pressure — HP/HT) in the experimental teams of Néel Institute.

3.1.1 Intrinsic point defects in single layer TMDCs

Point defects can have different forms: vacancies such as single vacancy of chalcogen or metal atoms, a complex vacancy that can be a combination of chalcogen and/or metal atoms, the substitution of the transition metal atom by another element, interstitial but also adatoms on one side or both sides of the layer. Because they alter transport properties and device characteristics[64], they have been extensively studied especially the most common one for MoS_2, the S vacancy.[53;71;75;76;94;125;175] The point defects can be introduced during the fabrication process often occurring at relatively high-temperature[60], but also during monolayer transfer. They can also be related to the substrate. Some groups even create point defects like vacancies by electron irradiation to study them.[144;147]

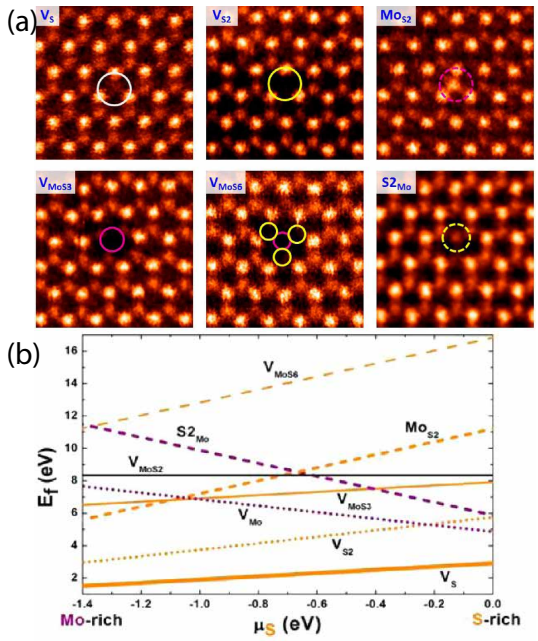

Figure 3.1: Point defects in MoS2. (a) atomic resolution STEM images, (b) formation energy of different point defects as a function of sulfur chemical potential. Reproduced from Zhou *et al.*[175]

The single S vacancy is a defect commonly observed in MoS_2 samples.[75;125;175] Their presence has been related to intrinsic n doping in MoS_2[101] or not[76]. From calculations[49;53] they have the lowest formation energy. Figure 3.1 from[175] shows the formation energy of different point defects in MoS_2 as a function of the sulfur chemical potential and their STEM images. The calculated defects are described in figure 3.2 and correspond to sulfur single vacancy, sulfur divacancy with two possible configurations (two vacancies within the same atomic plane or one in each of the atomic planes sandwiching the Mo plane), substitutional

of S or Mo atoms by an extrinsic atom and Mo single vacancy. The defect formation energy is calculated using:

$$E^f = E^{def}_{Tot} - E^{host}_{Tot} \pm \sum_i n_i \mu_i, \tag{3.1}$$

where E^f is the defect formation energy, E^{def}_{Tot} and E^{host}_{Tot} are the total energy taken from DFT calculations with and without the defect, respectively, n_i and μ_i are the number and the chemical potential of the removed/added atoms.

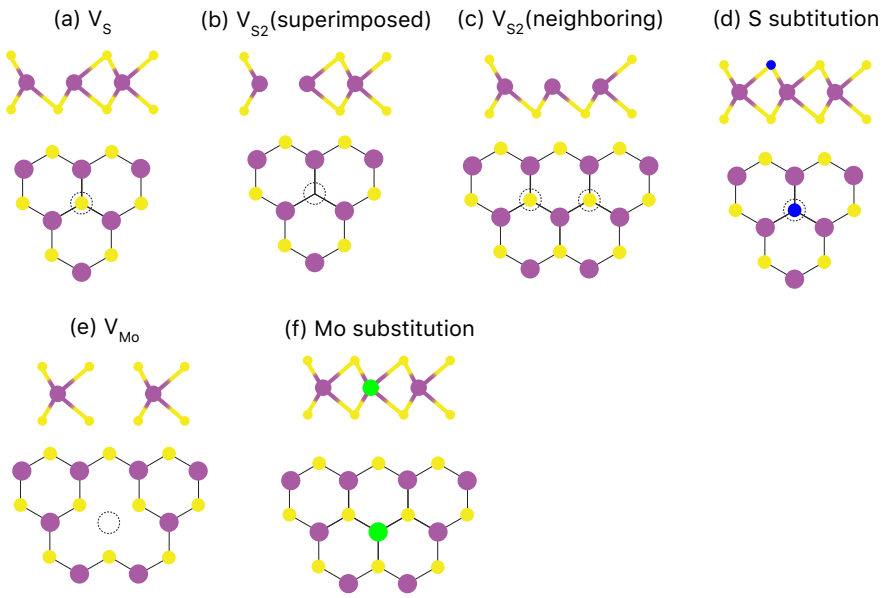

Figure 3.2: Geometry of different types of point defects within a TMDC single-layer: vacancies (a)-(c), (d) subtitutional at position of S atom, (e) Mo-vacancy and (f) subtitutional at position of Mo atom.

Eventually, another type of intrinsic defect — outside the layer — is an adatom.[71;114;175] This adatom can occupy different inequivalent high symmetry positions such as the center of the hexagon, on top of the chalcogen or metal atom, bridge sites. Mo and S adatoms are often observed on top of CVD - MoS_2[175]. Noh *et al.*[114] found that the only stable configuration for the S adatom on MoS_2 SL is on top of the S atom site whereas the Mo adatom can be found on top of the hexagon center or Mo atom.

It is worth to note that discriminating the point defects at the atomic level is difficult because of their variety due to the different steps involved in material growth. Recent results from Barja[11], for instance, based on multiple measurements with a specific fabrication environment suggested that the common chalcogen defects are substitutional oxygen rather than vacancies, this was also observed by several other groups.[147;170]

3.2 DFT calculations of point defects in MoS_2

We studied different point defects of MoS_2 to optimize their geometry and calculate their electronic structure. These defects include MoS_2 common point defects: S vacancy and di-vacancy, Mo vacancy, Se/S and Cl/S substitution together with impurities that are detected in MoS_2 samples used in Néel Institute: Fe/Mo, C/S, N/S, B/S substitutions.

3.2.1 Calculation details

Calculations are performed using a supercell technique, which has been explained in Chapter 1. A plane-wave cut-off of 500 eV and a Monkhorst-Pack mesh of 1×1 × 1 (for the atomic relaxation) and 6×6× 1 (for the density of states calculations) for Brillouin zone integration are employed. The total energies are converged if the change in total energy between two ionic steps is smaller than 10 meV. In order to eliminate the interaction between two adjacent layer images, a vacuum layer of 15Å is added in the z direction. A 6×6×1 super-cell in lateral dimensions is constructed to introduce the point defects. The supercell is shown in Fig. 3.3 (a). For STM simulations, a constant-height cut of the partial charge is calculated on both sides, as depicted in Fig. 3.3(c), from now onward, the constant-height cuts on the left (same side than the defect) is called the *defect-side* and on the right is called the *other-side*.

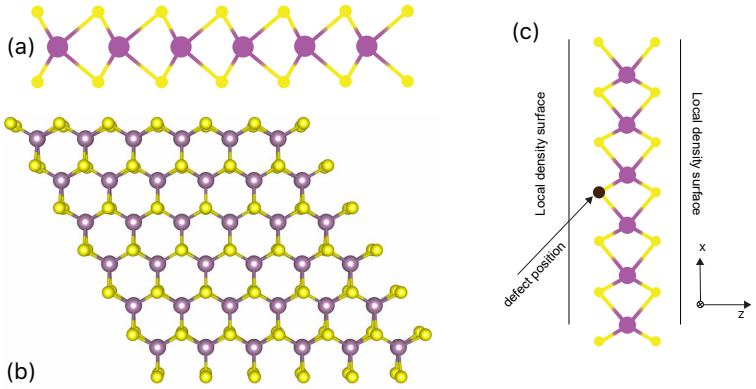

Figure 3.3: Supercell used for the calculation in (a) side and (b) top view. (c) The local density surface for simulating the STM images regarding both sides of the defect positions. The large (purple) and small (yellow) balls indicate Mo and S atom, respectively.

3.2.2 S vacancy

Figure 3.4 shows our DOS and partial charge maps (STM images) on both sides of the MoS_2 plane of a S vacancy (V_S) in a MoS_2 SL. As one S atom is removed from the superstructure, three nearest neighbor Mo atoms are found to be shifted away from the vacancy by 0.1 Å in the Mo-plane, the S atom bellow is shifted downward by only 0.03Å. The vacancy induced

two states in or close to the gap. The first one is filled, on top of the valence band (-0.15 eV), the second one is empty (+1.1 eV) and strictly localized on the vacancy.

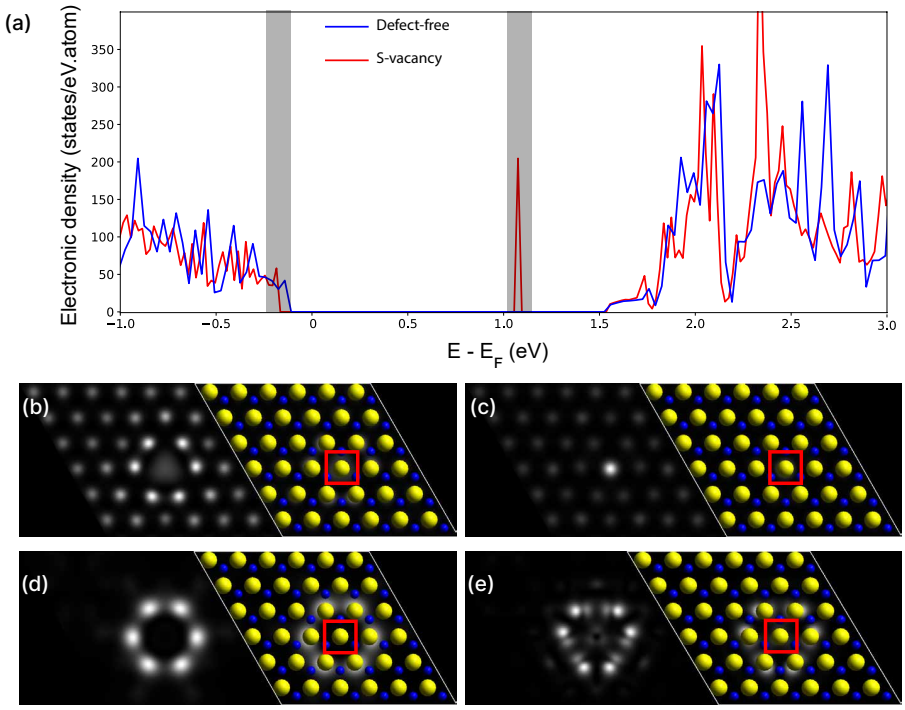

Figure 3.4: S vacancy in MoS_2 (a) DOS (b-e) partial charge maps on both sides of the MoS_2 plane and integrated on the shaded areas. (b) and (c) (resp. (d) and (e)) correspond to filled states (resp. empty states). (b) and (d) are on the vacancy side and (c) and (e) on the opposite side. Blue(Yellow) balls correspond to Mo(S) atoms, respectively, the red square indicates the defect position.

3.2.3 S divacancy

In addition to a single S vacancy, we also characterize the possibility of a double vacancy in MoS_2 SL. Two configurations were considered, in the first one, the two missing S atoms are first neighbors (then in the same plane) while in the second case they are superimposed on both sides of the Mo layer. The superimposed configuration is preferred by 40 meV using formula 3.1. Furthermore, our calculations in agreement with others show that S divacancy is less favorable than S monovacancies.

Figure 3.5 shows the DOS and the simulated STM images of the MoS_2 SL with an S-divacancy where the two removed S atoms are in the same surface. While atomic displacements are similar to what was observed in the mono vacancy case, the constant height cuts show complex patterns due to the rehybridization of orbitals. This type of defect obviously breaks the 3-fold symmetry of the lattice and creates two sets of two peaks, one on top of

the valence band and the other one deep inside the gap so at positions similar to what was found for the single vacancy. Here again, states in the gap are localized on the vacancies.

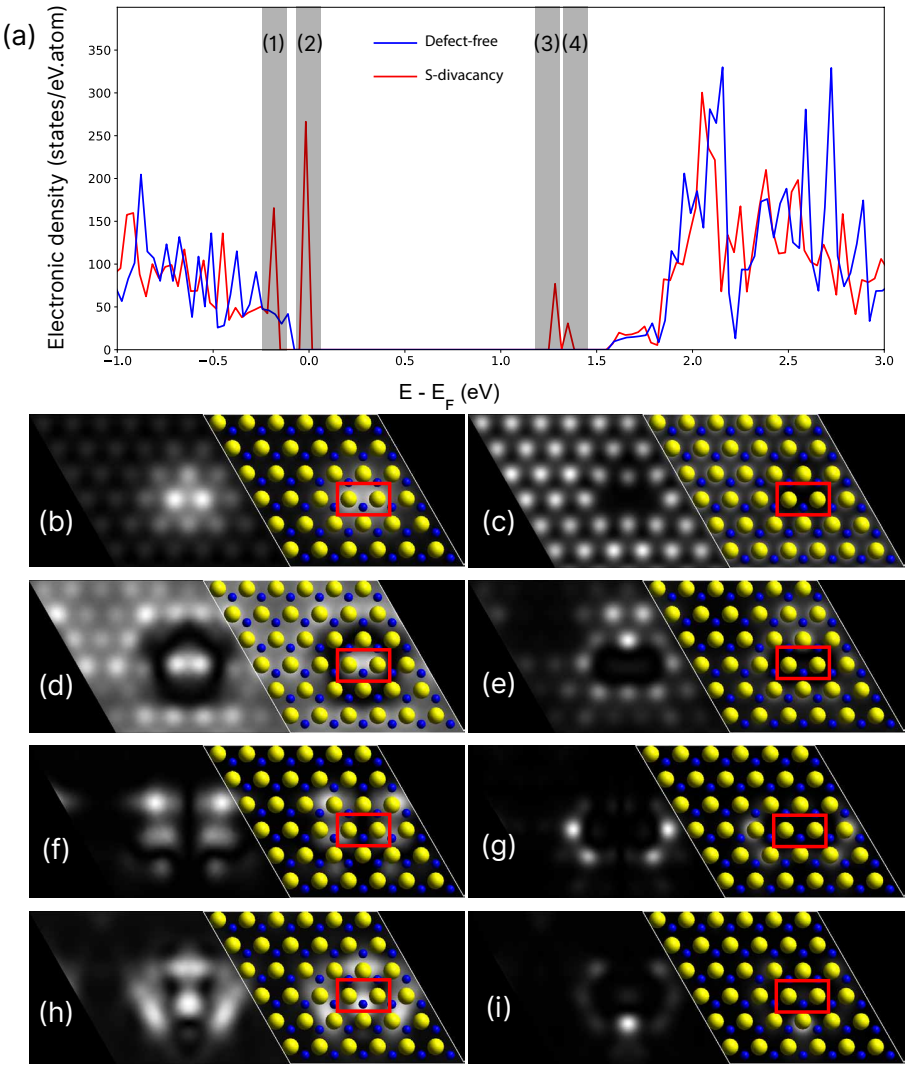

Figure 3.5: S divacancy in MoS_2 where the two missing S atoms are on the same plane. (a) DOS, (b-i) partial charge maps on both sides of MoS_2 plane and integrated on the shaded areas marked (1), (2), (3), (4) in (a). The DOS of pristine MoS_2 has been shifted to match the CBM of the defect DOS. Left (right) column of the partial charge maps correspond to the *defect* (*other*) sides.

The second possibility of V_{S2} is that the two removed S atom are superimposed located in two different atomic planes, the DOS and the simulated STM images of this structure are shown in Fig. 3.6. The removal of 2 S atoms creates 6 dangling bonds for the super-lattice system and modifies the top of the valence band significantly. To characterize the filled states at the top of the valence bands, the partial charges integrated with the range of -0.2 to 0.2 eV are shown in Fig 3.6 (b-c). Another resonance at 1.15 eV is unfilled and strictly localized on the vacancy. Obviously, due to the mirror symmetry in the z direction, the partial charge maps on both sides of the MoS_2 plane are identical. The partial charge maps

are very similar to the one obtained for the mono-vacancy.

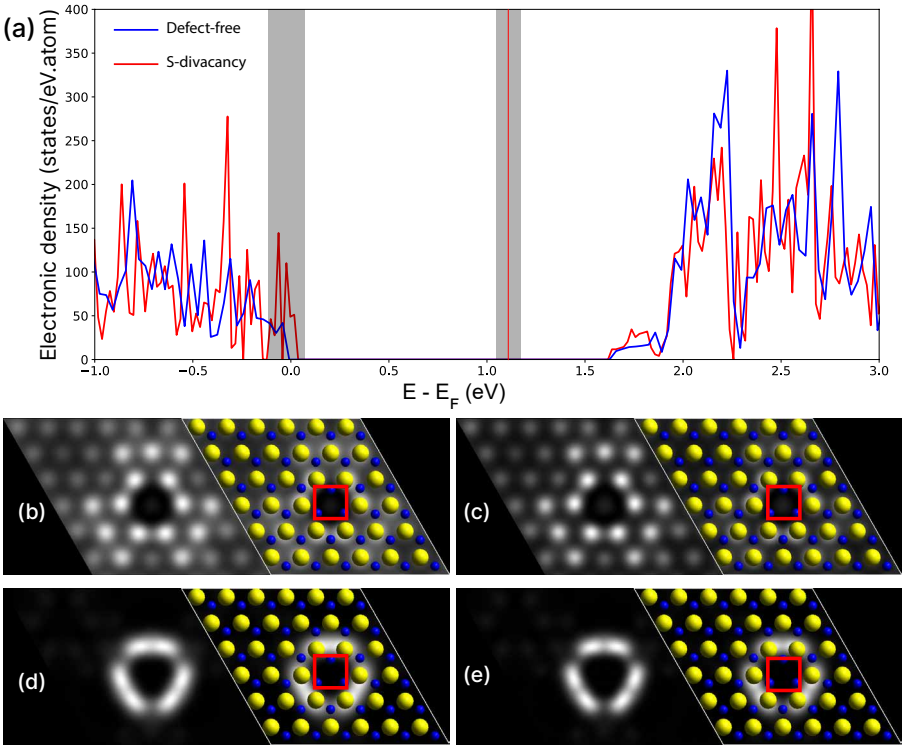

Figure 3.6: S divacancy in MoS_2 where two removed S atoms are superimposed. (a) DOS, (b-e) partial charged maps on both sides of the MoS_2 plane and integrated on the shaded areas. (b) and (c) (resp. (d) and (e)) correspond to filled states (resp. empty states). The DOS of pristine MoS_2 has been shifted to match the CBM of the defect DOS. Partial charge density cuts are identical on both sides.

3.2.4 Se/S substitution

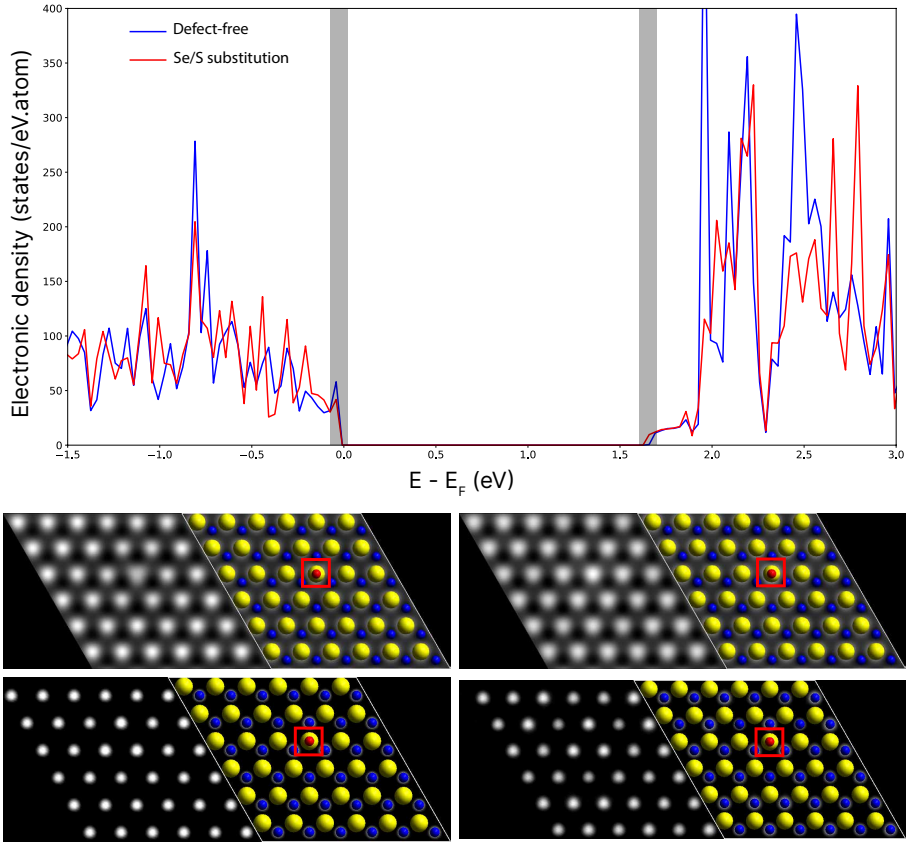

Figure 3.7: DOS of MoS_2 SL where a S atom is replaced by a Se atom. (a) DOS, (b-e) partial charged maps on both sides of the MoS_2 plane and integrated on the shaded areas. (b) and (c) (resp. (d) and (e)) are the partial charge at the vicinity of the valence band (resp. conduction band). Partial charge density cuts are identical on both sides.

Here, we analyze the case where an S atom is replaced by a Se atom. The reason behind these calculations is that MS_2/MSe_2 heterostructure has been investigated recently by several groups.[12] Since the growth usually needs multiple evaporation steps at high temperatures, different types of defects might appear, and one of them is the diffusion of S/Se at the interface of the junction. Since S and Se atoms are in the chalcogen family, they all have 4 electrons at the outer shell, the contribution of Se/S substitution in the super-lattice should have no significant effect. This is indeed what we find, the DOS in Fig. 3.7 (a) shows that the bandgap of the defect structure is reduced by only 30 meV and no feature appears in it.

3.2.5 B/S substitution

In the next parts, we investigate the possibility of p-type doping replacing an S atom with B, C, N.[101] Figure 3.8 shows the DOS and the partial charge of MoS_2 SL where an S atom is replaced by a B atom. The lattice symmetry remains, the substitutional B atom is moved 0.7 Å towards the Mo-plane with respect to the original S atom. A single defect state is found in the DOS spectrum in Fig. 3.8(a) close to the valence band that fixes the Fermi level. Partial charge maps show that this defect like the other ones affects both sides of the SL.

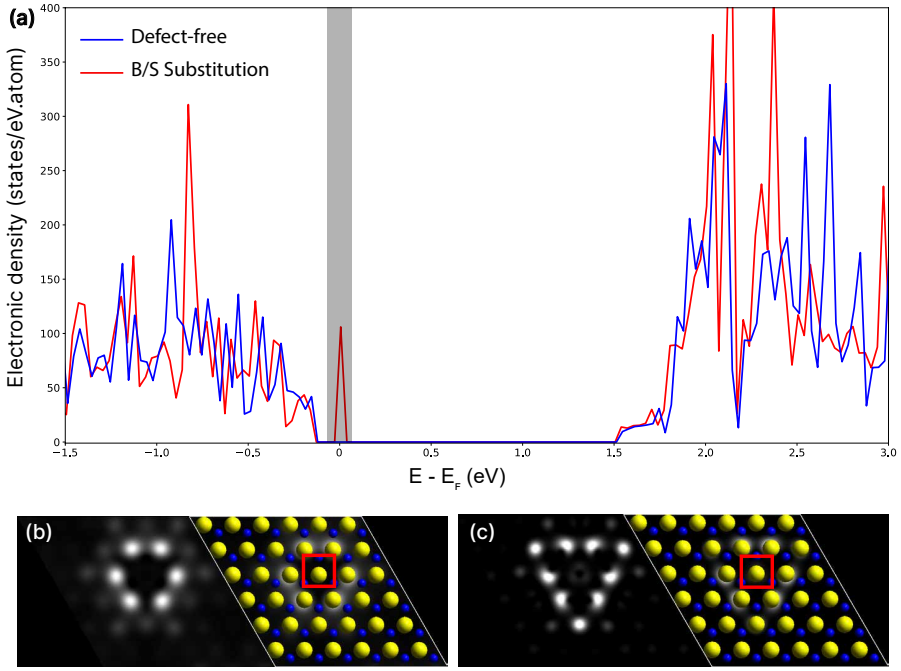

Figure 3.8: B substituting S in MoS_2 SL. (a) DOS, (b-c) partial charge maps (STM images) on both sides of the MoS_2 plane and integrated on the shaded areas. The DOS of pristine MoS_2 has been shifted to match the CBM of the defect DOS. Left (right) column of the partial charge maps corresponds to the *defect* (*other*) side.

3.2.6 C/S substitution

Figure 3.9 shows the DOS and the partial charge density cuts of MoS_2 SL where a S atom is replaced by a C atom. Similar to B_S defect, the substitutional C atom moves 0.75 Å towards the Mo-plane. A single defect state is found in the DOS (Fig. 3.8(a)) at the top of the valence band, in agreement with reference[101].

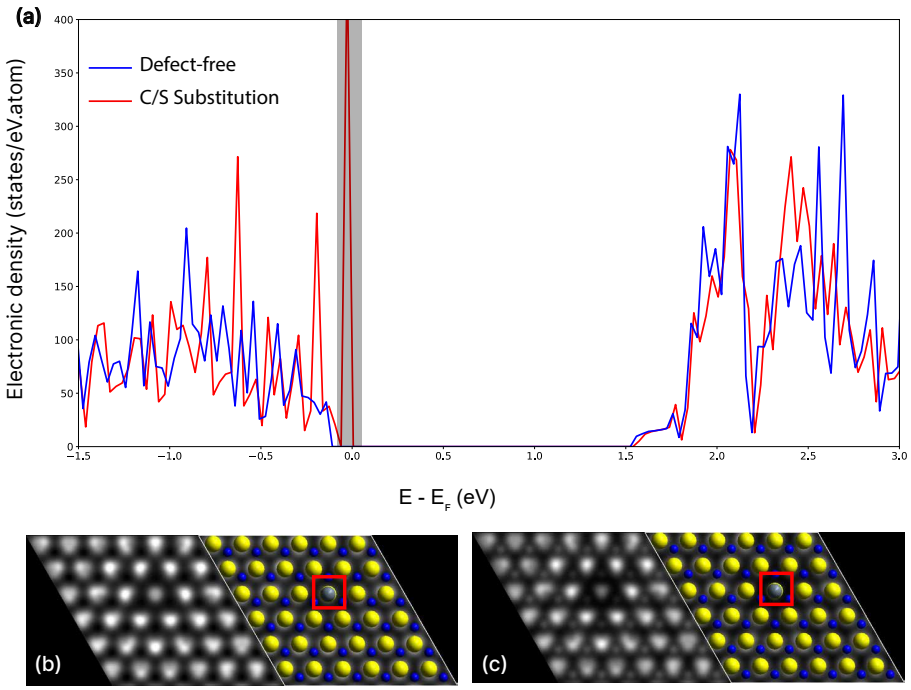

Figure 3.9: C substituting S atom in MoS_2 SL. (a) DOS, (b-c) partial charge maps on both sides of the MoS_2 plane and integrated on the shaded areas. The DOS of pristine MoS_2 has been shifted to match the CBM of the defect DOS. Left (right) column of the partial charge maps corresponds to the *defect* (*other*) side.

3.2.7 N/S substitution

Another candidate to induce p-type-doping in MoS_2 is an N atom substituting an S atom. The results are shown in Fig. 3.10. With no change in lattice symmetry like other point defects, the N atom position is moved 0.7 Å towards the Mo-plane with respect to the S atom. A sharp peak appears at the Fermi level and studying spin polarization of this state could be interesting[114]. The STM features of the defect look similar on both sides, consisting of a ring with three pairs of radial legs.

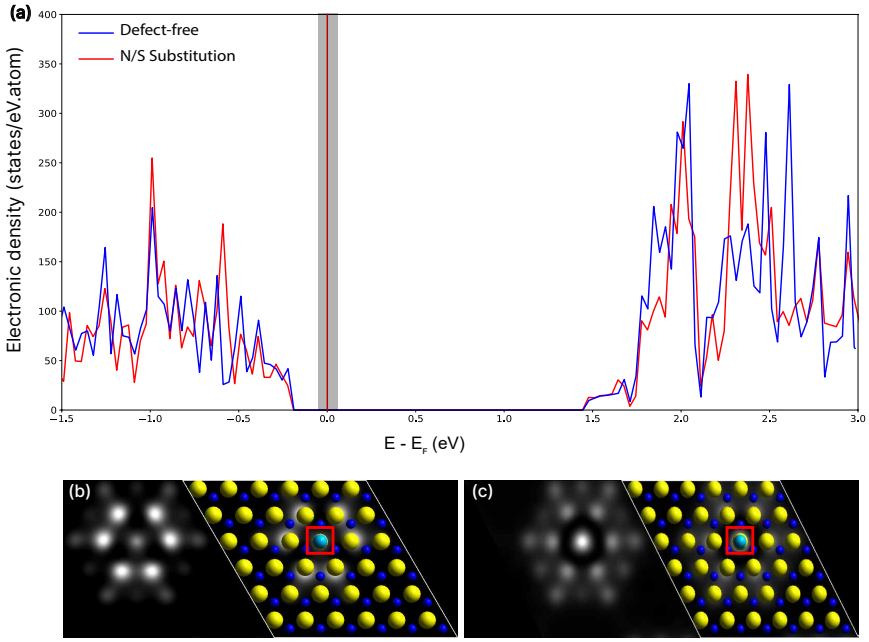

Figure 3.10: N substituting S atom in MoS_2 SL. (a) DOS, (b-c) partial charge maps on both sides of the MoS_2 plane and integrated on the shaded areas. The DOS of pristine MoS_2 has been shifted to match the CBM of the defect DOS. Left (right) column of the partial charge maps corresponds to the *defect* (*other*) side.

3.2.8 Cl/S substitution

To evaluate now n-type doping possibilities, we simulate MoS_2 SL where an S atom is substituted by a chlorine (Cl) atom, Cl_S. The Cl_S system is excepted to act as a source of n-type doping for MoS_2 because Cl has one more electron than S. The DOS is shown in Fig. 3.11(a), a state is found in the gap about 0.2 eV below the CBM, similar to what Dolui *et al.* have found[34]. No great change in lattice structure was observed, the substituted Cl atoms remain almost at the exact position of the replaced S atom. The simulated STM images show bright spots on the neighboring S atoms, depression is found around the defect at about 2 lattice constants.

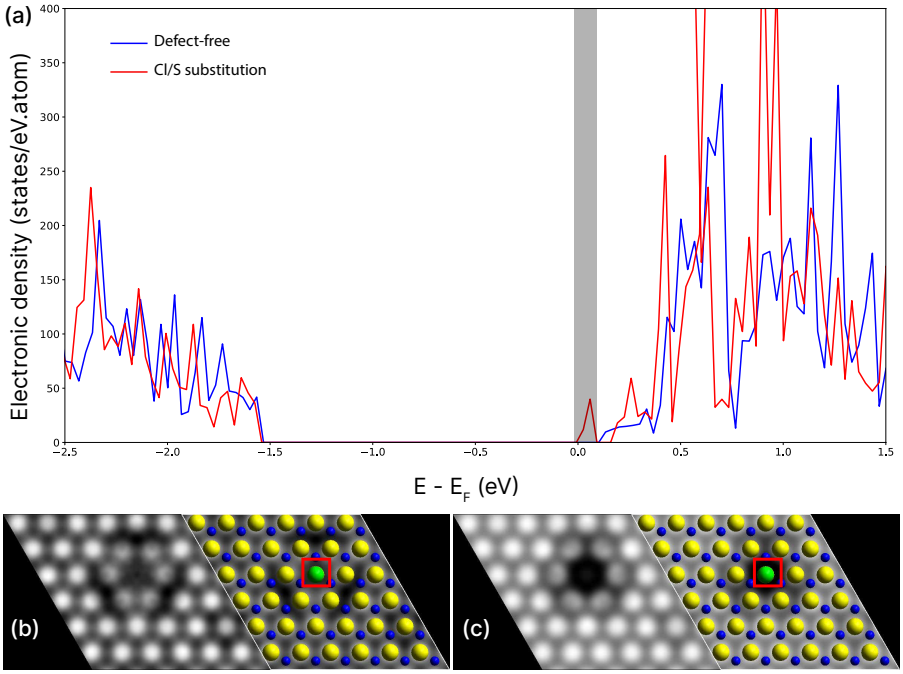

Figure 3.11: Cl substituting a S atom in MoS_2 SL. (a) DOS, (b-c) partial charge maps on both sides of the MoS_2 plane and integrated on the shaded area. The DOS of pristine MoS_2 has been shifted to match the CBM of the defect DOS. Left (right) column of the partial charge maps corresponds to the *defect* (*other*) side.

3.2.9 Mo vacancy

The atomic structure of a V_{Mo} is shown in Fig. 3.2(e). The DOS and simulated STM images are shown in Fig. 3.12. Like for the S (di)vacancy, the geometry of the Mo vacancy does not induce a significant distortion of the lattice. The atoms surrounding the vacancy are slightly moved toward the defect position. As a result of the defect formation, a Mo atom and six Mo-S bonds are eliminated, consequently, six S dangling bonds remain in the V_{Mo} structure. As shown in Fig. 3.12 (a), four peaks are found in the gap or close to it.

In agreement with Noh[114], the first two states are filled and the other two are empty. The partial charge maps integrated in region (1)-(4) are given in Fig. 3.12 (b-i). Images on both sides are identical because of the symmetry of the defect.

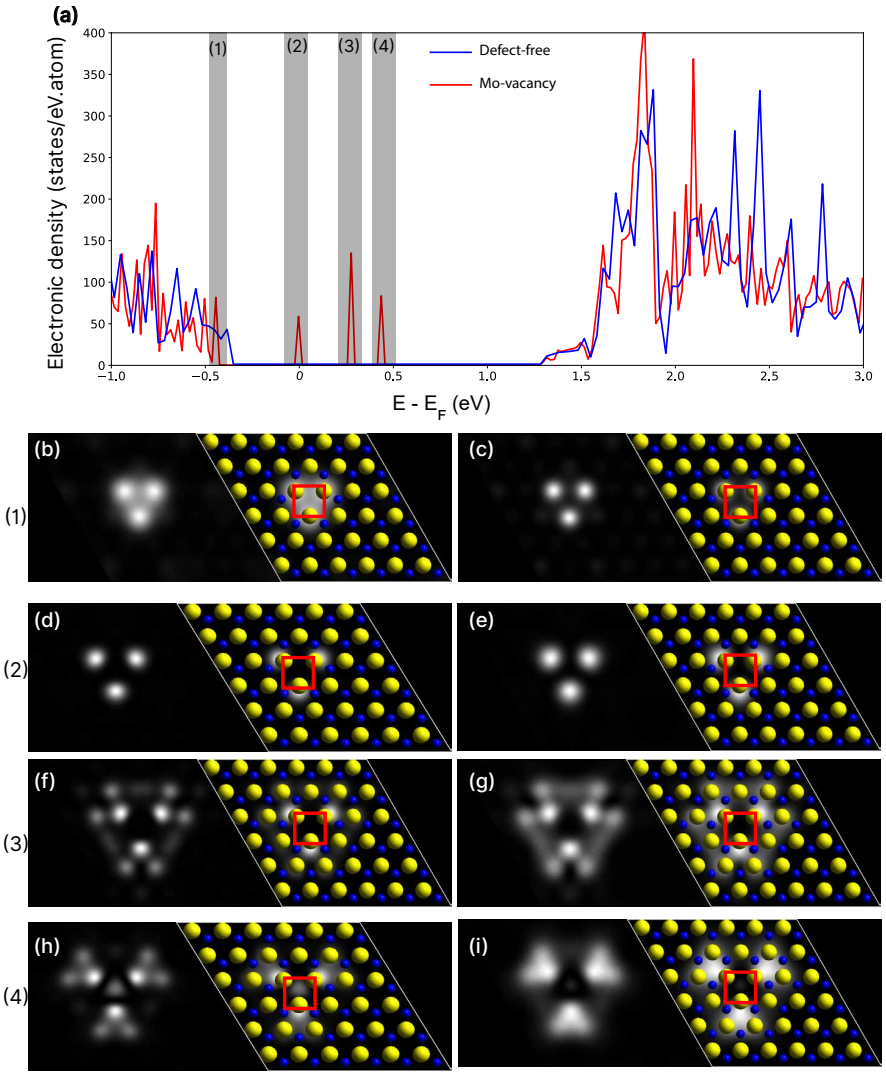

Figure 3.12: (a) Density of states of Mo vacancy V_{Mo} in MoS_2 SL. (b-c), (d-e), (f-g), (h-i) corresponds to partial charge maps at peak positions (1), (2), (3), (4) in (a), respectively. DOS of pristine MoS_2 has been shifted to match the CBM of the defect DOS. Left (right) column of the partial corresponds to the same defect side (opposite).

3.2.10 Fe/Mo substitution

Next, we consider the substitution of Mo by Fe. When Fe replaces Mo, two extra electrons are added to the supercell. It creates a peak located well above the CBM at 0.7 eV. The substitutional defect also creates a defect state inside the bandgap (Fig. 3.13(a)). The simulated STM images are identical from both sides because of the symmetry of the system.

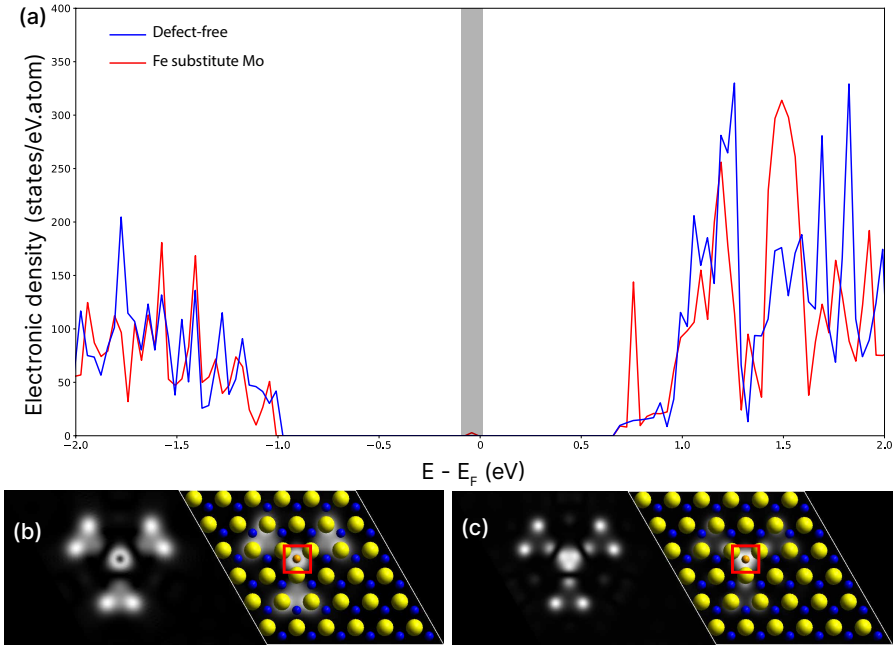

Figure 3.13: Fe substituting Mo in MoS_2 SL. (a) DOS, (b-c) partial charge maps on both sides of the MoS_2 plane and integrated on the shaded areas. The DOS of pristine MoS_2 has been shifted to match the CBM of the defect DOS. Left (right) column of the partial charge maps correspond to the *defect* (*other*) side.

3.3 Weakly Trapped, Charged, and Free excitons in Single-Layer MoS_2 in the Presence of Defects, Strain, and Charged Impurities

Defects in different MoS_2 samples by mechanical exfoliation of two kinds of bulk MoS2 (a natural source, and a source prepared at high temperature and pressure — HP/HT) on different substrates were studied by Raman, PL, and STM in Néel Institute. They found the defect-bound state in HP/HT MoS_2 having low binding energy of 20 meV that does not appear sensitive to strain and doping, unlike charged excitons. The nature of this defect has been solved by coupling the STM experiment results from P. Mallet - J. Y. Veuillen and co-workers to our DFT calculations.[35]

STM images of HP/HT MoS_2 with 5 layers show two prominent populations of point defects, which appear as a bright feature and a depression, respectively (Figure 3.14). Depression-like defects of the same extension (1—2 nm) or slightly larger (in the few nanometer scales) have been reported previously.[49;101;125;147] Among them, one appears as a depression at negative tip-sample bias as in our observations and is a characteristic defect in natural MoS_2 that is ascribed to missing S-Mo-S fragments located either in the top or in a buried MoS_2 layer.[3] The second kind of defect (the bright one – green arrow) has not been observed

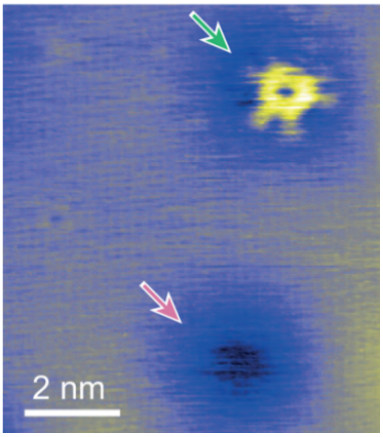

Figure 3.14: STM topography (V_b = -2V, I_t = 0.2 nA) close-up view on some defects. The green and pink arrows point to two kinds of defects (measurements by P. Mallet, J.-Y. Veuillen and co-workers).

in natural MoS_2 samples and is hence generated during the preparation of the HP/HT sample. It has a characteristic shape resolved with sharp STM tips, consisting of a ring with three pairs of radial legs. The size of the ring is typically 0.7 nm. Defects featuring a ring shape in STM have also been reported previously[1] and were ascribed to alkali atoms adsorbed on the surface. Neither the HP/HT process nor the ultra-high-vacuum chamber where the STM measurements were performed seems to yield such adsorbates.

Impurities that are detected in the chemical analysis of raw MoS_2 or present in the h-BN capsule used in the HP/HT process were described in the previous part. The Summary of the partial charge maps that we calculated is given in Fig 3.15 for comparison with STM images. This includes a sulfur vacancy, a molybdenum atom substituted by an iron atom, a sulfur atom substituted by a carbon, a nitrogen, and a boron atom. Each of these defects are associated with electronic states inside the bandgap of MoS_2 or close to the bandgap edges (3.15).[34;101;144] The spatial resolution is higher in partial charge maps than in STM presumably due to the shape of the tip, and more realistic simulation of the actual experimental situation would require taking into account the electronic properties of the tip, which we do not do here. Nevertheless, the main features of the defect pointed by the green arrow compare very well to the N substitutional defect: the sizes of the lower-intensity central feature match and the three pairs of legs appearing in the experimental image seem reminiscent of the three lobes found in the simulations. The new defect observed in HP/HT MoS_2 was then ascribed to an N substitutional defect.

Photoluminescence measurements performed in Néel Institute on the same samples unveil various optically active excitonic complexes and especially a defect-bound state having low binding energy of 20 meV that we related to the N/S defect.

To summarize our results for point defects in MoS_2 SL, we found that in most cases, point

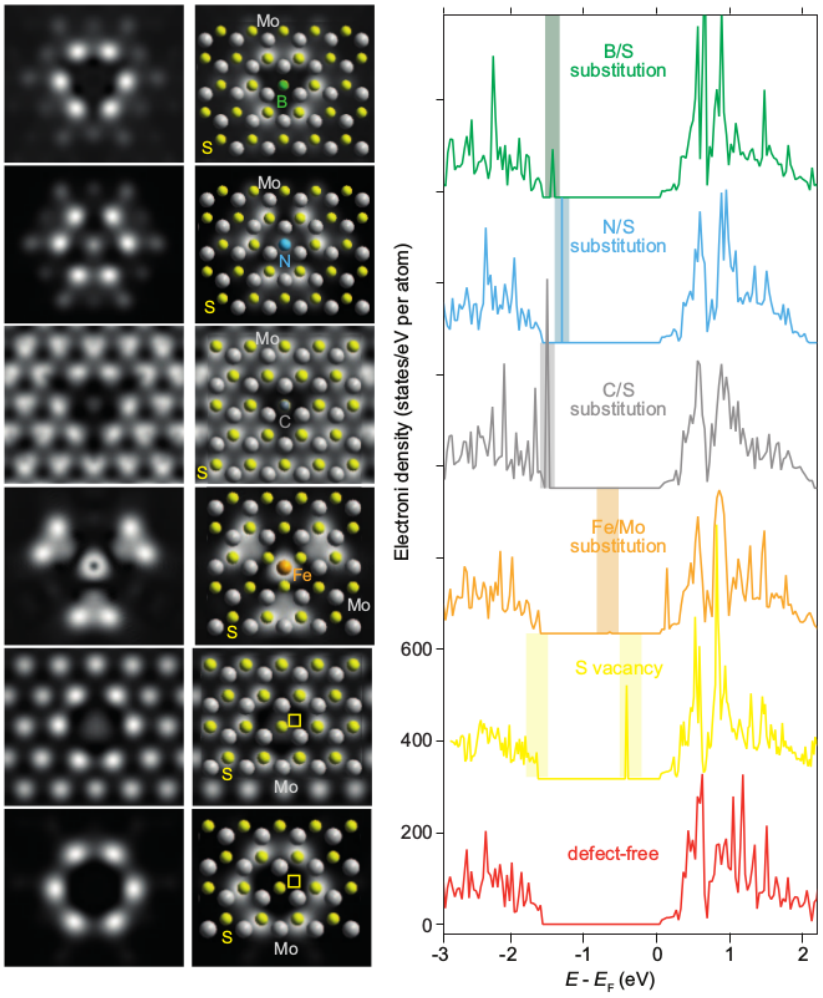

Figure 3.15: Electronic density of states and constant-height cuts (1 Å) of the partial charge around B/S, N/S, C/S substituted atoms , the Mo/Fe and the sulfur vacancy integrated in the energy range shaded in the electronic density of states spectra (the fifth and sixth rows correspond to the two lower- and higher-energy yellow-shaded ranges respectively). The electronic density of states for defect-free MoS_2 is shown as a reference. All spectra have been shifted horizontally to match the minima of the conduction band (at zero energy) and vertically for clarity.

defects do not significantly alter the lattice structure and that the created defect states are localized close to the defect. Coupling DFT calculations and STM imaging allowed us to discriminate between many possibilities to unveil the nature of the observed defect.

Chapter 4

$MoSe_2/WSe_2$ in-plane junction - the zigzag case

4.1 Introduction

In case of 3D materials, when two doped semiconductors (e.g. two TMDCs) are brought together to form a $p-n$ junction at thermal equilibrium, electrons (holes) from the n(p) part diffuse to the p(n) part where they recombine, leaving the charged ions (ionized dopants) uncompensated. Due to the limited density of free carriers in a semiconductor, recombination occurs within a region of finite width which becomes insulating but charged and is called depletion layer. This region is associated with an extended interface dipole. The corresponding electric field induces a bending of valence and conduction bands of each constituent. In a junction between intrinsic semiconductors, the bands may align with respect to the vacuum level.

This band alignment description assumes that no interfacial or defect state exists within the gaps. If it is not the case (the most common case) then these defect will pin the Fermi level and play a major role in the junction operation.[103]

In the case of 2D systems, the picture developed for 3D systems must be revised. In a stack between two 2D materials, the concept of a depletion region breaks down, since a meaningful thickness cannot be defined for SL 2D materials. In lateral junctions between 2D materials, like the ones considered here, depletion regions are expected, yet their modification upon applied bias may not resemble the situation in 3D systems, due to the reduced dimensionality[2]. Furthermore, defects in 2D materials give rise to specific electronic effects, and their occurrence at the lateral interface between 2D materials (a 1D interface) may accordingly lead to specific Fermi level pinning unlike in 2D interfaces (between 3D materials).

Answering these questions requires the understanding of the 2D interface physics at the atomic scale, an issue which is poorly known up to now. Indeed, to our knowledge, only a few studies at this scale have been published. In a first one STM/STS and photoluminescence experiments are coupled on MoS_2 islands on highly oriented pyrolytic graphite HOPG. It demonstrates pinning of the Fermi level by edge state located within the gap and determines the band bending and the width of the depletion layer.[168] In-plane and vertical junctions between two 2D materials can both be prepared by *in-situ* growth[48;62]. In this chapter, we focus on 2D junctions as prototypes of what true 2D electronics could be. TMDCs with the same chalcogen atom have very similar lattice parameters allowing the growth of sharp in-plane junctions.

4.1.1 Methods

Calculations were performed using the VASP code which is based on density functional theory. The electron-ion interaction is described within the PAW approach, and we use a PBE functional. The supercell approach is used to calculate ribbons (20×1) or junctions (20×1 or 20×4 with defects). A large empty space is introduced in the supercell (25 Å) to avoid spurious interaction along the z direction. A grid of 1×5×1 k point is used, after convergence the total energy variation is smaller than 0.01 eV.

4.1.2 From infinite 2D materials to WSe_2 zigzag ribbon

A ribbon can present different edges geometries: zigzag, armchair, mixed character. They can cut one or two bonds per atom, end on transition metal or chalcogen atoms. Here, a WSe_2 ribbon with zigzag edges is modeled, and we use a geometry where the edges only cut one bond (because cutting 2 bonds would have a higher energy cost). A zigzag ribbon will end on W atoms on one side and Se atoms on the other one (Figure 4.1). Relaxation occurs at the edge. It is rather large on the transition metal side where the atoms go inward so that the edge is made of a mixed W-Se line. The DOS show states within the gap deriving from Se orbitals in the lower part of the gap and W orbitals in the higher part. This is coherent with the positions of vacancy states in the gap of $MoSe_2$: a W(Se) edge corresponds to missing Se (W) atoms and then creates states within the gap at positions close to what was found for chalcogen (transition metal) vacancy in *Chapter* 3. The Fermi level falls in one of these states. The edge state on the W side mainly derives from W dangling bonds, which have a larger spacial extension within the ribbon (Fig 4.1(c)) than edge states on the other side, that remain localized on the Se atom edge.

In classical (3D) heterojunction models, these edge states (the equivalent of surface states

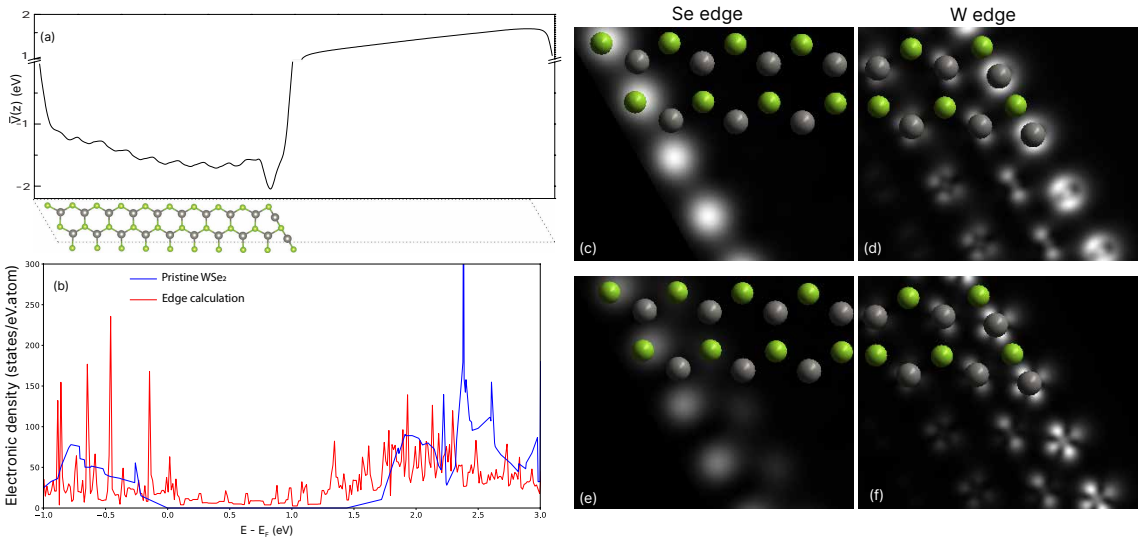

Figure 4.1: (a) Electrostatic profile of 10×2 WSe_2 ribbon, (b) DOS and (c) partial charge maps integrated on the different energy ranges shown in (b), 4 cells are shown along $\mathbf{y}$ to better show the edge relaxation. Partial charge cut on Se side is shown just above the Se layer (on the left) and in the W layer (on the right).

for 3D materials) form a band that could pin the Fermi level: adding or subtracting electrons from the band only has a small effect on the position of the Fermi level because of the band high density of states that can accommodate any variation of charge. A surface dipole is formed. When a junction is formed charge transfer between the surface states bands of the two semiconductors creates a dipole at the interface that aligns the two Fermi levels with an only small variation of the two band structures. Band offset is then determined by the positions of the two surface states in the gap and of the Fermi level within it. Defects in the semiconductors or interface states (due e.g. to the penetration of wavefunctions of one semiconductor in the gap of the other one) that lead to bands within the gaps with a strong density of states can play a similar role and also fix the Fermi level. When no defect or surface or interface bands exist in the gap, bands align with respect to the vacuum level, which is the electronic affinity of each constituent that are bulk properties of the two semiconductors[8]. This last case is really rare.

4.2 $MoSe_2/WSe_2$ heterojunction

The use of a supercell to model a junction means that two junctions are in fact modeled at the same time. The first one (see Figure 4.2(a)) occurs on a Se line where one Se atom is bound to 1 Mo and 2 W and the second one is the reverse case: a Se atom is bound to 2 Mo and 1 W. The last case is not present in this figure, however, results from periodic boundary condition.

TMDCs that share the same chalcogen atom, Se here, have very similar lattice parameters (the lattice constant of $MoSe_2/WSe_2$ are 3.32 / 3.35 Å, respectively, and the distance between the two Se layers are both 3.34 Å). As a consequence, the interface geometry is really simple and the junction appears as a continuation of the lattice (Figure 4.2). If one considers that the junction is created by assembling ribbons, the evolution of the edge states is of interest. Here the DOS of the junction (Figure 4.2(c)) shows no state within the gap: the edge states of the ribbons disappeared which means that the cut dangling bonds recombine so that there is a perfect matching of the wave functions at the interface, and the interface is also ideal at the electronic scale.

No surface/defect states in the gap mean that the bands should align with respect to the vacuum level. The calculated WSe_2 ($MoSe_2$) bandgap is equal to 1.44 eV (resp. 1.25 eV) while its work function are both equal to $\approx$ 2.5 eV. Positioning the bands with respect to the vacuum level led to the prediction of a type II junction for the $MoSe_2/WSe_2$ system[62]. This is what we find: maps of the partial DOS indeed show states on the WSe_2 side only at the top of the valence band and states on the $MoSe_2$ side only, at the bottom of the conduction band. These states leak in the gap inducing evanescent states Fig. 4.2(b) and then a charge transfer (electrons are transferred from WSe_2 to $MoSe_2$) and an interface dipole. According to the potential plotted in Fig. 4.2(a), the offset is equal to 0.2 eV. This is a "simple" DFT calculation so quantitative agreement with experiment is not expected.

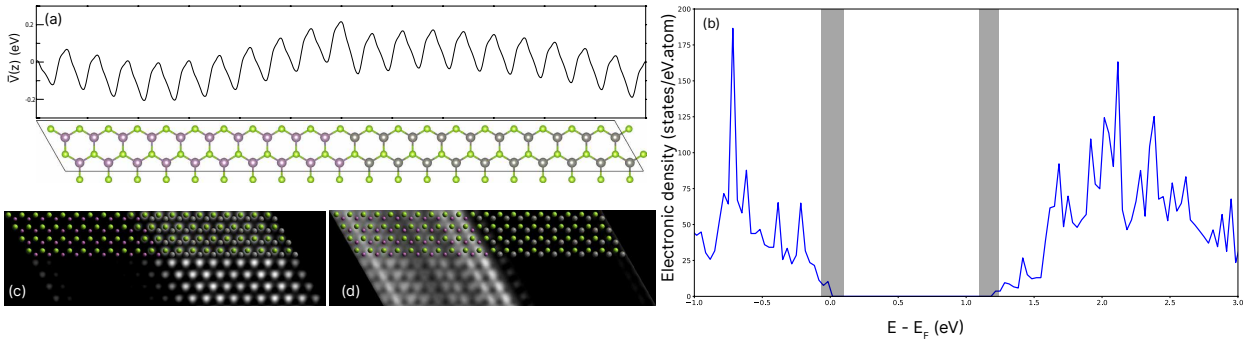

Figure 4.2: $MoSe_2/WSe_2$ junction. (a) potential and optimized interface geometry, (b) total DOS, (c /d) cross section of the partial DOS integrated on the shaded area on top of the valence band (/ bottom of the conduction band) and taken just above the upper Se plane.

The dipole extends on several unit cell distances and in a first calculation with a 20×4 cell (10×4 $MoSe_2$ unit cells and 10×4 WSe_2 unit cells) the evanescent states of the two junctions were overlapping. Here the distance between the two junctions is doubled (10 unit cells) and a strong decrease of the evanescent states is observed in the middle of the $MoSe_2$(WSe_2) part where they become negligible (partial DOS images in Fig. 4.2).

As already mentioned, junctions 1 and 2 are not symmetric. The electrostatic variations of the potential in Figure 4.2(a) are not symmetric either, the interface dipole has a larger

extension in junction 1 ($MoSe_2$ regions) than in junction 2 (WSe_2 regions).

4.3 Se vacancy in a $MoSe_2/WSe_2$ junction (20x4)

As already discussed, defects can play an important role at heterojunctions. As a first step towards the understanding of this role, we have modeled one Se vacancy at the $MoSe_2/WSe_2$ junction. The system is described by a 20×4 supercell and at convergence, the total energy variation is smaller than 0.04 eV. The different vacancy positions and the total energy as a function of the position are shown in figure 4.3. A first conclusion is that Se vacancy will be more favorable on the WSe_2 of the junction.

The corresponding DOS are shown in figure 4.4. They mainly show a shift of the vacancy peak in the gap. The partial charge density are shown in figure 4.5 They are integrated from 0 to 1 eV (1.3 eV) on the $MoSe_2$(WSe_2) side. The effect of the interface is here again rather small.

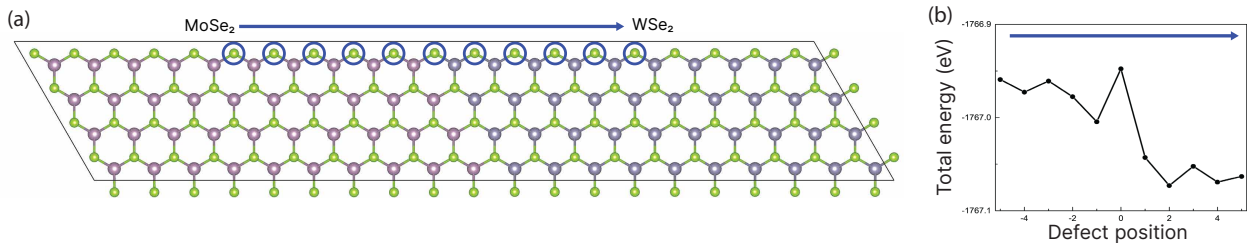

Figure 4.3: (a) Schematic of the supercell used for the calculation in top view. Blue circles give different defect positions. (b) Total energy as a function of defect positions.

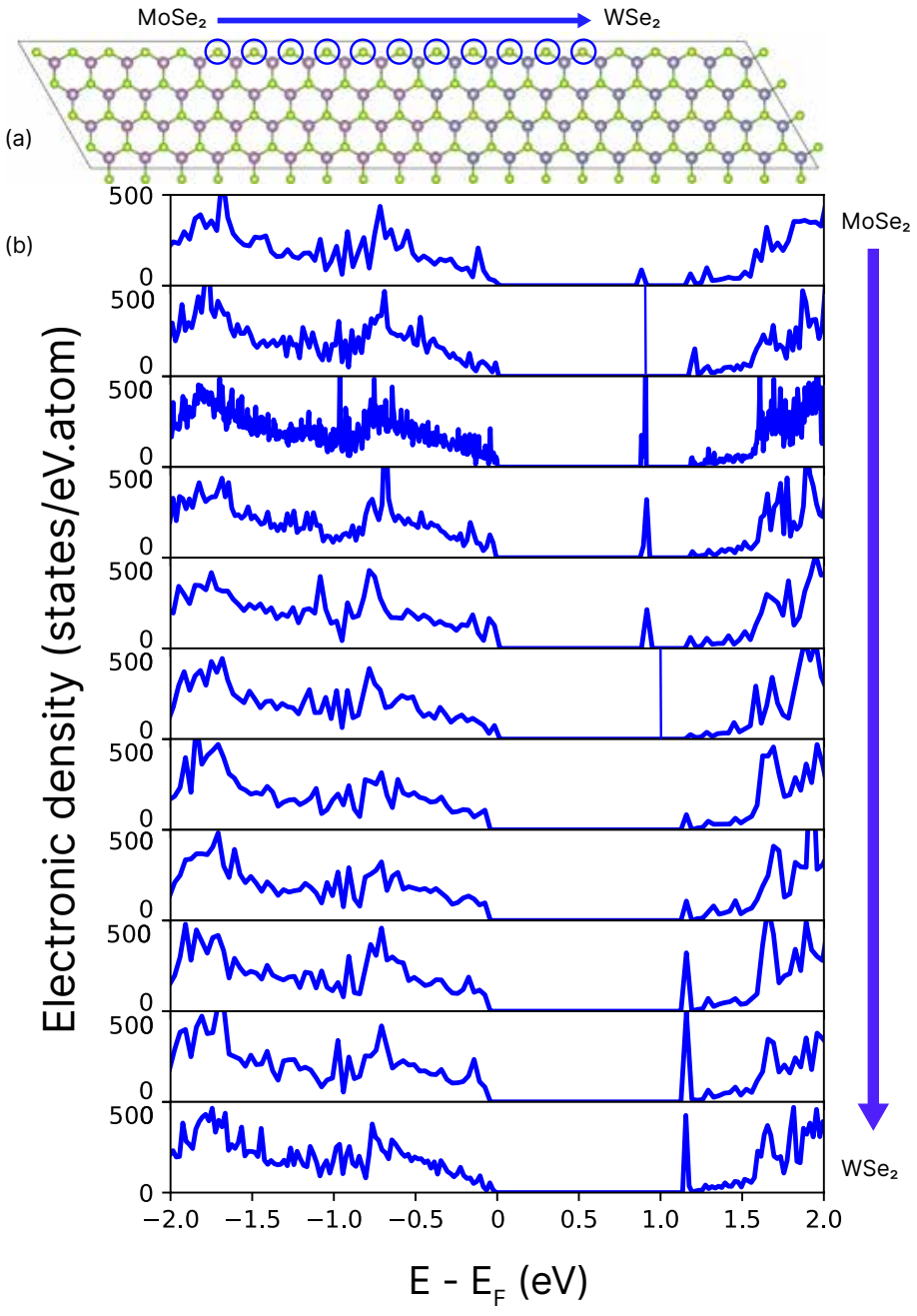

Figure 4.4: S vacancy in $MoSe_2/WSe_2$ heterojunction. (a) Lattice structure and (b) DOS. Blue circles, vectors represent the defect positions and directions where the Se atoms are being removed.

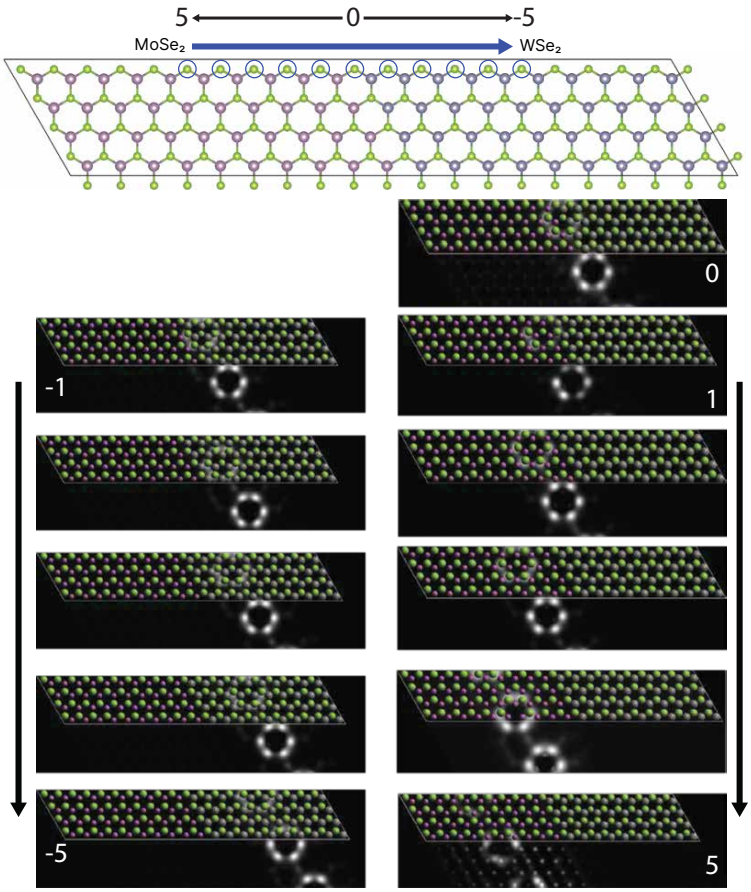

Figure 4.5: Cross section of the partial DOS integrated in the gap. Two unit cells are shown in the y direction, one with the atoms, the other one without.

4.4 Conclusion

In this chapter we showed that the $MoSe_2/WSe_2$ interface is nearly perfect at a different level: it induces very small relaxation, the electronic structure is just slightly affected and even defect properties remains similar on both sides. As a next step, it would be interesting to add different types of defects on both sides of the junction to create a $\mathtt{p}-\mathtt{n}$ junction.

Chapter 5

Epitaxial of TMDs on Metal Surface

Intercalation of alkali atoms within the lamellar transition metal dichalocgenides is a possible route to a new generation of batteries. It is also a way to induce structural phase transitions authorizing the realization of optical and electrical switches in this class of materials. The process of intercalation has been studied in thick or thin dichalcogenide films. Here, we address the case of a single-layer of molybdenum disulfide (MoS_2), deposited on a gold substrate. We studied the intercalation of cesium (Cs) in ultra-clean conditions (ultrahigh vacuum). This allows us to put in evidence that intercalation decouples MoS_2 from its substrate, significantly increasing the spacing distance. We discuss the strong charge donation from Cs to MoS_2, and the lifting of the hybridization between the orbitals of MoS_2 and of the substrate. Besides, we find an abnormal lattice expansion of MoS_2 that is related to the immediate vicinity of Cs, via strong electron doping and/or strong repulsion between Cs atoms. Intercalation is thermally activated, and so is the reverse process of de-intercalation. Our works open the route to a microscopic understanding of a process of relevance in several possible future technologies and shows the way to the manipulation of the properties of two-dimensional dichalcogenides by "under-cover" functionalization.

The work reported in this chapter has been performed in collaboration between Néel Institute, CEA-INAC, and CEA-SPECS. I was in charge of the fabrication and characterization by RHEED and STM at Néel Institute, and the fabrication was also done at the BM32 beamline of the ESRF, where RHEED and X-ray scattering experiments were made.

5.1 Introduction

The interest for transition metal dichalcogenide single-layers, initially spurred by the bright light emission found in molybdenum disulfide (MoS_2)[106;140] and the achievement of electrostatic switching of electrical conduction in MoS_2,[126] has revived activities devoted to the

synthesis of the materials. Efforts to reach the kind of structural quality found in mechanically exfoliated samples with bottom-up approaches – chemical vapour deposition,[38;89;98;166] chalcogenation of metal surfaces,[72;118;155] or molecular beam epitaxy, standard[145] or reactive under H_2S atmosphere[10;57;139] – are ongoing. Chalcogenation and reactive molecular beam epitaxy both usually require a metallic substrate. As-prepared samples are hence not suited to the study of some of the key properties of the material, *e.g.* those relating to excitons which become very short-lived due to the immediate vicinity of a metallic (substrate) charge reservoir, and electrical transport properties which are shunt by the conductive substrate. Besides, in the prototypical case of Au(111) as a substrate, MoS_2 does not retain the properties of the isolated material. Significant interaction between the electronic bands of MoS_2 and Au(111) was indeed detected[21] and the existence of a moiré pattern was found to induce a nanometer-scale modulation of this interaction.[80]

One way to alter this interaction is to "lift" MoS_2 from its surface. Such lifting is actually occurring spontaneously, across regions spanning typically a nanometer, when MoS_2 overhangs on Ångström-deep vacancy islands of the substrate.[81] Effective lifting may be achieved using an alternative strategy, namely by intercalating a layer of a species decoupling MoS_2 from its substrate. This strategy, already allowed to obtain quasi-free-standing graphene,[85;128;148] as shown by the observation of the typical dispersion of the π bands expected for isolated graphene. Beyond a simple decoupling of graphene, intercalation was also shown to induce high electron[146] and hole[151] doping, as well as superconductivity[65].

The intercalation of species in 2D materials others than graphene is a new topic of research. For instance, Yu *et al.*[163] studied the intercalation of small cation H^+ or Li^+ between the TMDC SL and the underlying substrate of SiO_2 and sapphire. Mahatha *et al.*[105] studied the intercalation of Bi atoms between a WS_2 single layer and a Ag substrate, and found that the TMDC was decoupled from its surface.

On the contrary, intercalation of thicker transition metal dichalcogenides, has been thoroughly investigated. Much like with graphite, a rich variety of systems with modulated structure in the direction perpendicular to the basal plane can be formed this way.[45] Using layers of alkali atoms, molecules, or transition metals as intercalants, unique properties including superconductivity and (anti)ferromagnetism have been found.[45] The ability to store (release) lithium atoms by intercalation (de-intercalation) also makes transition metal dichalcogenides possible electrode materials, both as cathode[110] and anode,[42;158] for Li-ion batteries. Electro-donnor intercalants besides promote a structural phase transition from a semiconducting phase to a metallic one,[4;37;40;54;56;122;154;156;159;161] with potential applications in data storage and reconfigurable electrical circuitry.

Here, we report on the intercalation and de-intercalation of alkali atoms, cesium (Cs). Unlike essentially all works addressing in-solution intercalation of thick or thin transition

metal dichalcogenide layers, the focus of our work is single-layer MoS_2 flakes, prepared on Au(111), and (de)intercalated under ultrahigh vacuum conditions. We find that the process of intercalation is thermally activated, being completed after few tens of minutes at a temperature of 550 K. A few 100 K above this temperature, deintercalation is active and completed within a few tens of minutes. We show that beyond charge donation and a change of the value of the electronic band-gap upon mere adsorption,[108] intercalation underneath MoS_2 lifts it from the substrate, and causes an abnormal lattice expansion parallel to the surface. Our analysis combines scanning tunneling microscopy (STM) performed at Néel Institute, reflection high-energy electron diffraction (RHEED) performed at Néel Institute and at the BM32 beamline of the ESRF, grazing incidence X-ray diffraction (GIXRD) and, reflectivity (XRR) both performed at BM32 by Dr. G. Renaud and R. Sant. These measurements have been made *in situ* and some *in operando* under ultrahigh vacuum.

5.2 Reactive molecular beam epitaxy of MoS_2 on Au(111)

Single-layer MoS_2 flakes were grown following the procedure described by Grønborg *et al.*[51] Two ultrahigh vacuum systems were used for our experiments. A first one is coupled to the X-ray synchrotron beam delivered at the BM32 beamline of the ESRF. It has a base pressure of 3×10^{-10} mbar and is equipped with a quartz micro-balance and a RHEED apparatus. The second one, with a base pressure of 2×10^{-10} mbar coupled to complementary *in situ* probes, a STM, a RHEED apparatus, and a quartz microbalance (as depicted in Fig. 5.1) (see also Fig. 1.2 *Chapter* 1). The samples were prepared in each system before being investigated by RHEED, STM, GIXRD, and XRR. Temperatures were measured with a pyrometer in both systems.

Our gold single-crystals was bought from Surface Preparation Laboratory and prepared under ultrahigh vacuum by sputter-anneal cycles. Each cycle consisted of 15-30 minutes of argon ion bombardment at room temperature and followed by 15-30 minutes of annealing at $\approx$ 850K, the Ar^+ energy was 1.0 keV and the Ar pressure of 2×10^{-5} mbar. Surface cleanliness was checked with STM imaging and RHEED. Evidences of the typical Au(111) herringbone reconstructions in both RHEED and STM (Fig. 5.2 (a,b)) confirmed the surface quality.

Molybdenum was evaporated using a high-purity rod heated by electron-beam bombardment, at a rate of ≈ 0.02 monolayer/min in ultrahigh vacuum chamber coupled to the X-ray beam and in the ultrahigh vacuum chamber coupled to the STM respectively (one monolayer referring to the surface coverage of a pseudomorphic Mo layer on Au(111)). The deposition rate was estimated with a quartz microbalance. In the setup installed at the ESRF, this estimate is relyable, within 10-20%. In the setup installed at Néel Institute, this estimate is

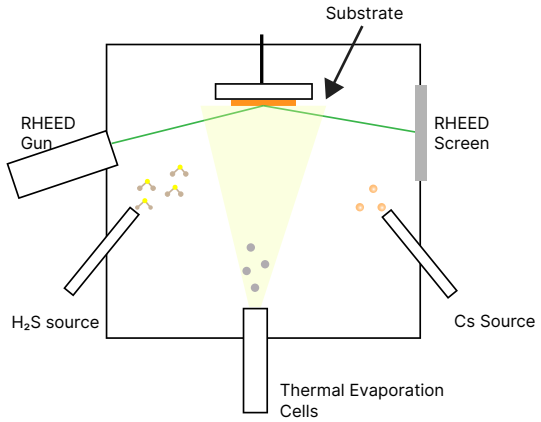

Figure 5.1: Schematic representation of an ultra high vacuum system setup.

much less reliable, due to the geometry of the ultrahigh vacuum chamber: the orientation of the electron-beam evaporator is strongly off the normal of the sample, and the quartz microbalance itself has a frame that can generate significant shadowing effects. This is why we rather rely on a callibration made with STM by measuring the coverage of Mo on the bare Au(111) surface. Figure 5.2(b) shows a typical example where Mo was evaporated for 20 min on Au(111). Molybdenum forms small clusters, here with a monolayer thickness, organized on the elbows of the herringbone reconstruction.

For introduction of H_2S in the ultrahigh vacuum chambers, we used a gas automatic distribution system (chamber coupled to the X-ray beam, it uses a mass flow controller and pneumatic valves governed by an automatic system (the control unit)) and a leak-valve (chamber coupled to the STM). In the latter system, large copper parts are found. Their surface was saturated by maintaining a 1×10^{-6} mbar of H_2S for 30 min. Without this treatment, residual gas analysis revealed that H_2S was prominently decomposed before even reaching the sample surface, which prevented MoS_2 growth.

The clean Au(111) surface was exposed to a partial pressure of H_2S ($P_{H_2S} \approx 1 \times 10^{-5}\mathrm{mbar}$) introduced in the ultrahigh vacuum systems, then molybdenum was deposited on the surface in presence of H_2S, and the sample was annealed to 850 K without the Mo atomic beam but still in presence of H_2S. This sequence was repeated four times to achieve a surface coverage of 60-80% with MoS_2. Cesium was deposited under ultrahigh vacuum with the help of a resistively heated high purity Cs dispenser from Saes Getter. We evaporated the Cs for 30 minutes under the current of 6.75 Å, the pressure during the evaporation is at 2.2×10^{-9} mbar.

STM measurements have been performed with our Omicron-STM1 apparatus, at room temperature under ultrahigh vacuum, in a dedicated chamber with a base pressure of 5×10^{-11} mbar. The STM topography was performed in constant current mode with the bias applied to the sample.

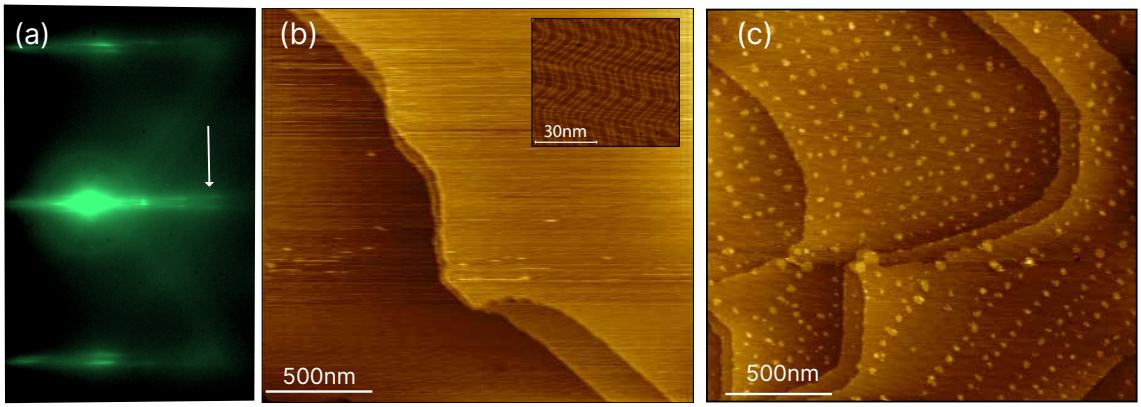

Figure 5.2: The clean Au(111) surface before (a,b) and after (c) exposing to Mo. The RHEED diffractogram is taken along the $[1\bar{1}0]$ azimuth. The STM topograph in (b) is taken with 2nA, 1V, the inset figure in (b) shows the herringbone reconstruction of Au(111) (2 nA, -2V).

5.3 Results and Discussion

5.3.1 Structure of MoS_2 single-layer islands on Au(111)

Figure 5.3a-d shows the typical diffraction patterns and morphology of the surface after growth. The MoS_2 flakes exhibit straight edges,[16] have an extension of the order of several 10 nm; in between the flakes the herringbone reconstruction of the bare Au(111) is visible. These observations are consistent with those in previous reports.[51;139]

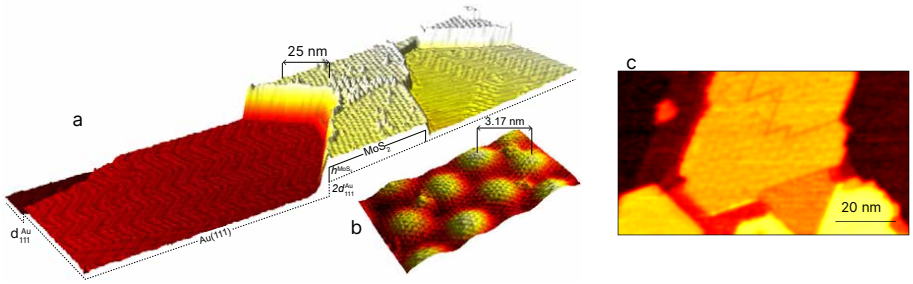

Figure 5.3: Single layer MoS_2 islands prepared on Au(111), (a) Three-dimensional view of a STM topograph (2 nA, -2 V) of single-layer MoS_2 islands formed on Au(111), with the herringbone reconstruction of the latter visible. (b) Three-dimensional view of an atomically-resolved STM topograph (1 nA, -2 V) of the moiré lattice between Au(111) and MoS_2. (*c*) Close-up STM view (1 nA, -2 V) of a MoS_2 island revealing linear defect.

A pronounced pattern, with 3.17 nm periodicity, is visible on the MoS_2 flakes presented in Figure 5.3 and 5.4. This pattern arises from the lattice mismatch with the substrate, and is described with an analogy to the optical moiré effect.[139] Careful analysis of atomically-resolved STM images and their Fourier transform (Figure 5.3b) allows to determine the size of the moiré unit cell. We find that the highest symmetry Au(111) and MoS_2 crystallographic

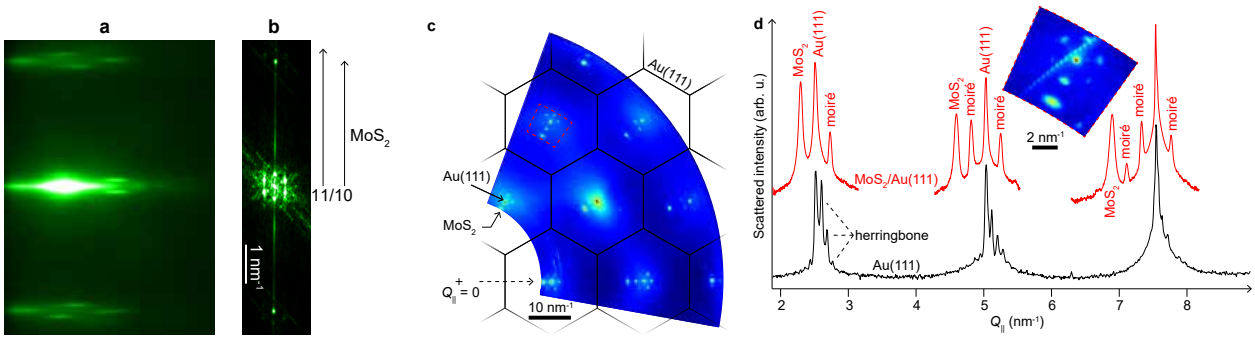

Figure 5.4: Single layer MoS_2 islands prepared on Au(111). (*a*) RHEED diffractogram (17 keV) along the [1$\bar{1}$0] azimuth. (*b*) Fast Fourier transform of an atomically resolved STM image, giving information consistent with the RHEED diffractogram. (*c*) In-plane cut of the reciprocal lattice, as measured with X-rays. (*d*) Radial scan of the X-ray scattered intensity, as a function of the modulus of the in-plane scattering vector $\mathbf{Q}_{\parallel}$ for Au(111) with and without single-layer MoS_2 islands on top. Inset: In-plane cut of the reciprocal lattice, in the area marked with a dotted frame in *c*.

direction are precisely aligned, and that the unit cell corresponds to the precise coincidence of 10 MoS_2 unit cells onto 11 Au(111) unit cells (10×11), consistent with a recent report.[10]

This moiré unit cell is consistent with the average reciprocal space lattice vector associated to the moiré, that is directly inferred from RHEED (Figure 5.3a) and GIXRD (Figure 5.4c,d) to be 0.3162 nm. We note that the moiré signals have strong intensity in GIXRD, translating a significant lattice distortion in MoS_2 and/or the topmost Au(111) planes with the in-plane periodicity of the moiré.

The full-width at half maximum of the MoS_2 peaks in a radial direction (Figure 5.4d) increases from 0.32 ± 0.05 nm$^-$1 to 0.54 ± 0.05 nm^{-1} from first to third order. This corresponds to a domain size of 10-18 nm and a distribution of in-plane lattice parameter of typically 0.6%.[52] Strikingly, the domain size is here smaller than the value of several 10 nm corresponding to the flake size that we determined by visual inspection of STM images. This difference simply shows that the flakes are not single-crystal, and actually consist each of (smaller) single-crystal grains. We indeed frequently observe linear defects within the flakes, at the boundary between laterally-shifted domains (see Figure 5.3(c)). Our interpretation is that at each of the four steps of the MoS_2 preparation, new MoS_2 islands nucleate, grow, and coalesce with pre-existing ones — no lattice re-organisation occurs that would eliminate the linear defect (so-called anti-phase grain boundaries) and yield large single-crystal flakes.

The Fourier transform of the total electronic density of the system along the out-of-plane direction is in fact directly measured in the XRR experiment whose result is shown in Figure 5.5b. In between the (000) and (111) crystallographic reflections of Au(111), we observe a

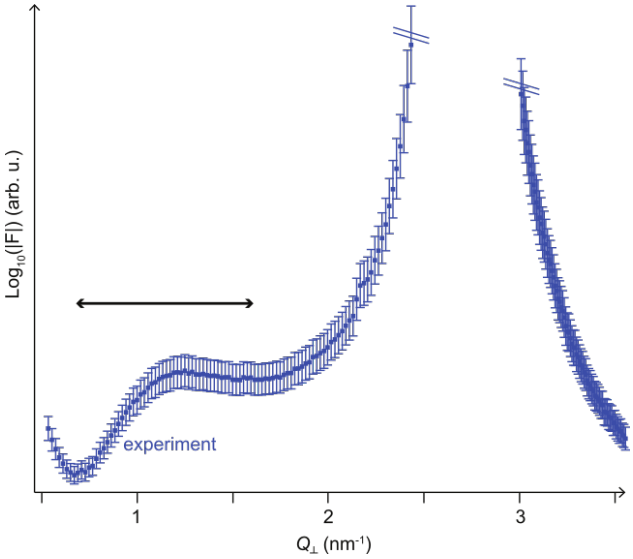

Figure 5.5: Square root of the X-ray reflectivity as function of the modulus of the out-of-plane scattering vector $Q_\perp$. The double arrow marks the distance between two destructive interference conditions.

rebound in the reflectivity. Qualitatively, the distance between the two minima is set by destructive interferences between the Au(111) lattice perpendicular to the surface and the MoS_2 layer. From this qualitative argument we estimate that destructive interferences occur between atomic planes whose interdistance is about three times the Au(111) interdistance. This agrees well with the value given by STM estimations.

5.3.2 Effects of Cs intercalation on the structure of MoS_2

The sample was first exposed to Cs under ultrahigh vacuum at room temperature. This treatment has several effects on diffraction patterns. First, the diffraction signal associated to MoS_2 progressively shows two components, one of which corresponding to an expansion of the lattice. We also observe an overall decreases in intensity as the Cs dose increases, which points to increased disorder. Second, the signals associated with the moiré lattice decrease in intensity, which suggests a reduction of the amplitude of the periodic lattice distortions associated with the spatially varying interaction between Au(111) and MoS_2.

These two effects get more prominent when the sample is annealed a few 100 K above room temperature, typically at 550 K (after Cs deposition), suggesting that kinetics is governing the surface processes here. After three steps, planar cuts in reciprocal space essentially feature the Au and MoS_2 peaks, with no sign of a moiré contribution and a new superstructure manifesting around the Au peaks (Figure 5.6a). In Figure 5.6b we show radial scans of the scattered intensity at different steps of the procedure we just described. The figure reveals the gradual change of the lineshape and position of the MoS_2 peaks together with

the progressive vanishing of the moiré peak.

A straightforward way to interpret these observations is to invoke intercalation of Cs in between MoS_2 and Au(111). As we have seen (Figure 5.5), without Cs significant hybridization and periodic lattice distortion are expected, which accounts for the strong moiré signals initially observed (Figure 5.4a,b). Conversely, the vanishing signal upon Cs deposition and annealing indicates that the atomic distortions related to the moiré are significantly reduced. This strongly suggests that hybridization effects are canceled, and we will see below that indeed intercalation is precisely expected to have this effect.

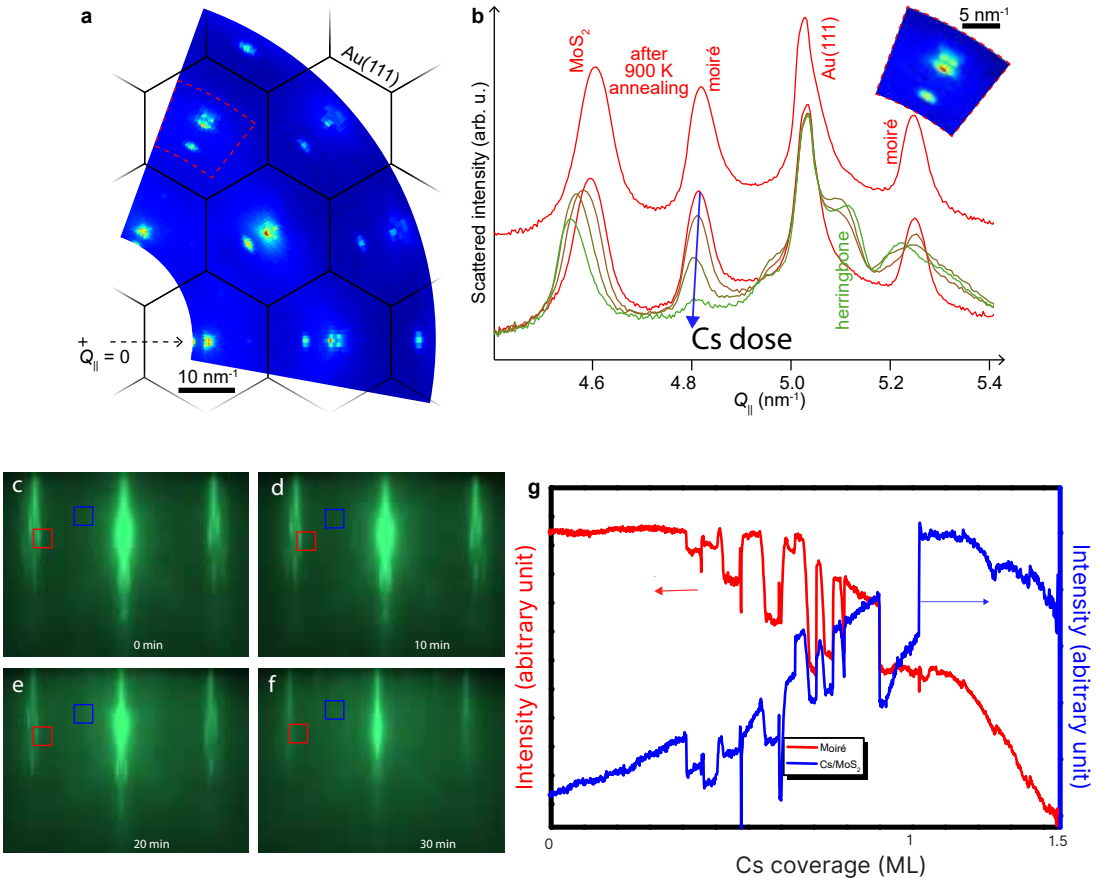

Figure 5.6: Structural changes in MoS_2 upon Cs intercalation. (a) In-plane reciprocal lattice measured with X-rays after Cs deposition and 550 K annealing. (b) Radial scan of the X-ray scattered intensity versus the in-plane momentum transfer $Q_{\parallel}$ after an increasing amount (red to green curves) of Cs has been deposited at room temperature, then annealed to 550 K, and to 870 K. Inset: high-resolution zoom in the area marked with a dotted frame in (a). (c-f) RHEED diffractograms (17 keV) after 0, 10, 20 and 30 minutes of Cs deposited. (g) Cut in the RHEED patterns averaged vertically within the red(blue) frames in (c-f), as a function of the Cs dose.

In the absence of a significant hybridization between MoS_2 and Au orbitals, the MoS_2 is no more strongly pinned on the substrate lattice. The question then arrises whether after

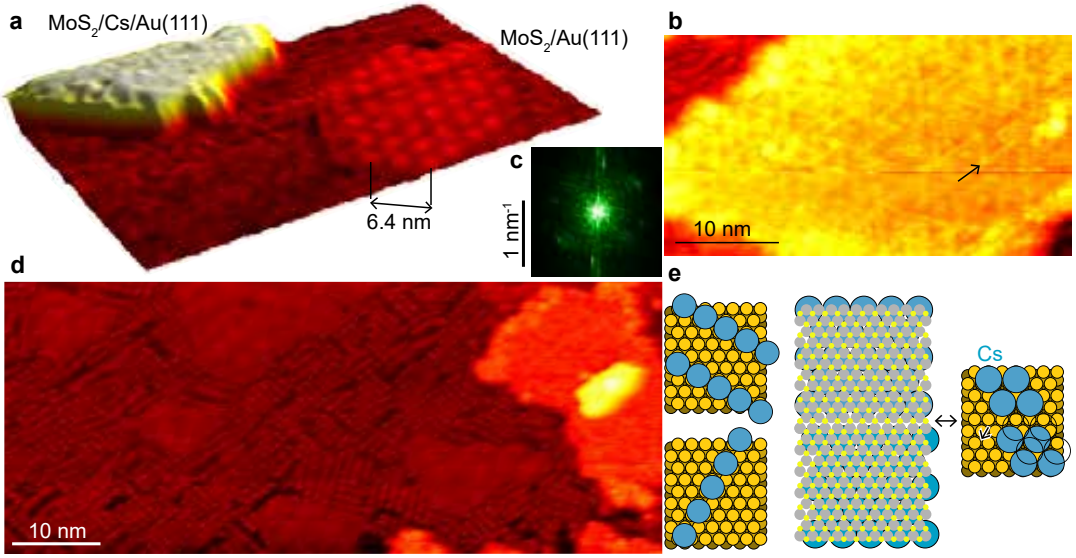

Figure 5.7: (*a*) Three-dimensional view of a STM topograph (1 nA, -0.5 V) of MoS_2 islands with and without intercalated Cs. (*b*) Close-up STM view (1 nA, -2 V) of a Cs-intercalated MoS_2 island revealing a pattern of lines. (*c*) Fast Fourier transform of STM images comprising MoS_2-free regions. (*d*) STM view (1 nA, -2 V) revealing Cs nanosticks on Au(111). (*e*) Nanostick patterns of Cs on Au (left); two intercalated (2×2) Cs domains and the corresponding grain boundary (dislocation) buried under MoS_2 and indicated with a double-arrow (center, right).

the MoS_2 growth and before intercalation of Cs, at room temperature, MoS_2 would not be compressively stressed (and strained) by the substrate. If this would be the case, then there would be a natural mechanical driving force for MoS_2 to expand its lattice after intercalation, which would account for the X-ray diffraction data. Based on first-principles calculations, Huang *et al.* predicted a similar temperature dependence of the in-plane lattice constant for single-layer and bulk MoS_2.[64] From 850 K (MoS_2 growth temperature) to 300 K, the lattices of MoS_2 and Au should then compress by 0.002 nm and 0.0026 nm in the surface plane respectively,[39;113] *i.e.* MoS_2 is expected to experience a residual ~0.2% compressive strain if it is locked on Au(111). Expansion in this range can thus be expected. This is however significantly smaller than the observed expansion, which amounts 1.4%.

What is the origin of this strong expansion, then? A structural phase transition (1H to 1T or 1T') is expected upon electron doping,[22] and Cs, a well-known electro-donnor species, might indeed donate the required amount of charges to MoS_2. Previous DFT calculations predicted that the 1H→1T structural phase transition does not induce, by itself, a significant lattice expansion. In fact, a marginal lattice contraction has even been predicted[36] while for a transition to a 1T' phase, indeed a strong expansion has been predicted recently[142]. An increasing amount of alkali atoms in the vicinity of MoS_2 is also expected to lead to

an increased lattice constant. In the related system of potassium inserted in between MoS_2 layers, DFT calculations predicted a significant lattice expansion, ascribed to either the stronger charge density within the Mo-S bonds or to repulsive interactions between the alkali atoms, which, due to electron donation, actually behave as cations.[7]

Obviously charge transfers with Cs will depend on the Cs density under the MoS_2 flakes: while Cs are in essence electro-donnor atoms, at high surface density, repulsion between the dipoles involving the ionized Cs is expected to reduce charge transfers.[86] In principle diffraction can inform us on the nature of the Cs phases, provided that they are ordered. In STM, we observe that on MoS_2-free regions Cs atoms form a pattern of ~5 nm-long nanosticks, some bunching across several 1 nm to several 10 nm, and having different orientations on the surface, also detected in the Fourier transform of the images (Figure 5.7c,d). Considering the observed periodicity, we propose two possible atomic structures for the Cs nanosticks (Figure 5.7e, left).

On MoS_2-covered regions, we are not able to detect this structure. The moiré lattice is not visible anymore (Figure 5.7a,b,c), which is consistent with the GIXRD data discussed above. Whether Cs forms an ordered structure or not underneath MoS_2 cannot be observed directly based on our STM measurements. Yet, we observe a nanoscale pattern of lines oriented along the three highest-symmetry direction of Au(111) and MoS_2 (120° orientations). This pattern may be related to that observed on another intercalated two-dimensional-material-on-metal system, graphene/Bi/Ir(111).[157] There, the pattern was interpreted as a network of dislocations in the intercalant's lattice, the lines corresponding to the boundaries between intercalated domains being shifted by a fraction of the lattice vector(s) of the intercalant's lattice. In the central and right panels of Figure 5.7e we have sketched a possible structure accounting for our STM observations, with two (2×2) Cs domains intercalated under MoS_2, and laterally shifted (at this point we cannot exclude that the Cs domains could be $(\sqrt{3}\times\sqrt{3})$ rather than (2×2), but similar configurations can be imagined with $(\sqrt{3} \times \sqrt{3})$ domains).

STM images taken after Cs deposition reveal that not all MoS_2 flakes have the same appearance (Figure 5.7a). Part of them are apparently higher, and exhibit no moiré pattern, while the other part has the same apparence as on the pristine MoS_2/Au(111) samples. This finding is consistent with the two-component character of the MoS_2 signal in GIXRD (Figure 5.6b), and indicates that Cs intercalation is not homogeneous.

Just like we did in the absence of Cs, we now address the structure of the sample in the direction perpendicular to the surface. The Fourier transform of the electronic density perpendicular to the surface is given by the XRR data. We observe that the XRR curves show faster oscillations, indicative of a larger distance between MoS_2 and Au(111) than in the absence of intercalated Cs (Figure 5.8).

As we have seen, increasing the temperature promotes intercalation of Cs underneath

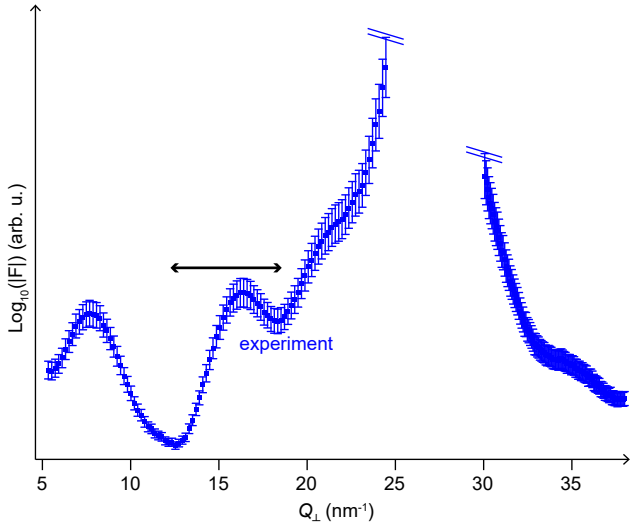

Figure 5.8: Increase of the MoS_2-substrate distance after Cs intercalation. Experimental X-ray reflectivity (normalized to its maximum value) as function of the modulus of the out-of-plane scattering vector $Q_\perp$ and with intercalated Cs. Note the distinct positions of the minima for the reflectivity with and without intercalated Cs (compare with Figure 5.5).

the MoS_2 flakes, which points to a kinetic barrier to intercalation (*e.g.* for passing through defects and/or for creating defects later acting as intercalation pathways). To further improve the efficiency of intercalation it is tempting to further increase temperature. A few K above 500 K however, another key process is activated: The moiré signal typical of a periodic lattice distortion re-appears in GIXRD, the MoS_2 peak shifts backwards corresponding to a compression of the atomic lattice (Figure 5.6b), and the wavelength of the oscillations in XRR increases suggesting a decreased distance between MoS_2 and Au(111). In fact, after 850 K annealing, the reciprocal lattice of the sample is very similar to that of the pristine sample, in other words at this temperature intercalated Cs atoms can diffuse outside of the MoS_2 flakes (*i.e.* they de-intercalate) and desorb to vacuum.

Conclusions

We showed that starting from MoS_2 flakes strongly coupling to the Au(111) substrate, with a short spacing and a substantial nanorippling, Cs intercalation lifts the flakes and flatens them. The process is thermally activated. De-intercalation is also thermally activated, but at higher temperatures. We found that Cs intercalation leads to an anomal ~1% expansion of the atomic lattice of MoS_2 parallel to the surface. This effect might originate from a strong electron donation of Cs atoms to the MoS_2. The decoupling we observe suggests that the presence of the intercalated layer prevents the hybridization of the sulfur and Au orbital.

Our works open new perspectives towards the manipulation of two-dimensional transition

metal dichalcogenides. Similarly to in-solution strategies,[37] intercalation could be exploited on MoS_2/Au(111) to facilitate the exfoliation of nanoscale flakes[57] or full layers.[10] Demonstrating further control on electronic or hole doping of MoS_2 with intercalated electro-donnor or electro-acceptor species is another exciting goal. A number of species, to be intercalated with varying doses, are relevant here, among the vast catalog of alkali atoms, transition metals, and molecules. Finally, as extensively demonstrated with bulk compounds in the past, intercalation opens new doors to achieve a variety of two-dimensional phases, structural ones, magnetic ones, and even superconducting ones.

Conclusions

There are several features that make two-dimensional (2D) transition metal dichalcogenides (TMDC) rather unique in terms of applications for optoelectronics. They can adopt different structures, each with a very different electronic band structure (e.g. MoS_2 is semiconducting in the 2H phase and metallic in the 1T phase). The relative stability of these structures has been reported to change with strain or electronic doping. While our DFT calculations confirm the former result, we could not drive clear conclusions regarding the latter. Besides adopting different structures, the electronic properties are strongly influenced by the number of layers, and our calculations confirm this well-known fact, that is illustrate by a transition from an indirect to a direct electronic bandgap when the TMDC is single-layer.

Defects in 2D TMDCs are also rather unique, simply because the displacement of atoms is not hindered in the direction perpendicular to the layers. Addressing the prototypical of MoS_2, which is probably the most studied 2D TMDC, we consider several substitutional defects at the metal and chalcogen sites and atomic vacancies. Our DFT calculations reveal sharp electronic states associated to the defects, and predict characteristic local density of states variations that serve as a guide to interpret scanning tunneling microscopy characterisation of a so far unknown kind of defect. We attribute these defects, found in MoS_2 exfoliated from a bulk crystal formed using a special high temperature / high pressure process, as N/S substitionals. These defects have been shown to weakly trap excitons in the material, as shown in photoluminescence experiments performed by our collaborators.

Moving to the DFT study of a almost homostructural $MoSe_2/WSe_2$ type-II planar junction, we were interested in understanding the way the different band structures of the two materials align. The band structure alignment is known to result in an extended interface dipole in traditional 3D semiconductors. As a preliminary step, we addressed the effect of finite size in WSe_2, when the material is in the form of a ribbon. Our simulations revealed that electronic states lying within the bandgap of WSe_2 are associated to the low-coordinated edge atoms. In the homostructural $MoSe_2/WSe_2$ planar junction, very few deformations are found. We found no evidence of electronic states within the bandgap of these materials, i.e. the edge states found in the WSe_2 ribbon are suppressed due to the passivation of atoms at the interface between $MoSe_2$ and WSe_2. This implies an absence of pinning of the Fermi level

in the junction, a desirable feature in p-n junctions. We do find that the junctions is of type II, with states on the WSe_2 side only at the top of the valence band and states on the $MoSe_2$ side only at the bottom of the conduction band. We also observe charge transfer between WSe_2 and $MoSe_2$, hence an interface dipole. Finally, studying the role of a Se vacancy in the system, we found localised defect states whose energy varies depending on the location of the defect in the structure: the energy is found within the gap when the defect is in the $MoSe_2$ side or at the interface, and presumably in the conduction band when it is in the WSe_2 side.

Our experimental study of single-layer MoS_2 on a Au(111) substrate revealed that TMDC grows in the form of well-oriented islands. This natural orientation selection is desirable and actually rarely possible with other kinds of substrates. Due to lattice mismatch, MoS_2 develops a moiré pattern with nanometer-scale periodicity on Au(111). This pattern corresponds to a strong, locally-varying interaction between the substrate and the overlayer, and is evident in the diffraction data. Deposition of Cs onto the samples leads to spontaneous intercalation underneath of MoS_2. A signature of this intercalation is the disappearance of the moiré signal in diffraction experiments, and an increase on the MoS_2/Au(111) distance that we qualitatively revealed with X-ray reflectivity experiments. Together with this lift-off of the MoS_2 a planar expansion of MoS_2 occurs, which seems related to the charge donation from Cs atoms. We find that the intercalation can be promoted by temperature, and that above a certain temperature, deintercalation occurs, eventually leading to the re-coupling of MoS_2 with its substrate.

Perspectives

In this thesis, TMDCs with different kind of point defects were characterized and the interaction of TMDCs with one another and with metallic substrate were also studied, however there are a lot of work need stills to be done. Let us mention some perspectives as follows:

- Beside point defects studied in Chapter 3, different kind of defects such as line defects, charge defects, etc are feasible. On the other hand, our calculations does not consider the appearance of substrate. It might interest to understand how defects behave (mechanically and electronically) with different type of substrates;
- The TMDCs heterojunctions have been successfully fabricated by other groups (see e.g. Bellus[12], Huang[62]), provided an ultrafast charge transfer in the order of dozen femtoseconds. However, the effect of point defects in such systems are still missing and can be address in further study;
- As we successful fabricate the MoS_2/Au(111) system, it showed the possibility of exploiting to facilitate the exfoliation of nanoscale flakes or full layers. Further study on electronic or hole doping of MoS_2 with intercalated electro-donor or electro-acceptor species can be a further goal.

Appendix A

```
1  // POSCAR   (1)
2  WS2-2H-a=3.16-dS-S=3.13   (2)
3  1.000000   (3)
4  3.160  0.000000 0.000000
5  -1.58  2.736640 0.000000   (4)
6  0.00   0.000000 25.00000
7  W  S      (5)
8  1  2      (6)
9  Direct   (7)
10 0.666666 0.333334 0.500000 F F F
11 0.333333 0.666667 0.437400 T T T (8)
12 0.333333 0.666667 0.562600 T T T
```

(1) Comment
(2) Optional name of the system
(3) Universal scaling factor
(4) Bravais lattice vector
(5) Atom symbols, separated by space
(6) Number of atoms per species, with the same position as in (5)
(7) Coordinates in term of Direct or Cartesian
(8) Positions of each atoms.

```
1
2  // INCAR
3  SYSTEM = WS2_GGA_08_01_2017
4  General
5  ISTART=0
6
7  Relaxation Electronic
8  PREC= Medium
9  LWAVE=.FALSE.
10
11
12 Relaxation ionique
13 NSW=100
14 IBRION=2
15
16
17 DOS related values:
18 ISMEAR =  -5
19 EMIN   =   -5 ;  EMAX = 5
```

The INCAR file is the configuration file that determines the main calculation paramters. The code above shows an example on how we input the INCAR file. The first 3 lines are comment lines. The START tells VASP to start the calculation from scratch with medium precision (PREC= Medium by changing the cutoff energy). In this calculation, the set of wave-function is not written out to a file (by setting LWAVE=.FALSE.). The ionic relaxation is perform by using conjugate-gradient algorithm (IBRION=2), and the maximum number of ionic steps is set to be 100 (NSW=100). The ISMEAR determines how the partial occupancies f_{nk} are set for each orbital, in this case, it used tetrahedron method with Blochl corrections. (https://cms.mpi.univie.ac.at/wiki/index.php/ISMEAR) The DOS is evaluate within the energy range of [-5, 5] eV (EMIN = -5 ; EMAX = 5)

The complete set of configuration can be found in the website of VASP:
https://cms.mpi.univie.ac.at/wiki/index.php/Category:INCAR

The file KPOINTS contains the k-point coordinates and weights or the mesh size for creating the k-point grid. For instance:

```
// KPOINTS
Automatic
0
GMonk-P
6 6 1
```

To generate strings of k-points connecting specific points of the Brillouin zone, the third line of the KPOINTS file must start with an L for line-mode, and the following specifies group of (start-end points):

```
Band structure
50
line-mode
reciprocal
0.0 0.0 0.0 ! G
0.5 0.0 0.0 ! M

0.5 0.0 0.0 ! M
0.3333 0.3333 0.0 ! K

0.3333 0.3333 0.0 ! K
0.0 0.0 0.0 ! G
```

Bibliography

[1] H. Abe, K. Kataoka, K. Ueno, and A. Koma. Scanning Tunneling Microscope Observation of the Metal-Adsorbed Layered Semiconductor Surfaces. *Jpn. J. Appl. Phys.*, 34(Part 1, No. 6B):3342–4445, Jun. 1995.

[2] A. S. Achoyan, A. É. Yesayan, É. M. Kazaryan, and S. G. Petrosyan. Two-dimensional $\mathfrak{p} - \mathfrak{n}$ junction under equilibrium conditions. *Semiconductors*, 36(8):903–907, Aug. 2002.

[3] R. Addou, L. Colombo, and R. M. Wallace. Surface Defects on Natural MoS_2. *ACS Applied Materials & Interfaces*, 7(22):11921–11929, May. 2015.

[4] M. Ahmad, E. Müller, C. Habenicht, R. Schuster, M. Knupfer, and B. Büchner. Semiconductor-to-Metal Transition in the Bulk of WSe_2 Upon Potassium Intercalation. *J Physics: Condens. Matter.*, 29(16):165502, 2017.

[5] M. N. Ali, J. Xiong, S. Flynn, J. Tao, Q. D. Gibson, L. M. Schoop, T. Liang, N. Haldolaarachchige, M. Hirschberger, N. P. Ong, and R. J. Cava. Large, non-saturating magnetoresistance in WTe_2. *Nature*, 514(7521):205–208, Sep. 2014.

[6] M. Amani, D.-H. Lien, D. Kiriya, J. Xiao, A. Azcatl, J. Noh, S. R. Madhvapathy, R. Addou, S. KC, M. Dubey, K. Cho, R. M. Wallace, S.-C. Lee, J.-H. He, J. W. Ager, X. Zhang, E. Yablonovitch, and A. Javey. Near-unity photoluminescence quantum yield in MoS_2. *Science*, 350(6264):1065–1068, Nov. 2015.

[7] A. Andersen, S. M. Kathmann, M. A. Lilga, K. O. Albrecht, R. T. Hallen, and D. Mei. First-Principles Characterization of Potassium Intercalation in Hexagonal 2H-MoS_2. *J. Phys. Chem. C*, 116(2):1826–1832, 2012.

[8] R. Anderson. Germanium-gallium arsenide heterojunctions [letter to the editor]. *IBM Journal of Research and Development*, 4(3):283–287, 1960.

[9] A. Artaud. *Quasi-ordre à longue distance et défauts topologiques dans le graphène sur rhénium étudié par microscopie à effet tunnel.* PhD thesis, 2017.

[10] H. Bana, E. Travaglia, L. Bignardi, P. Lacovig, C. E. Sanders, M. Dendzik, M. Michiardi, M. Bianchi, D. Lizzit, F. Presel, D. D. Angelis, N. Apostol, P. K. Das, J. Fujii, I. Vobornik, R. Larciprete, A. Baraldi, P. Hofmann, and S. Lizzit. Epitaxial Growth of Single-Orientation High-Quality MoS_2 Monolayers. *2D Mater.*, 5(3):035012, 2018.

[11] S. Barja, S. Refaely-Abramson, B. Schuler, D. Y. Qiu, A. Pulkin, S. Wickenburg, H. Ryu, M. M. Ugeda, C. Kastl, C. Chen, et al. Identifying substitutional oxygen as a prolific point defect in monolayer transition metal dichalcogenides with experiment and theory. *arXiv preprint arXiv:1810.03364*, 2018.

[12] M. Z. Bellus, M. Mahjouri-Samani, S. D. Lane, A. D. Oyedele, X. Li, A. A. Puretzky, D. Geohegan, K. Xiao, and H. Zhao. Photocarrier Transfer across Monolayer $MoS_2/MoSe_2$ Lateral Heterojunctions. *ACS Nano*, 12(7):7086–7092, Jun. 2018.

[13] C. Berger, Z. Song, T. Li, X. Li, A. Y. Ogbazghi, R. Feng, Z. Dai, A. N. Marchenkov, E. H. Conrad, P. N. First, and W. A. de Heer. Ultrathin Epitaxial Graphite: 2D Electron Gas Properties and a Route toward Graphene-based Nanoelectronics. *J. Phys. Chem. B*, 108(52):19912–19916, Dec. 2004.

[14] M. Bernardi, M. Palummo, and J. C. Grossman. Extraordinary sunlight absorption and one nanometer thick photovoltaics using two-dimensional monolayer materials. *Nano Lett.*, 13(8):3664–3670, 2013.

[15] G. Binnig, H. Rohrer, C. Gerber, and E. Weibel. 7×7 reconstruction on Si(111) resolved in real space. *Phys. Rev. Lett*, 50(2):120–123, Jan. 1983.

[16] M. Bollinger, J. Lauritsen, K. W. Jacobsen, J. K. Nørskov, S. Helveg, and F. Besenbacher. One-Dimensional Metallic Edge States in MoS_2. *Phys. Rev. Lett.*, 87(19):196803, 2001.

[17] M. V. Bollinger, K. W. Jacobsen, and J. K. Nørskov. Atomic and electronic structure of MoS_2 nanoparticles. *Phys. Rev. B*, 67(8), Feb. 2003.

[18] L. Britnell, R. Ribeiro, A. Eckmann, R. Jalil, B. Belle, A. Mishchenko, Y.-J. Kim, R. Gorbachev, T. Georgiou, S. Morozov, et al. Strong light-matter interactions in heterostructures of atomically thin films. *Science*, 340(6138):1311–1314, 2013.

[19] J. L. Brito, M. Ilija, and P. Hernández. Thermal and reductive decomposition of ammonium thiomolybdates. *Thermochimica Acta*, 256(2):325–338, Jun. 1995.

[20] B. E. Brown. The crystal structures of WTe_2 and high-temperature $MoTe_2$. *Acta Crystallogr.*, 20(2):268–274, Feb. 1966.

[21] A. Bruix, J. A. Miwa, N. Hauptmann, D. Wegner, S. Ulstrup, S. S. Grønborg, C. E. Sanders, M. Dendzik, A. G. Čabo, M. Bianchi, J. V. Lauritsen, A. A. Khajetoorians, B. Hammer, and P. Hofmann. Single-Layer MoS_2 on Au(111): Band Gap Renormalization and Substrate Interaction. *Phys. Rev. B*, 93(16):165422, 2016.

[22] T. Brumme, M. Calandra, and F. Mauri. First-principles theory of field-effect doping in transition-metal dichalcogenides: Structural properties, electronic structure, hall coefficient, and electrical conductivity. *Phys. Rev. B*, 91(15):155436, 2015.

[23] M. Calandra. Chemically exfoliated single-layer MoS_2: Stability, lattice dynamics, and catalytic adsorption from first principles. *Phys. Rev. B*, 88(24):245428, 2013.

[24] F. Ceballos, M. Z. Bellus, H.-Y. Chiu, and H. Zhao. Ultrafast Charge Separation and Indirect Exciton Formation in a $MoS_2/MoSe_2$ Van der Waals Heterostructure. *ACS Nano*, 8(12):12717–12724, Nov. 2014.

[25] L. Chen, B. Liu, A. N. Abbas, Y. Ma, X. Fang, Y. Liu, and C. Zhou. Screw-Dislocation-Driven Growth of Two-Dimensional Few-Layer and Pyramid-like WSe_2 by Sulfur-Assisted Chemical Vapor Deposition. *ACS Nano*, 8(11):11543–11551, Oct.. 2014.

[26] M. Chhowalla, H. S. Shin, G. Eda, L.-J. Li, K. P. Loh, and H. Zhang. The chemistry of two-dimensional layered transition metal dichalcogenide nanosheets. *Nature chemistry*, 5(4):263, 2013.

[27] S. S. Chou, N. Sai, P. Lu, E. N. Coker, S. Liu, K. Artyushkova, T. S. Luk, B. Kaehr, and C. J. Brinker. Understanding catalysis in a multiphasic two-dimensional transition metal dichalcogenide. *Nature communications*, 6:8311, 2015.

[28] K. Chrissafis, M. Zamani, K. Kambas, J. Stoemenos, N. Economou, I. Samaras, and C. Julien. Structural studies of MoS_2 intercalated by lithium. *Mater. Sci. Eng., B*, 3(1-2):145–151, 1989.

[29] J. N. Coleman, M. Lotya, A. ONeill, S. D. Bergin, P. J. King, U. Khan, K. Young, A. Gaucher, S. De, R. J. Smith, I. V. Shvets, S. K. Arora, G. Stanton, H.-Y. Kim, K. Lee, G. T. Kim, G. S. Duesberg, T. Hallam, J. J. Boland, J. J. Wang, J. F. Donegan, J. C. Grunlan, G. Moriarty, A. Shmeliov, R. J. Nicholls, J. M. Perkins, E. M. Grieveson, K. Theuwissen, D. W. McComb, P. D. Nellist, and V. Nicolosi. Two-Dimensional Nanosheets Produced by Liquid Exfoliation of Layered Materials. *Science*, 331(6017):568–571, Feb. 2011.

[30] C. Cong, J. Shang, X. Wu, B. Cao, N. Peimyoo, C. Qiu, L. Sun, and T. Yu. Synthesis and Optical Properties of Large-Area Single-Crystalline 2D Semiconductor WS_2 Monolayer from Chemical Vapor Deposition. *Advanced Optical Materials*, 2(2):131–136, Dec.. 2013.

[31] H. J. Conley, B. Wang, J. I. Ziegler, R. F. Haglund Jr, S. T. Pantelides, and K. I. Bolotin. Bandgap engineering of strained monolayer and bilayer MoS_2. *Nano Lett.*, 13(8):3626–3630, 2013.

[32] M. Dendzik, A. Bruix, M. Michiardi, A. S. Ngankeu, M. Bianchi, J. A. Miwa, B. Hammer, P. Hofmann, and C. E. Sanders. Substrate-induced semiconductor-to-metal transition in monolayer WS_2. *Phys. Rev. B*, 96(23), Dec.. 2017.

[33] R. G. Dickinson and L. Pauling. The crystal structure of molybdenite. *Journal of the American Chemical Society*, 45(6):1466–1471, 1923.

[34] K. Dolui, I. Rungger, C. D. Pemmaraju, and S. Sanvito. Possible doping strategies for MoS_2 monolayers: An *ab-initio* study. *Phys. Rev. B*, 88(7), Aug. 2013.

[35] S. Dubey, S. Lisi, G. Nayak, F. Herziger, V.-D. Nguyen, T. L. Quang, V. Cherkez, C. González, Y. J. Dappe, K. Watanabe, T. Taniguchi, L. Magaud, P. Mallet, J.-Y. Veuillen, R. Arenal, L. Marty, J. Renard, N. Bendiab, J. Coraux, and V. Bouchiat. Weakly Trapped, Charged, and Free Excitons in Single-Layer MoS_2 in the Presence of Defects, Strain, and Charged Impurities. *ACS Nano*, 11(11):11206–11216, Oct. 2017.

[36] K.-A. N. Duerloo, Y. Li, and E. J. Reed. Structural Phase Transitions in Two-Dimensional Mo-and W-Dichalcogenide Monolayers. *Nat. Commun.*, 5:4214, 2014.

[37] G. Eda, H. Yamaguchi, D. Voiry, T. Fujita, M. Chen, and M. Chhowalla. Photoluminescence from Chemically Exfoliated MoS_2. *Nano Lett.*, 11(12):5111–5116, Dec.. 2011.

[38] S. M. Eichfeld, L. Hossain, Y.-C. Lin, A. F. Piasecki, B. Kupp, A. G. Birdwell, R. A. Burke, N. Lu, X. Peng, J. Li, A. Azcati, S. McDonnel, R. M. Wallace, M. J. Kim, T. S. Mayer, J. M. Rewing, and J. A. Robinson. Highly Scalable, Atomically Thin WSe_2 Grown via Metal-Organic Chemical Vapor Deposition. *ACS Nano*, 9(2):2080–2087, 2015.

[39] S. El-Mahalawy and B. Evans. The Thermal Expansion of 2H-MoS_2, 2H-$MoSe_2$ and 2H-WSe_2 between 20 and 800°C. *J. Appl. Cryst.*, 9(5):403–406, 1976.

[40] X. Fan, P. Xu, D. Zhou, Y. Sun, Y. C. Li, M. A. T. Nguyen, M. Terrones, and T. E. Mallouk. Fast and Efficient Preparation of Exfoliated 2H-MoS_2 Nanosheets by

Sonication-Assisted Lithium Intercalation and Infrared Laser-Induced 1T to 2H Phase Reversion. *Nano Lett.*, 15(9):5956–5960, 2015.

[41] H. Fang, C. Battaglia, C. Carraro, S. Nemsak, B. Ozdol, J. S. Kang, H. A. Bechtel, S. B. Desai, F. Kronast, A. A. Unal, G. Conti, C. Conlon, G. K. Palsson, M. C. Martin, A. M. Minor, C. S. Fadley, E. Yablonovitch, R. Maboudian, and A. Javey. Strong interlayer coupling in Van der Waals heterostructures built from single-layer chalcogenides. *Proceedings of the National Academy of Sciences*, 111(17):6198–6202, Apr. 2014.

[42] C. Feng, J. Ma, H. Li, R. Zeng, Z. Guo, and H. Liu. Synthesis of Molybdenum Disulfide (MoS_2) for Lithium Ion Battery Applications. *Mater. Res. Bull.*, 44(9):1811–1815, 2009.

[43] F. Finocchi. *Density Functional Theory for Beginners Basic Principles and Practical Approaches*. 2011.

[44] C. Freysoldt, B. Grabowski, T. Hickel, J. Neugebauer, G. Kresse, A. Janotti, and C. G. V. de Walle. First-principles calculations for point defects in solids. *Rev. Mod. Phys*, 86(1):253–305, Mar. 2014.

[45] R. Friend and A. Yoffe. Electronic Properties of Intercalation Complexes of the Transition Metal Dichalcogenides. *Adv. Phys.*, 36(1):1–94, 1987.

[46] S. Ganorkar, J. Kim, Y.-H. Kim, and S.-I. Kim. Effect of precursor on growth and morphology of MoS2 monolayer and multilayer. *Journal of Physics and Chemistry of Solids*, 87:32–37, Dec.. 2015.

[47] Y. Gong, S. Lei, G. Ye, B. Li, Y. He, K. Keyshar, X. Zhang, Q. Wang, J. Lou, Z. Liu, R. Vajtai, W. Zhou, and P. M. Ajayan. Two-Step Growth of Two-Dimensional WSe_2/$MoSe_2$ Heterostructures. *Nano Lett.*, 15(9):6135–6141, Aug. 2015.

[48] Y. Gong, J. Lin, X. Wang, G. Shi, S. Lei, Z. Lin, X. Zou, G. Ye, R. Vajtai, B. I. Yakobson, H. Terrones, M. Terrones, B. K. Tay, J. Lou, S. T. Pantelides, Z. Liu, W. Zhou, and P. M. Ajayan. Vertical and in-plane heterostructures from WS_2/MoS_2 monolayers. *Nature Materials*, 13(12):1135–1142, Sep. 2014.

[49] C. González, B. Biel, and Y. J. Dappe. Theoretical characterisation of point defects on a MoS_2 monolayer by scanning tunnelling microscopy. *Nanotechnology*, 27(10):105702, Feb. 2016.

[50] S. Grimme. Semiempirical GGA-type density functional constructed with a long-range dispersion correction. *J. Comput. Chem*, 27(15):1787–1799, 2006.

[51] S. S. Grønborg, S. Ulstrup, M. Bianchi, M. Dendzik, C. E. Sanders, J. V. Lauritsen, P. Hofmann, and J. A. Miwa. Synthesis of Epitaxial Single-Layer MoS_2 on Au(111). *Langmuir*, 31(35):9700–9706, 2015.

[52] A. Guinier. *X-ray diffraction in crystals, imperfect crystals, and amorphous bodies.* Dover Publications, 1994.

[53] Y. Guo, D. Liu, and J. Robertson. Chalcogen vacancies in monolayer transition metal dichalcogenides and fermi level pinning at contacts. *Appl. Phys. Lett*, 106(17):173106, Apr. 2015.

[54] Y. Guo, D. Sun, B. Ouyang, A. Raja, J. Song, T. F. Heinz, and L. E. Brus. Probing the Dynamics of the Metallic-to-Semiconducting Structural Phase Transformation in MoS_2 Crystals. *Nano Lett.*, 15(8):5081–5088, 2015.

[55] F. Hanke and J. Björk. Structure and local reactivity of the Au(111) surface reconstruction. *Phys. Rev. B*, 87(23), Jun. 2013.

[56] J. Heising and M. G. Kanatzidis. Structure of restacked MoS_2 and WS_2 elucidated by electron crystallography. *J. Am. Chem. Soc*, 121(4):638–643, 1999.

[57] S. Helveg, J. V. Lauritsen, E. Lægsgaard, I. Stensgaard, J. K. Nørskov, B. Clausen, H. Topsøe, and F. Besenbacher. Atomic-scale structure of single-layer mos_2 nanoclusters. *Phys. Rev. Lett.*, 84(5):951, 2000.

[58] Y. Hernandez, V. Nicolosi, M. Lotya, F. M. Blighe, Z. Sun, S. De, I. T. McGovern, B. Holland, M. Byrne, Y. K. GunKo, J. J. Boland, P. Niraj, G. Duesberg, S. Krishnamurthy, R. Goodhue, J. Hutchison, V. Scardaci, A. C. Ferrari, and J. N. Coleman. High-yield production of graphene by liquid-phase exfoliation of graphite. *Nature Nanotechnology*, 3(9):563–568, Aug. 2008.

[59] P. Hohemberg and W. Kohn. Inhomogeneous electron gas. *Phys. Rev. B*, 136:864, 1964.

[60] J. Hong, Z. Hu, M. Probert, K. Li, D. Lv, X. Yang, L. Gu, N. Mao, Q. Feng, L. Xie, et al. Exploring atomic defects in molybdenum disulphide monolayers. *Nature communications*, 6:6293, 2015.

[61] X. Hong, J. Kim, S.-F. Shi, Y. Zhang, C. Jin, Y. Sun, S. Tongay, J. Wu, Y. Zhang, and F. Wang. Ultrafast charge transfer in atomically thin MoS_2/WS_2 heterostructures. *Nature Nanotechnology*, 9(9):682–686, Aug. 2014.

[62] C. Huang, S. Wu, A. M. Sanchez, J. J. P. Peters, R. Beanland, J. S. Ross, P. Rivera, W. Yao, D. H. Cobden, and X. Xu. Lateral heterojunctions within monolayer $MoSe_2/WSe_2$ semiconductors. *Nature Materials*, 13(12):1096–1101, Aug. 2014.

[63] J.-K. Huang, J. Pu, C.-L. Hsu, M.-H. Chiu, Z.-Y. Juang, Y.-H. Chang, W.-H. Chang, Y. Iwasa, T. Takenobu, and L.-J. Li. Large-Area Synthesis of Highly Crystalline WSe_2 Monolayers and Device Applications. *ACS Nano*, 8(1):923–930, Dec.. 2013.

[64] L. F. Huang, P. L. Gong, and Z. Zeng. Correlation between Structure, Phonon Spectra, Thermal Expansion, and Thermomechanics of Single-Layer MoS_2. *Phys. Rev. B*, 90(4):045409, 2014.

[65] S. Ichinokura, K. Sugawara, A. Takayama, T. Takahashi, and S. Hasegawa. Superconducting Calcium-Intercalated Bilayer Graphene. *ACS Nano*, 10(2):2761–2765, Jan. 2016.

[66] D. Jariwala, V. K. Sangwan, D. J. Late, J. E. Johns, V. P. Dravid, T. J. Marks, L. J. Lauhon, and M. C. Hersam. Band-like transport in high mobility unencapsulated single-layer MoS_2 transistors. *Applied Physics Letters*, 102(17):173107, 2013.

[67] W. Jin, P.-C. Yeh, N. Zaki, D. Zhang, J. T. Sadowski, A. Al-Mahboob, A. M. van Der Zande, D. A. Chenet, J. I. Dadap, I. P. Herman, et al. Direct measurement of the thickness-dependent electronic band structure of MoS_2 using angle-resolved photoemission spectroscopy. *Phys. Rev. Lett*, 111(10):106801, 2013.

[68] P. Joensen, R. Frindt, and S. Morrison. Single-layer MoS_2. *Mater. Res. Bull.*, 21(4):457–461, Apr. 1986.

[69] J. Kang, S. Tongay, J. Zhou, J. Li, and J. Wu. Band offsets and heterostructures of two-dimensional semiconductors. *Appl. Phys. Lett*, 102(1):012111, Jan. 2013.

[70] H. Katzke, P. Tolédano, and W. Depmeier. Phase transitions between polytypes and intralayer superstructures in transition metal dichalcogenides. *Phys. Rev. B*, 69(13):134111, 2004.

[71] S. KC, R. C. Longo, R. Addou, R. M. Wallace, and K. Cho. Impact of intrinsic atomic defects on the electronic structure of MoS_2 monolayers. *Nanotechnology*, 25(37):375703, Aug. 2014.

[72] D. Kim, D. Sun, W. Lu, Z. Cheng, Y. Zhu, D. Le, T. S. Rahman, and L. Bartels. Toward the Growth of an Aligned Single-Layer MoS_2 Film. *Langmuir*, 27(18):11650–11653, 2011.

[73] J. Klimeš, D. R. Bowler, and A. Michaelides. Chemical accuracy for the Van der Waals density functional. *J. Phys. Condens. Matter*, 22(2):022201, Dec.. 2009.

[74] A. V. Kolobov, P. Fons, and J. Tominaga. Electronic excitation-induced semiconductor-to-metal transition in monolayer $MoTe_2$. *Phys. Rev. B*, 94(9), Sep. 2016.

[75] H.-P. Komsa, J. Kotakoski, S. Kurasch, O. Lehtinen, U. Kaiser, and A. V. Krasheninnikov. Two-Dimensional Transition Metal Dichalcogenides under Electron Irradiation: Defect Production and Doping. *Phys. Rev. Lett*, 109(3), Jul. 2012.

[76] H.-P. Komsa and A. V. Krasheninnikov. Native defects in bulk and monolayer MoS_2 from first principles. *Phys. Rev. B*, 91(12), Mar. 2015.

[77] H.-P. Komsa, S. Kurasch, O. Lehtinen, U. Kaiser, and A. V. Krasheninnikov. From point to extended defects in two-dimensional MoS_2: Evolution of atomic structure under electron irradiation. *Phys. Rev. B*, 88(3), Jul. 2013.

[78] D. Kong, H. Wang, J. J. Cha, M. Pasta, K. J. Koski, J. Yao, and Y. Cui. Synthesis of MoS_2 and $MoSe_2$ Films with Vertically Aligned Layers. *Nano Lett.*, 13(3):1341–1347, Feb. 2013.

[79] A. Kormányos, V. Zólyomi, N. D. Drummond, P. Rakyta, G. Burkard, and V. I. Fal'ko. Monolayer MoS_2: trigonal warping, the Γ valley, and spin-orbit coupling effects. *Phys. Rev. b*, 88(4):045416, 2013.

[80] N. Krane, C. Lotze, and K. J. Franke. Moiré Structure of MoS_2 on Au(111): Local Structural and Electronic Properties. *Surf. Sci.*, 2018.

[81] N. Krane, C. Lotze, J. M. Lager, G. Reecht, and K. J. Franke. Electronic Structure and Luminescence of Quasi-Freestanding MoS_2 Nanopatches on Au(111). *Nano Lett.*, 16(8):5163–5168, 2016.

[82] G. Kresse and J. Hafner. Ab-initio molecular dynamics for liquid metals. *Phys. Rev. B*, 47:558, 1993.

[83] A. V. Krukau, O. A. Vydrov, A. F. Izmaylov, and G. E. Scuseria. Influence of the exchange screening parameter on the performance of screened hybrid functionals. *J. Chem. Phys*, 125(22):224106, Dec. 2006.

[84] A. Kumar and P. Ahluwalia. Electronic structure of transition metal dichalcogenides monolayers 1H-MX_2 (M= Mo, W; X= S, Se, Te) from *ab-initio* theory: new direct band gap semiconductors. *Eur. Phys. J. B*, 85(6):186, 2012.

[85] R. Larciprete, S. Ulstrup, P. Lacovig, M. Dalmiglio, M. Bianchi, F. Mazzola, L. Hornekær, F. Orlando, A. Baraldi, P. Hofmann, and S. Lizzit. Oxygen Switching of the Epitaxial Graphene–Metal Interaction. *ACS Nano*, 6(11):9551–9558, Oct.. 2012.

[86] J. L. LaRue, J. White, N. Nahler, Z. Liu, Y. Sun, P. Pianetta, D. J. Auerbach, and A. M. Wodtke. The work function of submonolayer cesium-covered gold: A photoelectron spectroscopy study. *J. Chem. Phys.*, 129(2):024709, 2008.

[87] S. LaShell, B. McDougall, and E. Jensen. Spin splitting of an Au(111) surface state band observed with angle resolved photoelectron spectroscopy. *Phys. Rev. Lett*, 77(16):3419, 1996.

[88] S. Lebegue and O. Eriksson. Electronic structure of two-dimensional crystals from *ab initio* theory. *Phys. Rev. B*, 79(11):115409, 2009.

[89] Y.-H. Lee, X.-Q. Zhang, W. Zhang, M.-T. Chang, C.-T. Lin, K.-D. Chang, Y.-C. Yu, J. T.-W. Wang, C.-S. Chang, L.-J. Li, and T.-W. Lin. Synthesis of Large-Area MoS_2 Atomic Layers with Chemical Vapor Deposition. *Adv. Mater.*, 24(17):2320–2325, 2012.

[90] H. Li, J. Wu, Z. Yin, and H. Zhang. Preparation and Applications of Mechanically Exfoliated Single-Layer and Multilayer MoS_2 and WSe_2 Nanosheets. *Accounts of Chemical Research*, 47(4):1067–1075, Apr. 2014.

[91] T. Li and G. Galli. Electronic properties of single-layer and multilayer transition metal dichalcogenides MX2 (M = Mo,Wand X = S, Se). *J. Phys. Chem. C*, 111(44):16192–16196, 2007.

[92] Y.-C. Lin, W. Zhang, J.-K. Huang, K.-K. Liu, Y.-H. Lee, C.-T. Liang, C.-W. Chu, and L.-J. Li. Wafer-scale MoS_2 thin layers prepared by MoO_3 sulfurization. *Nanoscale*, 4(20):6637, 2012.

[93] X. Ling, Y.-H. Lee, Y. Lin, W. Fang, L. Yu, M. S. Dresselhaus, and J. Kong. Role of the Seeding Promoter in MoS_2 Growth by Chemical Vapor Deposition. *Nano Lett.*, 14(2):464–472, Jan. 2014.

[94] D. Liu, Y. Guo, L. Fang, and J. Robertson. Sulfur vacancies in monolayer MoS_2 and its electrical contacts. *Appl. Phys. Lett*, 103(18):183113, Oct. 2013.

[95] G.-B. Liu, W.-Y. Shan, Y. Yao, W. Yao, and D. Xiao. Three-band tight-binding model for monolayers of group-VIB transition metal dichalcogenides. *Phys. Rev. B*, 88(8), Aug. 2013.

[96] G.-B. Liu, D. Xiao, Y. Yao, X. Xu, and W. Yao. Electronic structures and theoretical modelling of two-dimensional group-vib transition metal dichalcogenides. *Chem. Soc. Rev*, 44(9):2643–2663, 2015.

[97] H.-L. Liu, C.-C. Shen, S.-H. Su, C.-L. Hsu, M.-Y. Li, and L.-J. Li. Optical properties of monolayer transition metal dichalcogenides probed by spectroscopic ellipsometry. *Appl. Phys. Lett*, 105(20):201905, Nov. 2014.

[98] K.-K. Liu, W. Zhang, Y.-H. Lee, Y.-C. Lin, M.-T. Chang, C.-Y. Su, C.-S. Chang, H. Li, Y. Shi, H. Zhang, C.-S. Lai, and L.-J. Li. Growth of Large-Area and Highly Crystalline MoS_2 Thin Layers on Insulating substrates. *Nano Lett.*, 12(3):1538–1544, 2012.

[99] S. Lizzit, R. Larciprete, P. Lacovig, M. Dalmiglio, F. Orlando, A. Baraldi, L. Gammelgaard, L. Barreto, M. Bianchi, E. Perkins, and P. Hofmann. Transfer-Free Electrical Insulation of Epitaxial Graphene from its Metal Substrate. *Nano Lett.*, 12(9):4503–4507, Aug. 2012.

[100] H. Lüth. *Surfaces and interfaces of solid materials*. Springer Science & Business Media, 2013.

[101] C.-P. Lu, G. Li, J. Mao, L.-M. Wang, and E. Y. Andrei. Bandgap, mid-gap states, and gating effects in MoS_2. *Nano Lett.*, 14(8):4628–4633, 2014.

[102] X. Lu, M. I. B. Utama, J. Zhang, Y. Zhao, and Q. Xiong. Layer-by-layer thinning of MoS_2 by thermal annealing. *Nanoscale*, 5(19):8904–8908, Jul. 2013.

[103] H. Luth and J. Bohm. Surfaces and interfaces of solid materials. *Crystal Research and Technology*, 31(2):150–150, 1996.

[104] J. E. Mahan, K. M. Geib, G. Y. Robinson, and R. G. Long. A review of the geometrical fundamentals of reflection high-energy electron diffraction with application to silicon surfaces. *J. Vac. Sci. Technol*, 8(5):3692–3700, Sep. 1990.

[105] S. K. Mahatha, A. S. Ngankeu, N. F. Hinsche, I. Mertig, K. Guilloy, P. L. Matzen, M. Bianchi, C. E. Sanders, J. A. Miwa, H. Bana, et al. Electron-phonon coupling in single-layer mos_2. *Surface Science*, 681:64–69, 2019.

[106] K. F. Mak, C. Lee, J. Hone, J. Shan, and T. F. Heinz. Atomically thin MoS_2: a new direct-gap semiconductor. *Phys. Rev. Lett*, 105(13):136805, 2010.

[107] J. C. Meyer, A. K. Geim, M. I. Katsnelson, K. S. Novoselov, T. J. Booth, and S. Roth. The structure of suspended graphene sheets. *Nature*, 446(7131):60–63, Mar. 2007.

[108] J. A. Miwa, S. Ulstrup, S. G. Sørensen, M. Dendzik, A. G. Čabo, M. Bianchi, J. V. Lauritsen, and P. Hofmann. Electronic Structure of Epitaxial Single-Layer MoS_2. *Phys. Rev. Lett.*, 114(4):046802, 2015.

[109] H. Murata, K. Kataoka, and A. Koma. Scanning tunneling microscope images of locally modulated structures in layered materials, $MoS_2(0001)$ and $MoSe_2(0001)$, induced by impurity atoms. *Surface Science*, 478(3):131–144, May. 2001.

[110] A. V. Murugan, M. Quintin, M.-H. Delville, G. Campet, C. S. Gopinath, and K. Vijayamohanan. Exfoliation-Induced Nanoribbon Formation of Poly(3,4-Ethylene Dioxythiophene) PEDOT Between MoS_2 Layers as Cathode Material for Lithium Batteries. *J. Power Sources*, 156(2):615–619, 2006.

[111] S. Najmaei, Z. Liu, W. Zhou, X. Zou, G. Shi, S. Lei, B. I. Yakobson, J.-C. Idrobo, P. M. Ajayan, and J. Lou. Vapour phase growth and grain boundary structure of molybdenum disulphide atomic layers. *Nature Materials*, 12(8):754–759, Jun. 2013.

[112] V. Nicolosi, M. Chhowalla, M. G. Kanatzidis, M. S. Strano, and J. N. Coleman. Liquid exfoliation of layered materials. *Science*, 340(6139):1226419–1226419, Jun. 2013.

[113] F. Nix and D. MacNair. The Thermal Expansion of Pure Metals: Copper, Gold, Aluminum, Nickel, and Iron. *Phys. Rev.*, 60(8):597, 1941.

[114] J.-Y. Noh, H. Kim, and Y.-S. Kim. Stability and electronic structures of native defects in single-layerMoS2. *Phys. Rev. B*, 89(20), May. 2014.

[115] K. Novoselov, D. Jiang, F. Schedin, T. Booth, V. Khotkevich, S. Morozov, and A. Geim. Two-dimensional atomic crystals. *Proc. Natl. Acad. Sci. U.S.A.*, 102(30):10451–10453, 2005.

[116] H. Ochoa and R. Roldán. Spin-orbit-mediated spin relaxation in monolayer MoS_2. *Phys. Rev. B*, 87(24):245421, 2013.

[117] D. J. O'Connor, B. A. Sexton, and R. S. Smart. *Surface analysis methods in materials science*, volume 23. Springer Science & Business Media, 2013.

[118] C. M. Orofeo, S. Suzuki, Y. Sekine, and H. Hibino. Scalable Synthesis of Layer-Controlled WS_2 and MoS_2 Sheets by Sulfurization of Thin Metal Films. *Appl. Phys. Lett.*, 105(8):083112, 2014.

[119] B. Ouyang, G. Lan, Y. Guo, Z. Mi, and J. Song. Phase engineering of monolayer transition-metal dichalcogenide through coupled electron doping and lattice deformation. *Appl. Phys. Lett*, 107(19):191903, 2015.

[120] J. E. Padilha, H. Peelaers, A. Janotti, and C. G. V. de Walle. Nature and evolution of the band-edge states in MoS_2: From monolayer to bulk. *Phys. Rev. B*, 90(20), Nov. 2014.

[121] J. P. Perdew, K. Burke, and M. Ernzerhof. Generalized Gradient Approximation Made Simple. *Phys. Rev. Lett*, 77(18):3865–3868, Oct. 1996.

[122] M. Py and R. Haering. Structural Destabilization Induced by Lithium Intercalation in MoS_2 and Related Compounds. *Canadian J. Phys.*, 61(1):76–84, 1983.

[123] Y. Qi, P. G. Naumov, M. N. Ali, C. R. Rajamathi, W. Schnelle, O. Barkalov, M. Hanfland, S.-C. Wu, C. Shekhar, Y. Sun, V. Süß, M. Schmidt, U. Schwarz, E. Pippel, P. Werner, R. Hillebrand, T. Förster, E. Kampert, S. Parkin, R. J. Cava, C. Felser, B. Yan, and S. A. Medvedev. Superconductivity in Weyl semimetal candidate $MoTe_2$. *Nat. Commun*, 7:11038, Mar. 2016.

[124] X. Qin, D. Yang, R. Frindt, and J. Irwin. Real-space imaging of single-layer MoS_2 by scanning tunneling microscopy. *Phys. Rev. B*, 44(7):3490, 1991.

[125] H. Qiu, T. Xu, Z. Wang, W. Ren, H. Nan, Z. Ni, Q. Chen, S. Yuan, F. Miao, F. Song, et al. Hopping transport through defect-induced localized states in molybdenum disulphide. *Nature communications*, 4:2642, 2013.

[126] B. Radisavljevic, A. Radenovic, J. Brivio, i. V. Giacometti, and A. Kis. Single-layer MoS_2 transistors. *Nat. Nanotechnol*, 6(3):147, 2011.

[127] A. Ramasubramaniam. Large excitonic effects in monolayers of molybdenum and tungsten dichalcogenides. *Phys. Rev. B*, 86(11):115409, 2012.

[128] C. Riedl, C. Coletti, T. Iwasaki, A. Zakharov, and U. Starke. Quasi-Free-Standing Epitaxial Graphene on SiC Obtained by Hydrogen Intercalation. *Phys. Rev. Lett.*, 103(24):246804, 2009.

[129] P. Rivera, J. R. Schaibley, A. M. Jones, J. S. Ross, S. Wu, G. Aivazian, P. Klement, K. Seyler, G. Clark, N. J. Ghimire, J. Yan, D. G. Mandrus, W. Yao, and X. Xu. Observation of long-lived interlayer excitons in monolayer $MoSe_2/WSe_2$ heterostructures. *Nature Communications*, 6(1), Feb. 2015.

[130] A. S. Rodin, P. Z. Hanakata, A. Carvalho, H. S. Park, D. K. Campbell, and A. H. C. Neto. Spin-Orbit Dirac Fermions in 2D Systems. *arXiv preprint arXiv:1703.04713*, 2017.

[131] R. Roldán, J. A. Silva-Guillén, M. P. López-Sancho, F. Guinea, E. Cappelluti, and P. Ordejón. Electronic properties of single-layer and multilayer transition metal dichalcogenides MX_2 (M= Mo, W and X= S, Se). *Ann. Phys. (Berl.)*, 526(9-10):347–357, 2014.

[132] H. Rydberg, M. Dion, N. Jacobson, E. Schröder, P. Hyldgaard, S. Simak, D. C. Langreth, and B. I. Lundqvist. Van der Waals density functional for layered structures. *Phys. Rev. Lett*, 91(12):126402, 2003.

[133] K. D. P. S. K. Mahatha and K. S. R. Menon. Electronic structure investigation of MoS_2 and $MoSe_2$ using angle-resolved photoemission spectroscopy and *ab-initio* band structure studies. *J. Phys. Condens. Matter*, 24(47):475504, Oct.. 2012.

[134] S. J. Sandoval, D. Yang, R. Frindt, and J. Irwin. Raman study and lattice dynamics of single molecular layers of MoS_2. *Phys. Rev. B*, 44(8):3955, 1991.

[135] T. Sekine, M. Izumi, T. Nakashizu, K. Uchinokura, and E. Matsuura. Raman Scattering and Infrared Reflectance in 2H-$MoSe_2$. *J. Phys. Soc. Jpn*, 49(3):1069–1077, Sep. 1980.

[136] C.-J. Shih, A. Vijayaraghavan, R. Krishnan, R. Sharma, J.-H. Han, M.-H. Ham, Z. Jin, S. Lin, G. L. Paulus, N. F. Reuel, Q. H. Wang, D. Blankschtein, and M. S. Strano. Bi- and trilayer graphene solutions. *Nature Nanotechnology*, 6(7):439–445, Jun. 2011.

[137] R. Somoano, V. Hadek, and A. Rembaum. Alkali metal intercalates of molybdenum disulfide. *The Journal of Chemical Physics*, 58(2):697–701, 1973.

[138] I. Song, C. Park, M. Hong, J. Baik, H.-J. Shin, and H. C. Choi. Patternable large-scale molybdenium disulfide atomic layers grown by gold-assisted chemical vapor deposition. *Angewandte Chemie*, 126(5):1290–1293, 2014.

[139] S. G. Sørensen, H. G. Füchtbauer, A. K. Tuxen, A. S. Walton, and J. V. Lauritsen. Structure and Electronic Properties of In Situ Synthesized Single-Layer MoS_2 on a Gold Surface. *ACS Nano*, 8(7):6788–6796, Jun. 2014.

[140] A. Splendiani, L. Sun, Y. Zhang, T. Li, J. Kim, C.-Y. Chim, G. Galli, and F. Wang. Emerging photoluminescence in monolayer MoS_2. *Nano Lett.*, 10(4):1271–1275, 2010.

[141] L. Sun, J. Yan, D. Zhan, L. Liu, H. Hu, H. Li, B. K. Tay, J.-L. Kuo, C.-C. Huang, D. W. Hewak, et al. Spin-orbit splitting in single-layer MoS_2 revealed by triply resonant Raman scattering. *Phys. Rev. Lett*, 111(12):126801, 2013.

[142] S. J. R. Tan, S. Sarkar, X. Zhao, X. Luo, Y. Z. Luo, S. M. Poh, I. Abdelwahab, W. Zhou, T. Venkatesan, W. Chen, et al. Temperature and Phase Dependent Phonon Renormalization in 1T' MoS_2. *ACS Nano*, 12(5):5051–5058, 2018.

[143] D.-M. Tang, D. G. Kvashnin, S. Najmaei, Y. Bando, K. Kimoto, P. Koskinen, P. M. Ajayan, B. I. Yakobson, P. B. Sorokin, J. Lou, and D. Golberg. Nanomechanical cleavage of molybdenum disulphide atomic layers. *Nature Communications*, 5(1), Apr. 2014.

[144] S. Tongay, J. Suh, C. Ataca, W. Fan, A. Luce, J. S. Kang, J. Liu, C. Ko, R. Raghunathanan, J. Zhou, F. Ogletree, J. Li, J. C. Grossman, and J. Wu. Defects activated photoluminescence in two-dimensional semiconductors: interplay between bound, charged and free excitons. *Scientific Reports*, 3(1), Sep. 2013.

[145] M. M. Ugeda, A. J. Bradley, S.-F. Shi, F. H. da Jornada, Y. Zhang, D. Y. Qiu, W. Ruan, S.-K. Mo, Z. Hussain, Z.-X. Shen, F. Wang, S. G. Louie, and M. F. Crommie. Giant bandgap renormalization and excitonic effects in a monolayer transition metal dichalcogenide semiconductor. *Nature Materials*, 13(12):1091–1095, Aug. 2014.

[146] S. Ulstrup, M. Andersen, M. Bianchi, L. Barreto, B. Hammer, L. Hornekær, and P. Hofmann. Sequential oxygen and alkali intercalation of epitaxial graphene on Ir(111): enhanced many-body effects and formation of pn-interfaces. *2D Materials*, 1(2):025002, Aug. 2014.

[147] P. Vancsó, G. Z. Magda, J. Pető, J.-Y. Noh, Y.-S. Kim, C. Hwang, L. P. Biró, and L. Tapasztó. The intrinsic defect structure of exfoliated MoS_2 single layers revealed by Scanning Tunneling Microscopy. *Scientific Reports*, 6(1), Jul. 2016.

[148] A. Varykhalov, J. Sánchez-Barriga, A. Shikin, C. Biswas, E. Vescovo, A. Rybkin, D. Marchenko, and O. Rader. Electronic and magnetic properties of quasifreestanding graphene on ni. *Phys. Rev. Lett.*, 101(15):157601, 2008.

[149] VASP. https://www.vasp.at/, May 2019.

[150] P. R. Wallace. The band theory of graphite. *Phys. Rev.*, 71(9):622, 1947.

[151] A. L. Walter, K.-J. Jeon, A. Bostwick, F. Speck, M. Ostler, T. Seyller, L. Moreschini, Y. S. Kim, Y. J. Chang, K. Horn, and E. Rotenberg. Highly p-doped epitaxial graphene obtained by fluorine intercalation. *Appl. Phys. Lett*, 98(18):184102, May. 2011.

[152] D. Wang, Z. Wang, C. Wang, P. Zhou, Z. Wu, and Z. Liu. Distorted MoS_2 nanostructures: An efficient catalyst for the electrochemical hydrogen evolution reaction. 34:219–222, 2013.

[153] X. Wang, H. Feng, Y. Wu, and L. Jiao. Controlled Synthesis of Highly Crystalline MoS_2 Flakes by Chemical Vapor Deposition. *Journal of the American Chemical Society*, 135(14):5304–5307, Mar. 2013.

[154] X. Wang, X. Shen, Z. Wang, R. Yu, and L. Chen. Atomic-Scale Clarification of Structural Transition of MoS_2 Upon Sodium Intercalation. *ACS Nano*, 8(11):11394–11400, 2014.

[155] Y. Wang, L. Li, W. Yao, S. Song, J. Sun, J. Pan, X. Ren, C. Li, E. Okunishi, Y.-Q. Wang, E. Wang, Y. Shao, Y. Y. Zhang, H.-T. Yang, E. F. Schwier, H. Iwasawa, K. Shimada, M. Taniguchi, Z. Cheng, Z. Zhou, S. Du, S. J. Pennycook, S. T. Pantelides, and H.-J. Gao. Monolayer $PtSe_2$, a New Semiconducting Transition-Metal-Dichalcogenide, Epitaxially Grown by Direct Selenization of Pt. *Nano Lett.*, 15(6):4013–4018, 2015.

[156] Y. Wang, J. Z. Ou, S. Balendhran, A. F. Chrimes, M. Mortazavi, D. D. Yao, M. R. Field, K. Latham, V. Bansal, J. R. Friend, S. Zhuiykov, M. S. Medhekar, Nikkil Vand Strano, and K. Kalantar-zadeh. Electrochemical Control of Photoluminescence in Two-Dimensional MoS_2 Nanoflakes. *ACS Nano*, 7(11):10083–10093, 2013.

[157] J. Warmuth, A. Bruix, M. Michiardi, T. Hänke, M. Bianchi, J. Wiebe, R. Wiesendanger, B. Hammer, P. Hofmann, and A. A. Khajetoorians. Band-Gap Engineering by Bi Intercalation of Graphene on Ir(111). *Phys. Rev. B*, 93(16):165437, 2016.

[158] M. S. Whittingham. Electrical Energy Storage and Intercalation Chemistry. *Science*, 192(4244):1126–1127, 1976.

[159] F. Wypych and R. Schöllhorn. 1T-MoS_2, a New Metallic Modification of Molybdenum Disulfide. *J. Chem. Soc. Chem. Comm.*, (19):1386–1388, 1992.

[160] D. Xiao, G.-B. Liu, W. Feng, X. Xu, and W. Yao. Coupled spin and valley physics in monolayers of MoS_2 and other group-VI dichalcogenides. *Phys. Rev. Lett*, 108(19):196802, 2012.

[161] F. Xiong, H. Wang, X. Liu, J. Sun, M. Brongersma, E. Pop, and Y. Cui. Li Intercalation in MoS_2: In Situ Observation of its Dynamics and Tuning Optical and Electrical Properties. *Nano Lett.*, 15(10):6777–6784, 2015.

[162] X. Xu, W. Yao, D. Xiao, and T. F. Heinz. Spin and pseudospins in layered transition metal dichalcogenides. *Nature Physics*, 10(5):343, 2014.

[163] Y. Yu, G. Li, L. Huang, A. Barrette, Y.-Q. Cai, Y. Yu, K. Gundogdu, Y.-W. Zhang, and L. Cao. Enhancing Multifunctionalities of Transition-Metal Dichalcogenide Monolayers via Cation Intercalation. *ACS Nano*, 11(9):9390–9396, Sep. 2017.

[164] R. Zan, Q. M. Ramasse, R. Jalil, T. Georgiou, U. Bangert, and K. S. Novoselov. Control of Radiation Damage in MoS_2 by Graphene Encapsulation. *ACS Nano*, 7(11):10167–10174, Oct.. 2013.

[165] H. Zeng, G.-B. Liu, J. Dai, Y. Yan, B. Zhu, R. He, L. Xie, S. Xu, X. Chen, W. Yao, et al. Optical signature of symmetry variations and spin-valley coupling in atomically thin tungsten dichalcogenides. *Sci. Rep*, 3:1608, 2013.

[166] Y. Zhan, Z. Liu, S. Najmaei, P. M. Ajayan, and J. Lou. Large-Area Vapor-Phase Growth and Characterization of MoS_2 Atomic Mayers on a SiO_2 Substrate. *Small*, 8(7):966–971, 2012.

[167] C. Zhang, A. Johnson, C.-L. Hsu, L.-J. Li, and C.-K. Shih. Direct imaging of band profile in single layer MoS2 on graphite: quasiparticle energy gap, metallic edge states, and edge band bending. *Nano Lett.*, 14(5):2443–2447, 2014.

[168] C. Zhang, A. Johnson, C.-L. Hsu, L.-J. Li, and C.-K. Shih. Direct imaging of band profile in single layer MoS_2 on graphite: Quasiparticle energy gap, metallic edge states, and edge band bending. *Nano Lett.*, 14(5):2443–2447, May. 2014.

[169] C. Zhang, H. Wang, W. Chan, C. Manolatou, and F. Rana. Absorption of light by excitons and trions in monolayers of metal dichalcogenide MoS_2: Experiments and theory. *Phys. Rev. B*, 89(20):205436, 2014.

[170] S. Zhang, C.-G. Wang, M.-Y. Li, D. Huang, L.-J. Li, W. Ji, and S. Wu. Defect structure of localized excitons in a WSe_2 monolayer. *Phys. Rev. Lett*, 119(4):046101, 2017.

[171] Y. Zhang, Y.-W. Tan, H. L. Stormer, and P. Kim. Experimental observation of the quantum Hall effect and Berry's phase in graphene. *nature*, 438(7065):201, 2005.

[172] W. Zhao, R. M. Ribeiro, and G. Eda. Electronic structure and optical signatures of semiconducting transition metal dichalcogenide nanosheets. *Accounts of chemical research*, 48(1):91–99, 2014.

[173] W. Zhao, R. M. Ribeiro, M. Toh, A. Carvalho, C. Kloc, A. H. C. Neto, and G. Eda. Origin of Indirect Optical Transitions in Few-Layer MoS_2, WS_2, and WSe_2. *Nano Lett.*, 13(11):5627–5634, Nov. 2013.

[174] L. Zhou, K. Xu, A. Zubair, A. D. Liao, W. Fang, F. Ouyang, Y.-H. Lee, K. Ueno, R. Saito, T. Palacios, J. Kong, and M. S. Dresselhaus. Large-Area Synthesis of High-Quality Uniform Few-Layer $MoTe_2$. *Journal of the American Chemical Society*, 137(37):11892–11895, Sep. 2015.

[175] W. Zhou, X. Zou, S. Najmaei, Z. Liu, Y. Shi, J. Kong, J. Lou, P. M. Ajayan, B. I. Yakobson, and J.-C. Idrobo. Intrinsic Structural Defects in Monolayer Molybdenum Disulfide. *Nano Lett.*, 13(6):2615–2622, May. 2013.

[176] Z. Y. Zhu, Y. C. Cheng, and U. Schwingenschlögl. Giant spin-orbit-induced spin splitting in two-dimensional transition-metal dichalcogenide semiconductors. *Phys. Rev. B*, 84(15), Oct.. 2011.